Radiative Dynamics of Imploded Wires with a Two-Phase Dense Core

G. V. Ivanenkov* and W. Stepniewski**

Lebedev Institute of Physics, Russian Academy of Sciences, Leninskiĭ pr. 53, Moscow, 117924 Russia
e-mail: ivanenkv@sci.lebedev.ru
Kaliski Institute of Plasma Physics and Laser Microfusion, Warsaw 49, Hery 23, Poland
Received October 17, 2001; in final form, January 16, 2002

Abstract—MHD compression of a heterogeneous Z-pinch produced by the explosion of a thin metal wire in the diode of a high-power current generator is investigated. The process is calculated starting from the instant when the breakdown of the evaporation products from the metal surface has come to an end and the current is just switched from the central core to the surrounding plasma corona, whereas the core material is still in the liquid–vapor state. The influence of the cold core on the plasma implosion is studied. The results obtained are compared with similar calculations carried out under the assumption that, in the initial state, either the core material is completely ionized or the core is absent at all. © 2002 MAIK "Nauka/Interperiodica".

1. INTRODUCTION

High energy densities can be achieved by using explosions, shock waves, magnetic implosion, high-power lasers, and pulsed current generators. The latter are used in experiments with fast pinches, which play an important role in controlled fusion research and for X-ray generation. Due to the progress in studying the compression of high-power pinches produced by the explosion of thin metal wires, fast pinch drivers, as well as drivers based on the laser compression of targets, are considered to be promising for inertial confinement fusion. It is believed that, along with lasers, fast pinches will make it possible to obtain in laboratory experiments extreme states of matter, which have so far been attainable only in nuclear explosions. For an electric wire explosion, single wires and wire arrays are used. Of interest are also X-pinches [1] arising in a discharge through two or more thin crossed wires. These pinches, proposed as early as the 1980s, were used in the 1990s to develop the diagnostics of wire discharges [2]. Structurally, X-pinches may also be regarded as a model of a constriction (which is typical of wire explosions), whose hot spots are the sources of X-ray emission from multicharged ions.

This paper is devoted to the study of the MHD compression of a heterogeneous Z-pinch created by the explosion of a thin metal wire under the action of the current produced by a high-power pulsed generator. Most attention is given to the influence of a liquid–vapor core arising in the course of the so-called "cold start" in the two-phase domain of thermodynamic states. For comparison, we present also the data from calculations with initial states lying outside the phase transition domain.

2. PROBLEM OF THE COLD START OF A DISCHARGE THROUGH EXPLODING WIRES

The progress achieved in the late 1990s in research on wire-array liners arose from the idea to substantially increase the number of wires [3]. Following a common notion, it was assumed that the metal evaporates completely in the beginning of the discharge and, then, the plasma shell is imploded toward the axis. The predicted increase in the radiation yield from such a load was confirmed experimentally in the Z device (20 MA, 40 TW) in the Sandia Laboratory (USA), where the soft X-ray yield attained 2 MJ at a peak power higher than 200 TW [4, 5]. However, the real situation turned out to be more complicated, because the metal was evaporated only partially and the bulk of the load material remained at rest. In this case, in spite of a cylindrical shell, extended plasma jets were originated on individual wires [6]. This fact showed the importance of the problem of the cold start (note that the calculations of [7] successfully reproduced the situation in the r–θ geometry).

The essence of the problem is elucidated by the results of experiments [8, 9], in which the modern X-ray backlighting technique with use of X-pinches as pulsed point radiation sources was employed. This technique confirmed the existence of a long-living dense and cold liquid–vapor core surrounded by a plasma corona, i.e., an optically visible plasma column formed during the breakdown of the surface evaporation products. Both media are separated by a sharp (by a factor of up to 100) increase in the density due to the liquid–vapor transition [10]. The study of the discharge start in a low-current device [11] revealed the change in the regime of the impedance growth from a gradual

growth at the beginning of the heating and metal evaporation to the subsequent sharp increase. After the breakdown of the outer vapor, the current first switches to the arising plasma corona and, then, vapor bubbles appear in the metal volume. However, the total evaporation occurred only for very fine wires with a special coating and only for the best conductors (besides Al, Cu, Ag, and Au, all the remaining metals at any accessible sizes could not be exploded completely). It was found that the fast expansion of the central core, as well as the formation and growth of vapor bubbles in the liquid phase are related to the thermal energy introduced due to Joule heating [12].

Hence, the liquid phase and vapor play an important role in the dynamics of exploding wires. The study of their behavior is just beginning, so it is yet unclear how the magnetic field affects metastable states in the region between the binodal (the curve describing the liquid–vapor equilibrium) and the spinodal (the line determining the boundary of the existence domain of an overheated liquid and overcooled vapor in the two-phase region; the spinodal is tangent to the binodal at the critical point). Thus, the thermodynamic analysis [13] of the liquid–vapor equilibrium conditions at the boundary of a current-carrying metal conductor suggests that an electric explosion is the generation of a rapidly expanding mixture of submicron liquid drops with vapor under the action of Joule heating. In this analysis, besides the work on the formation of a surface, the condition of phase equilibrium at the metal boundary also incorporated the work on the bending of magnetic field lines, but did not include the medium motion (later, the quasi-steady medium flow was also incorporated in [14]). The previous models [15] of the evaporation wave and volume boiling assumed the formation of an overheated liquid. Until now, there is still no clear knowledge of the process of electric explosion and switching of the current to the corona. However, it is clear that the long-lived liquid–vapor core exits almost independently of the surrounding corona. Its evolution depends on the load type. In liners, the cores exist throughout the entire discharge phase; the same refers to the main part of the X-pinch (however, there is still little information on the material state in the cross). Finally, in a single-wire load, the independent existence of the core comes to an end after the arrival of an MHD compression wave. The width of the wave front is usually comparable with the core radius; as a result, the hot plasma and the cold dense core interact over a relatively long time. The details of this interaction are still unknown, and it is reasonable to obtain an additional information from numerical simulations.

In this paper, we study the influence of the cold core material on the implosion process. However, we have to omit another important aspect of the cold-start problem, namely, the modeling of the process of the core formation and the switching of the current to the corona in the beginning of the discharge. Accordingly, we have to start calculations from the instant when the switching

of the current to the corona has already finished. Note that Chittenden's model [16], which underlies the calculations of [7], ignores this problem. In that model, it is assumed that, from the very beginning, the metal evaporation products are in the plasma state and the complicated kinetics of phase transitions and the processes of breakdown of the produced vapor are thus ignored.

3. MODIFICATION OF THE RADIATIVE MHD MODEL

Our study required the modification of the previous MHD model [17, 18] of the axisymmetric radiative compression of a hot dense plasma column based on the Eulerian–Lagrangian scheme of Dyachenko free points. The scheme was taken in the version by Jach (a detailed description and various applications of this scheme are given in [19]). The long-term work with the progressively complicated model required its further modification. Like the previous code, the new version describes the transport processes in the magnetic field, radiative–collisional processes, and radiation diffusion (matched in the outer layers to the transparent medium approximation). The innovations reduce to the following: (i) the new code contains the other, wide-range equation of state [20], which works better in the two-phase region; (ii) the other form is used for the power approximations of the Rosseland and Planckian photon ranges proposed in [21]; and (iii) the calculation algorithm is improved, first of all, in the blocks of calculations of multiple ionization and radiation. The main feature of the new code is the description of the metal liquid–vapor transition and the related processes: the formation of neutrals in dense vapor, the presence of the core–corona boundary, and the averaging of the properties of the two-phase medium. This allowed us to avoid the representation of the core material as being the same as the corona plasma, but with a much higher density. Such a plasma was replaced with a cold two-phase medium. Now, the cold start of the discharge is still difficult to model; hence, we have to chose the initial conditions by intuition, based on few experimental data. For the most part, our study is based on the results of experiments with low-current pulses (5 kA, 15 kV, a half-period of 0.6 μs, and a damping time of 8–9 μs) [11] with the use of the X-ray backlighting technique. A longer time duration of the initial implosion phase made it possible to perform photographing, which was impossible in high-current devices.

The most important distinction of the present model from the previous one is the description of the thermodynamically equilibrium liquid–vapor transition. In this description, we do not consider how the magnetic field produced by the current flowing through the metal influences the phase transition, because this problem is still poorly understood. To which extent the equilibrium description is rough can be estimated from the time τ of

the formation of a vapor bubble in liquid.[1] The reciprocal of this time is the probability of atoms to pass through the liquid–vapor interface per unit time. Using the conventional Frenkel representation, we write this quantity in the form $1/\tau = \omega \exp(-\varepsilon/T)$, where ω is the frequency of thermal atomic oscillations in liquid. The characteristic transition energy ε includes the atomic evaporation heat Λ and the work on the formation of a seed vapor nucleus W. As ω, we take the Debye frequency ω_D, which corresponds to wavelengths as short as interatomic spacing. Substituting typical values of the parameters $\omega_D \approx c_s (\rho_l/m_i)^{1/3}$ and $c_s \approx (3Z\varepsilon_F/m_i)^{1/2}$ into $\tau \approx \omega_D^{-1} \exp((\Lambda + W)/T)$ (where ρ_l is the liquid mass density and ε_F is the Fermi electron energy), we obtain that, for copper at $T \geq 0.3$ eV, τ is shorter than the typical duration of the explosion stage of interest (1–10 ns). In this case, we neglect the delay times shorter than 0.1 ns, which are required to overcome the barrier for the formation of vapor bubbles in the liquid in the evaporation region. Hence, if we restrict consideration to these starting temperatures, then, in the first approximation, we can omit the details of the evaporation model, which is important in view of incomplete knowledge of the cold-start processes.

Such a simplification is impossible in the full-scale modeling of the cold-start process, because at real low starting temperatures and typical heating rates of ≈ 0.1 eV/ns ($\approx 10^{12}$ K/s), the nucleus formation time amounts to ≈ 10 ns [22]. For this reason, starting calculations from a real cold initial state may require the description of metastable phases. We will also have to take into account the nonequilibrium heating of solid-state metal. According to measurements [11], the current flowing through a 10-μm-radius wire in the beginning of explosion does not exceed 200–300 A. In other words, the current density attains $j \approx 10^8$ A/cm^2 and the carrier drift velocity at a typical electron density in metal of $n_e \approx 10^{23}$ cm^{-3} is $u = j/en_e \approx 5 \times 10^5$ cm/s, which is comparable to the speed of sound c_s. As a result, in the energy spectrum of the heated electrons, the supersonic component plays an important role. This component excites lattice oscillations via the process of Cherenkov sound emission, which results in ion heating. Note that the electron temperature remains higher than the ion temperature, $T_e > T_i$. The difference between the electron and ion temperatures, which according to [23] is equal to $T_e - T_i = (12/\pi^2)(u/c_s)^2 T_i$ (the quasi-steady estimate in the limit of low Debye temperatures $T_D \ll T_i < T_e$), can attain high values comparable to T_i. As will be shown below, even after 10 ns, the core still remains in the nonequilibrium state with $T_e > T_i$.

The two-phase states were described by using the usual hydrodynamics averaging. This procedure, which

results in the effective homogenization of the heterogeneous core medium, assumes that the radii of bubbles or drops are small in the regions where one of the phases is dominant. In the intermediate region, the interpolation was applied. In this model, the two-phase state was characterized by the vapor volume fraction x, so that the average mixture density was presented in the form $\rho = (1 - x)\rho_l + x\rho_g$, where ρ_l and ρ_g are the mass densities of the liquid and gaseous phases of the core material. For $\rho_g < \rho < \rho_l$, any characteristic of the homogenized medium at pressures of $p < p_c$ and ion temperatures of $T_i < T_c$ (where p_c and T_c are the critical parameters) was defined by the formula $\rho f = (1 - x)\rho_l f_l + x\rho_g f_g$. The one exception was made for the conductivity, for which we used an effective medium model proposed by Kirkpatrick [24]: $\sigma = [Y + (Y^2 + y/2)^{1/2}]\sigma_l$ with the parameters $y = \sigma_g/\sigma_l$ and $Y = [(2 - 3x)(1 - y) + y]/4$. This model works up to the percolation threshold. For nonconducting vapor ($y = 0$) at volume averaging, which more adequately describes the geometrical properties of the phenomenon, it predicts the disappearance of conductivity even for $x = 2/3$ instead of unity.

In view of the fact that the temperature T_i and the pressure p remain constant during evaporation, such a description allows us to perform calculations for the averaged liquid–vapor mixture by solving the same equations of motion and temperature balance between T_e and T_i as were used in [17]. All information about the phase transition was included in the equation of state. For example, the evaporation heat Λ was determined from the difference between the specific enthalpies at $x = 1$ and 0 at a given temperature T_i. Using the binodal equation in the (ρ, T_i) plane in the explicit form [20], we determined the values of ρ_l and ρ_g for a given ion temperature $T_i < T_c$ and, thereby, the volume vapor content $x = (\rho - \rho_g)/(\rho_l - \rho_g)$ for a given mass density. Then, we determine both the individual electron and ion components and the total pressure of the mixture, together with the transport coefficients and radiative properties averaged according to the rules described above. Then, as in [17], we solved the MHD, ionization, and radiation diffusion equations, which gave the distributions of the corresponding quantities over the entire medium volume. It should be noted that, although the equations keep their form in the mixture, the conditions on the core–corona interface are modified: instead of the continuity of the ion heat flux component normal to the boundary, they contain the term $\rho_l V_f \Lambda$, where V_f is the velocity of the boundary with respect to the medium. The core material at the boundary was assumed to be in the liquid state. When the working material was easily evaporated copper and vapor was dominant in the initial state, this implied that the core was surrounded by a thin liquid shell (the possibility of this was demonstrated by the experiments of [11]). Note also that the average charge number Z in the region where it is less than unity, in fact, describes the concentration of elec-

---

[1] It is clear that the volume evaporation time is longer than the surface evaporation time because the latter process goes without the formation of a seed vapor nucleus.

trons and ions in vapor. The description of ionization in this region requires a more complete account for neutral kinetics.

Obviously, this model does not take into account a number specific features of the process, first of all, the above-mentioned possibility of generating metastable states. However, as a first step, this model can be considered admissible. The most significant modification of the code resulted from the introduction of the core–corona interface. Now, the procedure of determining neighbors [19] for the interface points is the same as for those located on the outer plasma surface, so that the model is capable of adequately describing the real contact of two media. Because of the small curvature and low velocity of the interface, the capillary and surface evaporation effects were omitted in the heat and force balances; the validity of this assumption was confirmed by calculations. Previously, when the core was modeled by a dense plasma qualitatively similar to the corona plasma, the contact conditions were not used and the density drop was spread within a cell. A comparison with such calculations showed the importance of the introduction of a special procedure at the core–corona interface. Thus, an insulator–conductor transition of the Mott type appeared in the dense material near the core boundary; i.e., the high-impedance core material transformed into a high-conductivity plasma (see [25]). In turn, this made it necessary to modify the correction for the reduction in the ionization potential due to the influence of the medium. The relative value of this correction depends on the ratio of the Bohr radius to the plasma Debye radius. The fact that their values are comparable meets the criterion for the Mott transition. In our calculations, the value of the total potential taken from [26] (we write its ratio to the potential in vacuum as $1 - q$) decreased below zero. For this reason, the iteration procedure in calculations of the ionization kinetics became unstable. To avoid this, we used different versions and, ultimately, replaced $1 - q$ with the representations in the form $1/(1 + q/k)^k$. For $k = 1$ and 10, calculations demonstrated only a slight dependence on the power index; hence, below, we restrict our analysis to the case $k = 1$.

4. IMPLOSION OF A LOAD WITH A LIQUID–VAPOR CORE

As was mentioned above, our calculations start with a state in which the current is not zero. Previously (see calculations of [8, 17, 18] for W and Ti), this state was associated with the maximum expansion of the products of the electric explosion of the metal wire. Now, the calculations start after the corona has been formed and the core current is switched to the corona. The wire material was chosen taking into account the data accessibility. It was also desirable to have a core that is not too cold in the early stage in order to avoid problems with metastable phases. As was mentioned in Section 2, we chose high-conductivity copper. The 10-μm-radius

copper wire was 4 mm in length. We performed preliminary calculations in which either a core was absent or it was modeled by a jump of the plasma density in the axial region. In subsequent calculations, the problem was formulated in a more correct way by introducing a corona–core interface. The initial density profiles inside the core and the corona were taken to be parabolic, and the temperature was assumed to be constant across the core (0.3 eV < T_c) and the corona (0.8 eV). Near the ends of the load, the corona density was gradually doubled, thereby imitating the evaporation of the electrode material.[2] To initiate perturbations, a random scatter in the parameters at a level of 1% (5% for the core material) was superimposed onto the initial distribution. The outer radius of the plasma produced by explosion was taken to be 300 μm, the core radius was 50 μm, and a 20-fold jump in the density was specified for the core–corona interface (the masses of the core and corona were assumed to be nearly the same). In contrast to [8, 17, 18], where the current varied sinusoidally with time, the current in this run increased linearly from 0.5 to 250 kA over 40 ns and, then, remained constant. The anomalous resistance of the corona was taken into account. The problem was solved on a mesh of 18×240 cells. To check the calculation stability, the number of cells was varied (increased or decreased).

Figure 1a shows the density and temperature distributions at $t = 0$.[3] We can see that, in the core, the electron density is relatively low, which confirms the high content of nonionized vapor. In the early stage of the process, until the core material starts to affect the corona dynamics, the implosion resembles that observed in the previous models without a core [18, 27].[4] A low (on the order of 100 A) current also flows through the core, which results in a somewhat higher (by nearly 0.1 eV) electron temperature near the corona as compared to the ion temperature (0.3–0.5 eV). However, the main current flows through the corona, where the skin layer is formed, as it usually occurs in such problems. This process continues for the first ≈10 ns and is characterized by the higher electron temperature T_e as compared to the ion temperature T_i due to Joule heating. The plasma expands slowly (by 12% in the middle of the pinch and by 19–20% near the ends) up to $t \approx 11$ ns. Then, the implosion begins. After 11.5 ns, the implosion process extends to the wire ends. Between 15 and 18 ns, a shock wave is formed. Its wide front structure is determined by radiation, electron thermal conduction, and multiple ionization. The evidence of the shock formation is the appearance of the density gradient propagating toward the core, as well as the difference between T_i and T_e. The heated region with

---

[2] Otherwise, after 15 ns, both the corona and core near the wire ends were heated intensely, thus giving rise to an enhanced compression in these regions.

[3] In all figures, the anode is on the left and the cathode is on the right.

[4] We note that the computation time for the core region increases substantially.
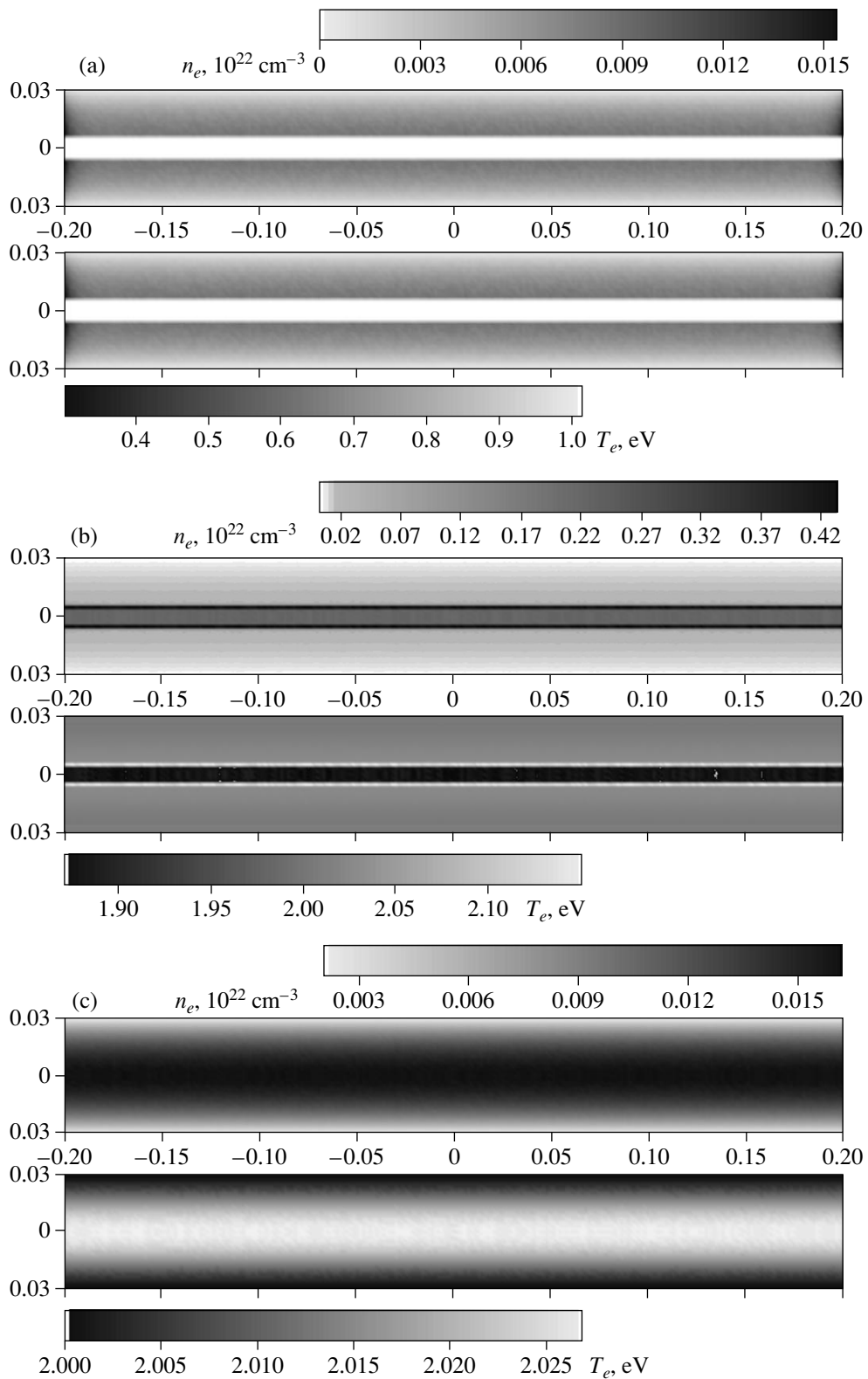
Fig. 1. Initial distributions of the electron densities and temperatures in the models (a) with the evaporation of the core material, (b) with a plasma core, and (c) in the conventional model of the plasma column without a core. The cores surrounded by the corona are seen in the axial regions of frames (a) and (b). In each frame, the density scales are shown at the top and the temperature scales are shown at the bottom. Numerals along and across the images indicate the radial r and axial z coordinates (in cm).

$T_e > T_i$ ahead of the compression front arrives at the core boundary, and, by the time $t = 20$ ns, the core material becomes heated to 1 eV and ionized and the maximum of the electron density is displaced into this region (Fig. 2). By that time, the appearance of the core changes slightly, and the corona boundaries are almost the same on the outer (vacuum) and inner sides. After arriving at the core boundary, the front sharply decelerates. This occurs after 20 ns and is clearly seen in Fig. 2 at $t = 25$ ns. The interaction of the compression wave with the core is confirmed by the increase in the density and the heating of the boundary layer of the dense material. Between 22 and 26 ns, the maximum density n_e increases by a factor of 5 (reaching a value typical of solid metals), whereas the corona temperature $T_e \approx$ 50 eV changes only slightly. At the same time, the shock wave reflected from the interface arrives at the corona–vacuum interface and decelerates the corona compression.[5] This is evidenced by the development of the MHD instability of the corona surface. Because of the corona compression, the released heat density increases, which, in turn, increases the heat flux from the corona into the core. Therefore, the axial inhomogeneity of the subsequent core heating (T_e from ≈ 1 to ≈ 10 eV) correlates with the onset of instability modes in the corona.

Let us consider in more detail how the core material is converted into a plasma. This process begins when the front of the shock wave approaches the core. At $t = 20$ ns, in the distribution of the density n_e, distinct thin layers appear at the core–corona interface. These layers may be attributed to the core heating on the corona side. The important point is a substantial decrease in the ionization potential because of the high density of the compressed material. This decrease (by a factor of 3–4 or higher) becomes even more pronounced at $t > 21$ ns, when the insulator–conductor transition occurs (which is analogous to the metal–dielectric transition considered by Mott). This effect is observed only in the model that uses the procedure of separating the points of the core–corona contact interface. Without this procedure, the material density is not so high and the corrections to the ionization potential do not reach very high values. The core itself is gradually heated by the penetrating UV radiation of the hot plasma corona. As a result, the difference between the electron and ion temperatures increases. By 23 ns, the temperature inside the core reaches 1–10 eV, the average charge number Z becomes close to unity, and the dense core becomes fully ionized. Further, nearly 0.1–0.2 ns before $t = 24$ ns, the process of core heating is rapidly (in an explosive manner) enhanced, in contrast to the previous gradual heating. As is seen in Fig. 3, by 24 ns, the ion temperature T_i is close to 40 eV, whereas T_e reaches 100 eV or higher in the bulk of the core. However, because of the high heating rate, the core material has no time to ionize

strongly. In spite of the high temperature, Z does not exceed unity ($n_i \approx n_e \approx 10^{22}$ cm^{-3}). Such a nonequilibrium state of the core material points to a relatively long electron–ion energy relaxation time τ_{ei}, which, for the given parameter values, is estimated at 10–100 ns. In contrast, the corona plasma is in an almost equilibrium state. The value of Z here is much higher, and, in spite of the lower (as compared to the core) ion density n_i, the electron density n_e here is higher and the temperatures T_e and T_i are close to 50 eV. By 24.5 ns, the excessive heating gradually ceases, the ion charge number in the core becomes consistent with the temperature, which decreases to the coronal level, and the electrons and ions relax to their equilibrium states. Such behavior of the core heating may be explained by the combination of the fast processes related to radiative and electron heat conduction. The corona radiation (UV photons with energies up to 100 eV or higher), penetrating into the core to a depth of several Planckian length l_P ($\sim T_e/n_i$) = 1–10 μm, can heat the core volume at the slow stage of this process. As T_e increases, the front of radiative heating propagates toward the axis. This process is accompanied by the heat removal from the corona to the core by electrons. In this case, the supersonic heat conduction mechanism can be realized, when the heating time r_c^2/χ_e (where r_c is the core radius and χ_e is the electron thermal diffusivity) become shorter than the hydrodynamic time $r_c/c_s \approx 5$ ns, which, in turn is shorter than $\tau_{ei} \sim T_e^{3/2}/Z^2 n_i$. This heating affects only electrons and leads to the ionization of the dense plasma, thus reducing τ_{ei} and the degree to which the material state is nonequilibrium. First, the Rosseland length and, then, l_P become comparable to r_c, the core becomes transparent, and the heating terminates. Because of the high heat conductivity, the skin effect prevents the penetration of the current into the core. By 25 ns, the core temperature falls below the corona level, whereas the degree of ionization is high everywhere.

The current flowing over the core surface produces the magnetic field suppressing the core expansion. The current channel is a thin highly ionized layer clearly seen in Fig. 2 after 20 ns. Since the heated core remains long in the equilibrium state, we can find, using Bennet's condition, that this current can attain 10 kA or higher (the pressure produced by the corona should also be taken into account). The jump in the magnetic field maintains the sharp core boundary. After 25 ns, the alternating compression and expansion regions arise around the narrow central core throughout the entire plasma length. Then, these regions transform rapidly into constrictions and disks. However, the core remains visible for a long time. Its cross size changes only slightly and the boundary remains rather even up to 29 ns. The shape of the corona and the distribution of the core parameters correlate to each other: the density n_e increases appreciably in the constrictions in the core

---

[5] If the core mass is greater than that of the corona, the latter may even expand for a short time.
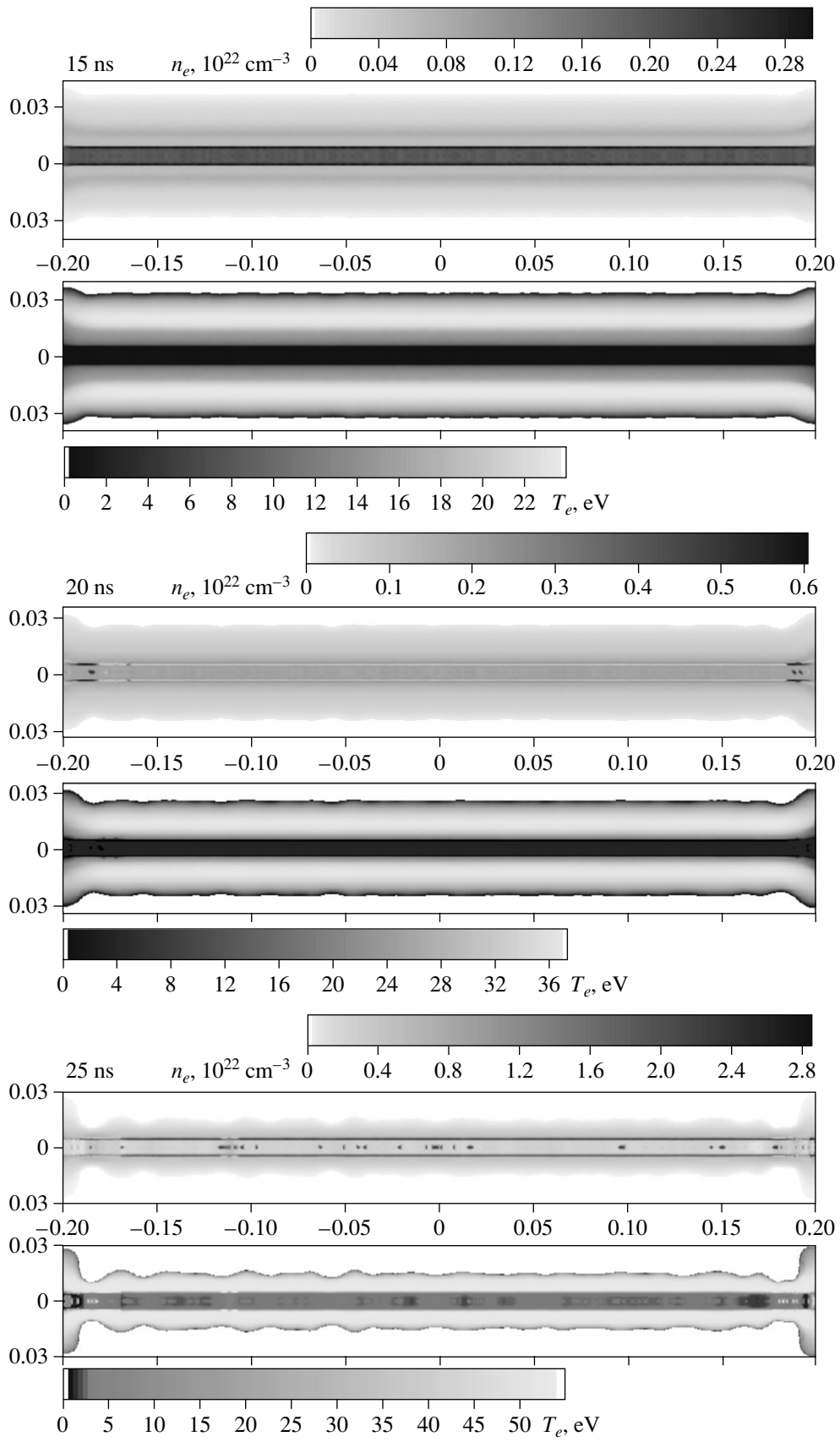
Fig. 2. Time evolution of the spatial distributions of the electron density and temperature in the corona and core in the model with evaporation.
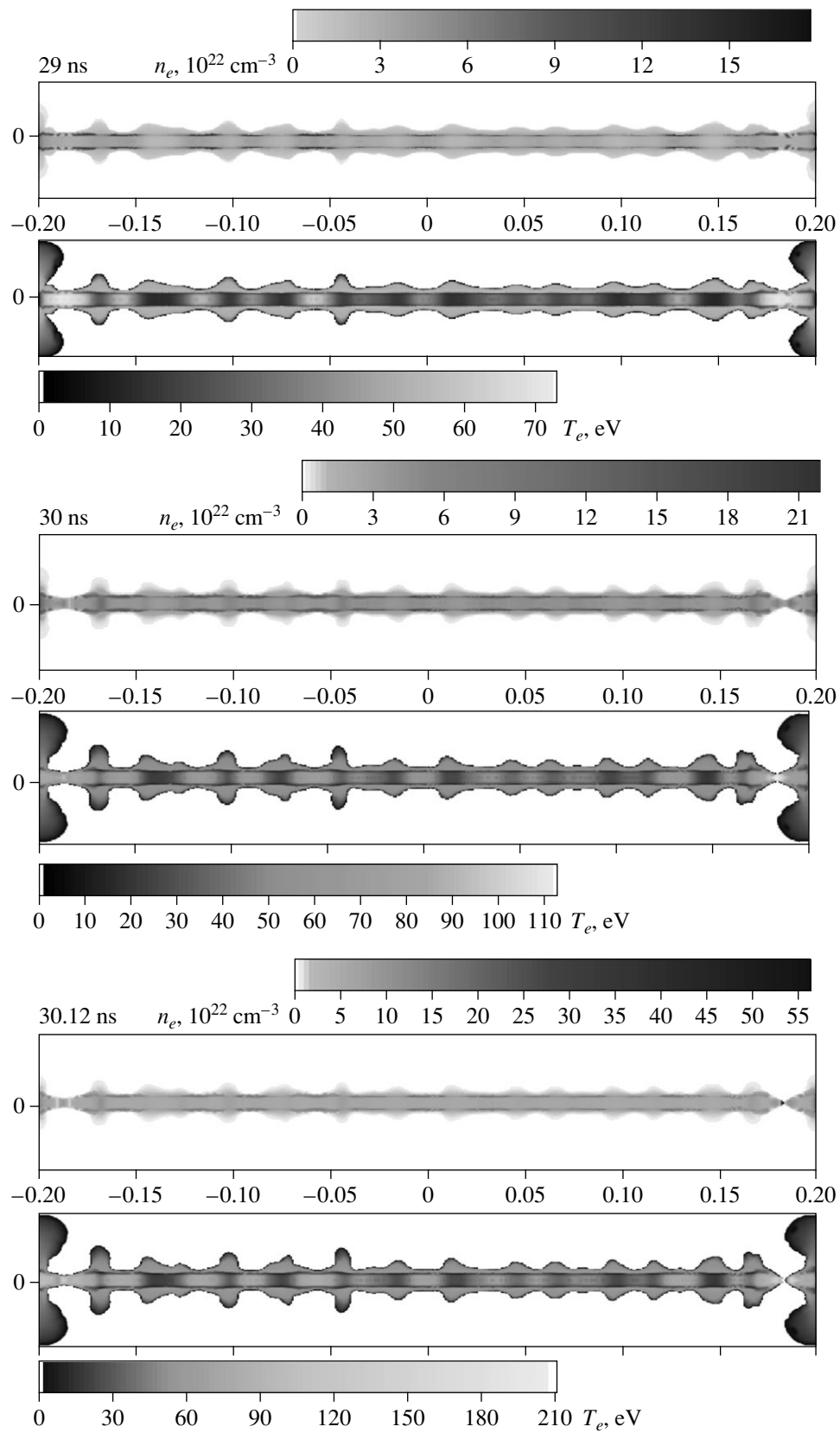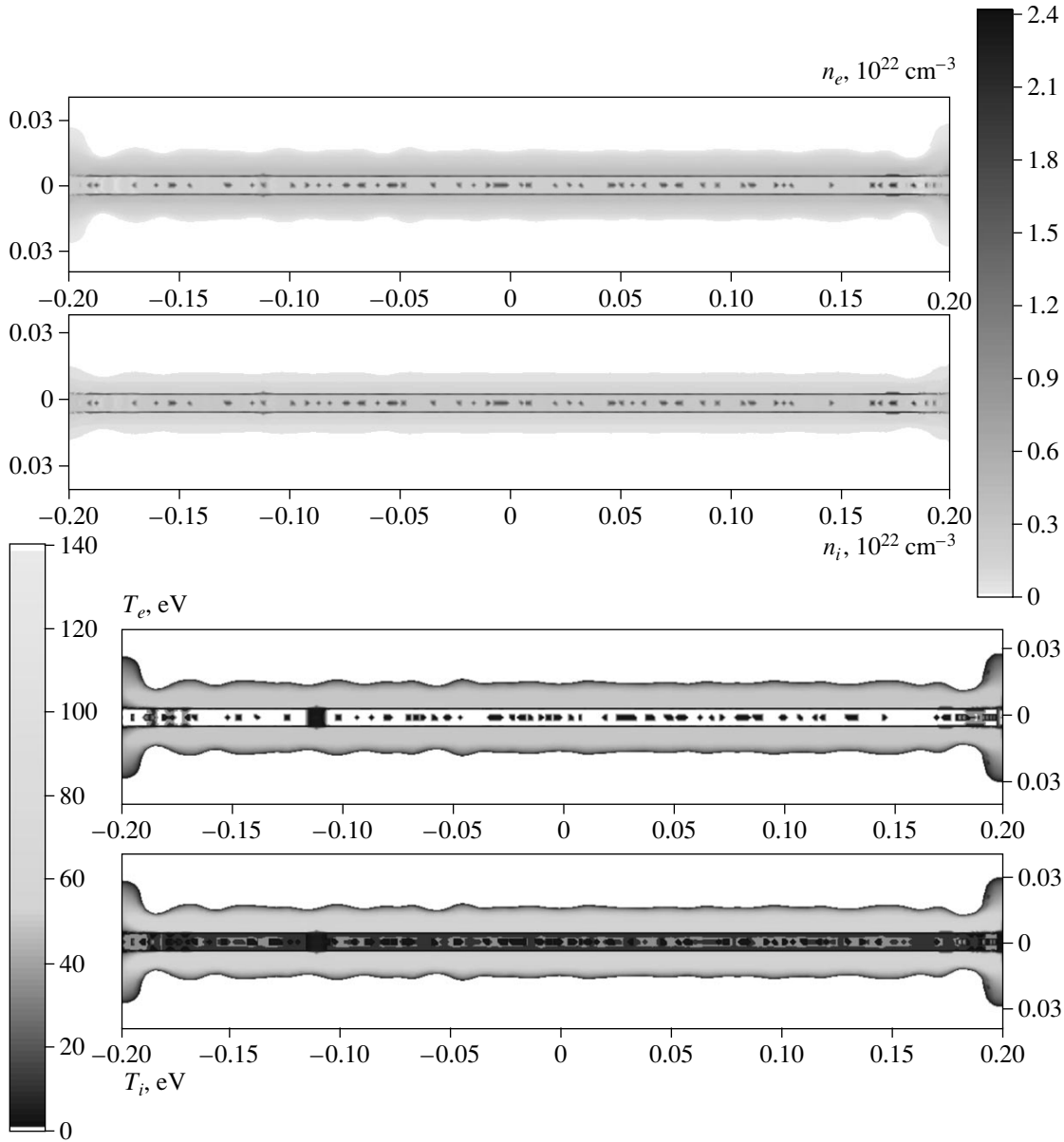
Fig. 2. (Contd.)

Fig. 3. The electron and ion densities and temperatures in the corona and core at the time 24 ns. The same density and temperature scales are used for both plasma components.

boundary layer, whereas the peak of the temperature is displaced inward, where the volume heating is now localized. At $t > 29$ ns, we can see constrictions near the ends and the compression region lying somewhat to the left from the middle. The plasma velocity there attains $(1–2) \times 10^7$ cm/s, and the temperatures increase from 70–80 to 110 eV or higher over 1 ns. The core boundary begins to deform near the ends, which evidences that implosion comes to an end.

The final stage is characterized by a subnanosecond time scale. The fast compression can proceed only locally in the course of the development of constrictions (in Fig. 2, they appear near the ends). This com-

pression is accompanied by the strong local heating of the dense plasma into which the core has been transformed; however, the bulk material cannot change in such a short time interval. Near the right end (Figs. 2, 4a; $t > 30$ ns), the constriction radius decreases during rapid deceleration from ≈ 40 μm to less than 1 μm over ≈ 0.3 ns. In hot spots, the temperatures T_i and T_e attain 0.5–1 keV, the density n_e is $(2–3) \times 10^{23}$ cm^{-3}, the ion charge number Z is 20–22, and the pressure is up to 500 Mbar. In disks, the temperature of the cold core plasma is no higher than 10–30 eV, and the pressure in the most dense part is 3 Mbar, which indicates a very sharp spatial distribution of the parameters.

## 5. COMPARISON WITH SIMPLIFIED MODELS

It is expedient to compare the data obtained with the results of calculations by the same model, but without evaporation, i.e., assuming that, in the initial state, either the core material is completely ionized or the core is absent at all. For this purpose, we increased the initial temperature to 2 eV, which is higher than the critical temperature $T_c \approx 0.85$ eV. The corona density near the ends was increased only in the model with a core. Without a core, the number of current carriers was high enough and there was no need for increasing the corona density. At the boundary of the dense plasma core, we have to spread the initial density jump over a pair of neighboring cells[6] and to artificially require that $Z > 1$ during all the run. In the conventional model of the plasma column, a smooth initial density distribution was represented by a quadratic function vanishing on the surface. The time dependences of the current, the mass and size of the load, and the initial mesh parameters were identical in all cases as far as was allowed by the configuration used. The corresponding distributions at the initial time $t = 0$ are shown in Figs. 1b and 1c (note that the peaks of the densities n_e and n_i fall now into the core).

In the model with a hot plasma core, there is no qualitative differences from the case with a cold core until the shock wave arrives at the corona–core interface. As long as the core does not affect the corona compression dynamics, the picture is very similar to that shown in Fig. 2 for $t = 15$ ns. A closer inspection, however, shows a small quantitative difference in the results obtained with a hot and cold cores. The higher the starting temperature, the larger the initial expansion in the stage of adaptation to physical conditions during the first ≈ 10 ns and the slower the subsequent compression. Thus, with a cold core, the plasma surface radius at 15 ns is larger than the initial one by nearly 3.5–4% (up to 17% near the ends) and the velocity of the plasma motion toward the axis is $\approx 10^6$ cm/s, whereas, in the model with a plasma core, the compression is delayed by nearly 1 ns (in this case, we have 8–9% and $\approx 8 \times 10^5$ cm/s, respectively). The pictures remain similar until the shock wave arrives at the core. The decrease in the ionization potential in a thin layer near the interface between the media is now smaller because there is no insulator–conductor transition [see Figs. 5a, 5b]. On the whole, all the evolution processes seem to be less intense; in particular, the onset of MHD instability in the corona plasma is slower. At the same time, in the constriction regions, the core material is more easily involved into the compression process. As a result, the plasma column is not so rippled and the final picture of the parameter distribution in Fig. 4b is less contrast as compared to Fig. 4a.

---

[6] This was done in order to avoid subfemtosecond steps required by the scheme in the early stage of calculations.

Now, let us consider the conventional model without any core. In this model, the implosion process differs strongly from that considered above. Although the load mass is the same as in the previous cases, the plasma is denser than the corona plasma in the models with a core, the initial expansion of the column turns out to be smaller, and the multiple-ionization process goes more slowly. For this reason, the ion charge number in this model is somewhat lower and the plasma conductivity $\sigma \sim T_e^{3/2}/Z$ is higher than those in the models with a core. As a result, the skin effect is more pronounced, the plasma heating is more intense, the plasma shell is formed at an earlier time, and the compression starts more than 1 ns earlier as compared to the models with a core. However, the subsequent acceleration of the denser plasma goes much more slowly and the shock wave with the same front radius is less intense (Fig. 5c). However, in the later stage, when the implosion in the other models is already suppressed by the core, the compression goes more rapidly. The instability of the outer plasma develops at earlier times and is more pronounced (although at later times, after the arrival of the shock wave reflected from the core boundary, the instability in the models with a core develops more rapidly). At $t < 30$ ns, the even shock front propagates toward the axis with a velocity of no higher than 2×10^6 cm/s, thus heating and ionizing the plasma ahead of it. From 22 to 30 ns, the plasma temperature increases very slowly to ≈ 50 eV, whereas the density n_e grows from 2×10^{21} to 1.7×10^{22} cm^{-3}. As the pressure increases to 2 Mbar, the plasma motion toward the axis slows down to 10^5 cm/s. Between 28 and 30 ns, in the growing instability of the plasma column surface, we can distinguish a leading group of constrictions: two constrictions on the anode side and one constriction near the cathode. The shock wave that develops due to the competition between these constrictions arrives at the axis at $t \approx 33$ ns and, then, reflects from it. In the hot spot located at a distance of 0.7 mm from the middle, the plasma parameters are $T_e \approx 130$ eV, $T_i \approx 160$ eV, $Z \approx 16$, and $n_e \approx 10^{23}$ cm^{-3}; the pressure increases, and the compression slows down. For this reason, the implosion velocity falls rapidly from 6×10^6 cm/s to zero. As a result, a rather smooth hot spot ~15 μm in diameter arises in the constriction. The plasma column transforms into a quasi-periodic system of constrictions and disks more pronounced on the anode side. Then, we had to stop computations because the number of points in the constriction rapidly decreases and the arising fluctuations made the results far from realistic.

A comparison of the results of calculations obtained in simplified models shows that the plasma surface in these models has a similar shape. We also note that, in this case, the mobility of the outer plasma turns out to be so high that, near the anode, the outer fragments of neighboring disks merge together. In the case of the ini-
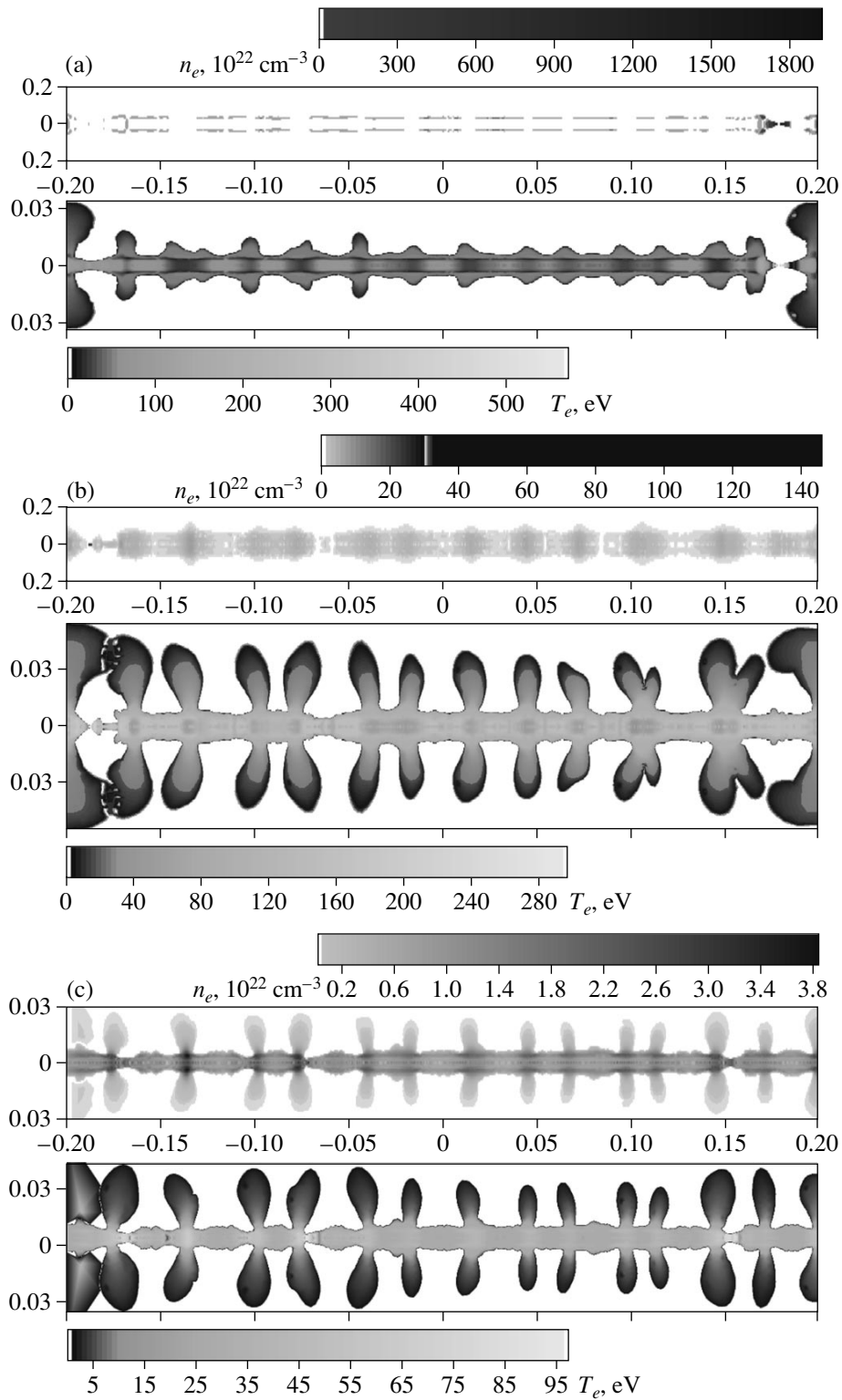
Fig. 4. Final compression states calculated in three models. The correlation between the positions of constrictions and disks obtained with different models is seen.

tial plasma core, the brightest hot spot arises just between these disks; the current through this constriction is probably amplified by the induction loop.

Figures 4 and 5 present the data obtained with three different initial states. As expected, the material mobility generally decreases in the presence of the core. The
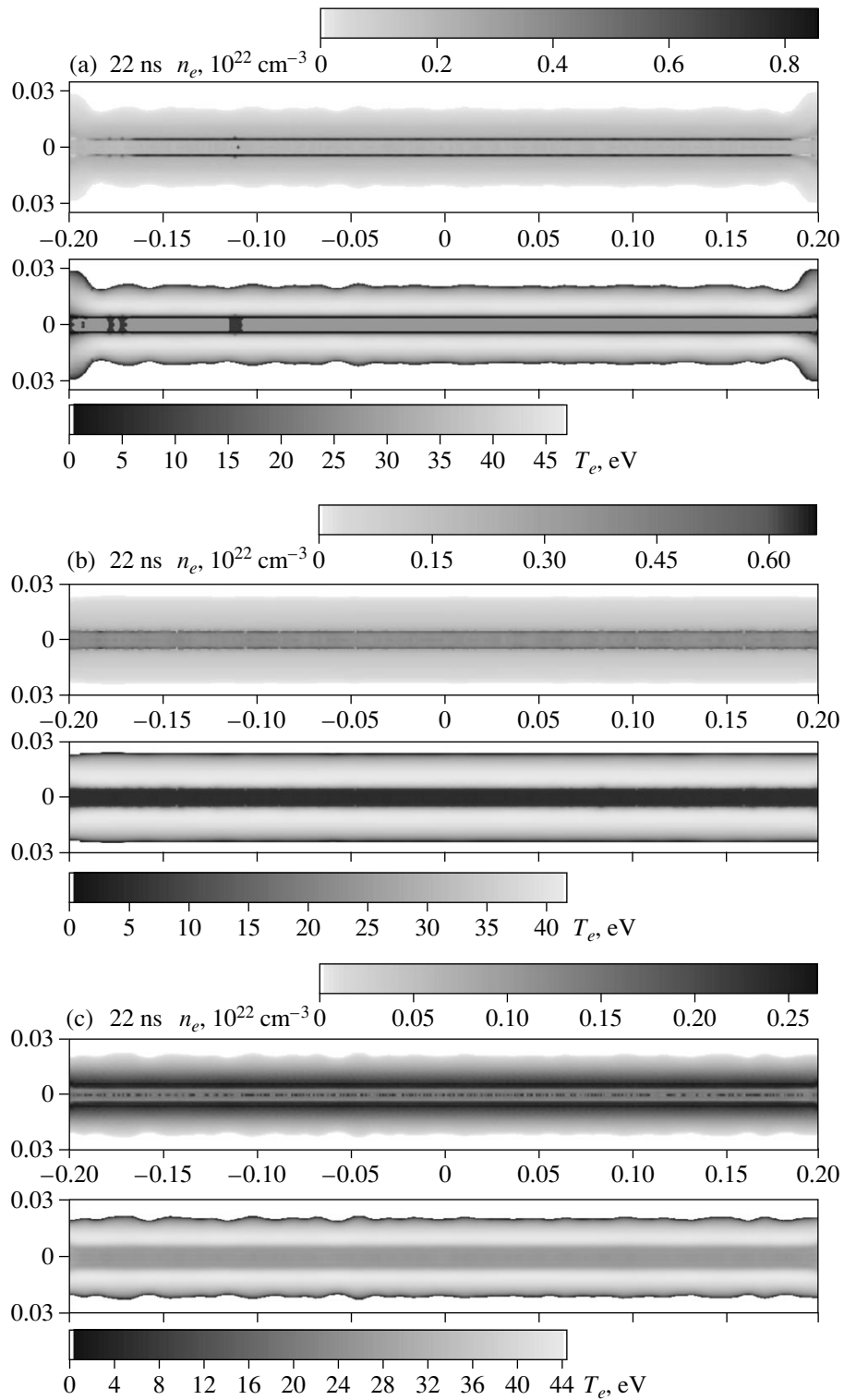
Fig. 5. Comparison of the electron temperature and density distributions calculated for 22 and 26 ns in three models.

increase in the initial core temperature enhances the plasma flows into the disk-shaped regions of the column. However, the plasma there is colder and hot spots are more intense than those predicted by the conventional model. In the absence of a core, the final shape of the column surface is deformed more strongly, the distribution of the material parameters is smoother, and the intensity of hot spots is lower as compared to the mod-
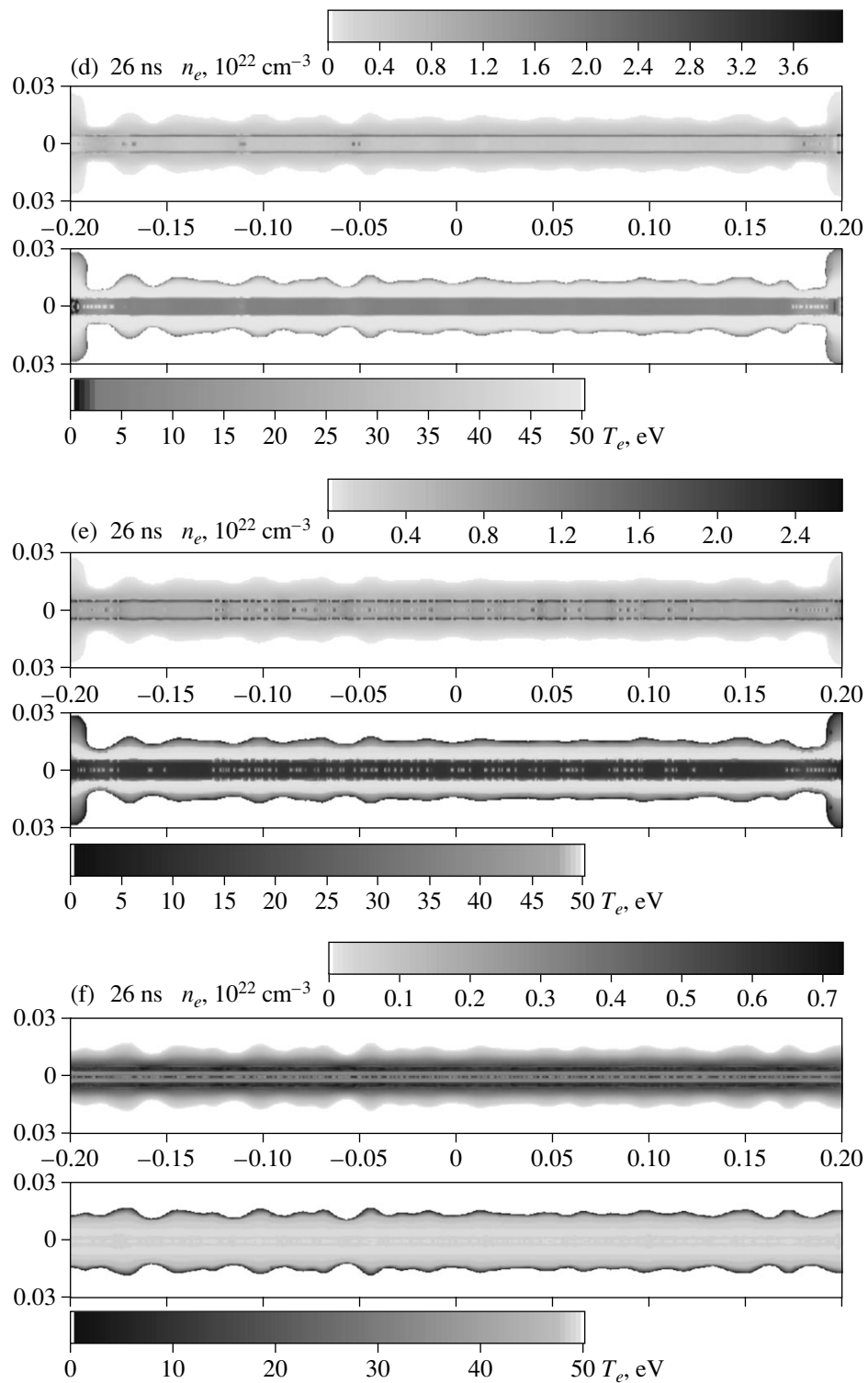
Fig. 5. (Contd.)

els with a core. The cold core suppresses the onset of instability of the corona surface. As a result, the instability develops at later times, when the corona becomes thin and its spatial dimensions decrease. As a result, although the compression time in all the cases is approximately the same (accurate to 10%), the final picture turns out to be very different: the denser and colder the core, the more contrast the distribution of the parameters and the higher their maximum values. Note that the obtained scatter in the final times characterizes

just the difference of the initial states used, including their random component, whereas irregularities in the calculation mesh that cause the termination of computations only locally influence the extremely fast compression phase lasting 10 ps and do not affect the general picture shown in Fig. 4. Therefore, the role of the core is twofold: on the one hand, the compression time increases in the presence of a dense core, and, on the other hand, the presence of a cold core shortens this time, thereby giving rise to the processes of the fast heating and ionization of the core due to heat transfer via corona radiation and supersonic heat conduction.

We should also mention that the computation time increases sharply as the model becomes more complicated. As compared to computations by the conventional model (without a core), this time is longer by a factor of 3 for the model with a plasma core and by a factor of 12–15 for the model with a cold core. For modern CPUs with frequencies of 1 GHz, the run time amounts to several days.

6. CONCLUSION

Over the last few years, an MHD model of the compression of a plasma produced by the explosion of thin metal wires has been developed [17, 18]. This model was applied to materials characterized by a high specific impedance (heavy tungsten, which is opaque to optical and X radiation [8, 17, 18], and relatively light transparent titanium [17, 27]), as well as to high-conductivity copper. Loads in the form of single wires, X-pinches [17, 28], and wire arrays [17] were considered. However, in all of these configurations, the state of a dense and cold material near the axis was described in simplified models. In this paper, we have described the two-phase state of the material in the axial region by incorporating evaporation into the model. As a result, we could depart from the conventional model, as well as from the model with a plasma core. The latter is found to be capable of adequately describing the parameters of hot spots; however, it somewhat underestimates the temperature and the ion charge number and smoothes out both the distributions of the physical quantities and the plasma column boundary. The new model allowed us to perform calculations in the entire core and corona density range observed in experiments. This made it possible to describe the effect of the core on the compression dynamics throughout the entire lifetime of the core. However, in this case, the short initial stage of explosion in which the core and the surrounding plasma corona were formed was excluded from consideration. The available one-dimensional models of the initial stage (see, e.g., [14]) are restricted to the prebreakdown phase. The incorporation of this stage in our two-dimensional model encounters serious difficulties, because this requires a detailed knowledge of the evaporation processes in the current-carrying metal and the breakdown of the evaporation products. In this context, important effects are the formation of metastable phases during the liquid–vapor transition and the influence of metal drops and ion complexes on the breakdown of vapor around the core.

The importance of the cold-start model stems from the fact that, although the presence of a two-phase core has been established experimentally, it is hard to say now what type of a heterogeneous mixture the core substance is: vapor bubbles in a boiling liquid or liquid drops in a dense vapor. This fact testifies to the complexity of the problems arising in contemporary research on exploding wires and to the necessity of the joint effort of theorists, programmers, and experimentors in order to solve them. However, even in the present (far from complete) form, the model demonstrates the effects caused by the presence of a cold and dense core: the Mott transition in a thin boundary layer, the processes of fast heating and ionization of the core material, the slow development of the corona surface instability, and the contrast structure of the parameter distributions. All this explains why the imploding wires are leading loads with respect to the attainable plasma parameters in high-power discharges.

REFERENCES

1. S. M. Zakharov, G. V. Ivanenkov, A. A. Kolomenskiǐ, *et al.*, Pis'ma Zh. Tekh. Fiz. **8**, 1060 (1982) [Sov. Tech. Phys. Lett. **8**, 456 (1982)].

2. D. H. Kalantar and D. A. Hammer, Phys. Rev. Lett. **71**, 3806 (1993); S. A. Pikuz, T. A. Shelkovenko, V. M. Romanova, *et al.*, Rev. Sci. Instrum. **68**, 740 (1997).

3. T. W. L. Sanford, G. O. Allshouse, B. M. Marder, *et al.*, Phys. Rev. Lett. **77**, 5063 (1996).

4. R. B. Spilman, C. Deeney, G. A. Chandler, *et al.*, Phys. Plasmas **5**, 2105 (1998).

5. T. W. L. Sanford, R. C. Mock, R. B. Spilman, *et al.*, Phys. Plasmas **6**, 2030 (1999).

6. S. V. Lebedev, I. H. Mitchell, R. Aliaga-Rossel, *et al.*, Phys. Rev. Lett. **81**, 4152 (1998).

7. J. P. Chittenden, S. V. Lebedev, A. R. Bell, *et al.*, Phys. Rev. Lett. **83**, 100 (1999).

8. G. V. Ivanenkov, A. R. Mingaleev, S. A. Pikuz, *et al.*, in *Proceedings of the 4th International Conference on Dense Z-Pinches, Vancouver, 1997*, Ed. by N. R. Pereira, J. Davis, and P. E. Pulsifer (American Inst. of Physics, Woodbury, 1997); AIP Conf. Proc. **409**, 253 (1997).

9. G. V. Ivanenkov, A. R. Mingaleev, S. A. Pikuz, *et al.*, Zh. Éksp. Teor. Fiz. **114**, 1216 (1998) [JETP **87**, 663 (1998)].

10. S. A. Pikuz, G. V. Ivanenkov, T. A. Shelkovenko, and D. Hammer, Pis'ma Zh. Éksp. Teor. Fiz. **69**, 349 (1999) [JETP Lett. **69**, 377 (1999)].

11. S. A. Pikuz, D. B. Sinars, J. B. Greenly, *et al.*, Phys. Rev. Lett. **83**, 4313 (1999).

12. G. V. Ivanenkov, A. R. Mingaleev, S. A. Pikuz, *et al.*, Fiz. Plazmy **25**, 851 (1999) [Plasma Phys. Rep. **25**, 783 (1999)].

13. V. S. Vorob'ev and S. P. Malyshenko, Zh. Éksp. Teor. Fiz. **111**, 2016 (1997) [JETP **84**, 1098 (1997)]; V. S. Vorob'ev, A. A. Eronin, and S. P. Malyshenko, Teplofiz. Vys. Temp. **39**, 107 (2001).

14. V. S. Vorob'ev, P. R. Levashov, I. V. Lomonosov, *et al.*, Preprint No. 1-448 (Institute for High Temperatures Scientific Association, Russian Academy of Sciences, Moscow, 2001); S. I. Tkachenko, K. V. Khishchenko, V. S. Vorob'ev, *et al.*, Teplofiz. Vys. Temp. **39**, 728 (2001).

15. F. Bennett, in *The Physics of High Energy Density*, Ed. by P. Caldirola and H. Knoepfel (Academic, New York, 1971; Mir, Moscow, 1974); M. M. Martynyuk and O. G. Panteleĭchuk, Teplofiz. Vys. Temp. **14**, 1201 (1976).

16. J. P. Chittenden, R. Aliaga-Rossel, S. V. Lebedev, *et al.*, Phys. Plasmas **4**, 4309 (1997).

17. G. V. Ivanenkov and W. Stepniewski, Fiz. Plazmy **26**, 24 (2000) [Plasma Phys. Rep. **26**, 21 (2000)].

18. G. V. Ivanenkov and W. Stepniewski, J. Mosc. Phys. Soc. **9**, 337 (1999).

19. K. Jach, *Komputerowe modelowanie dynamicznych odzialywan cial metoda punktow swobodnych* (PWN, Warsaw, 2001).

20. S. N. Kolgatin and A. V. Khachatur'yants, Teplofiz. Vys. Temp. **20**, 447 (1982).

21. E. Minguez, R. Munoz, R. Ruiz, and Y. Yague, Laser Part. Beams **17**, 799 (1999).

22. V. P. Skripov, *Metastable Liquids* (Nauka, Moscow, 1972).

23. V. L. Ginzburg and V. P. Shabanskiĭ, Dokl. Akad. Nauk SSSR **100**, 445 (1954); I. M. Lifshits, M. I. Kaganov, and L. V. Tanatarov, Zh. Éksp. Teor. Fiz. **31**, 232 (1956) [Sov. Phys. JETP **4**, 173 (1956)].

24. S. Kirkpatrick, Rev. Mod. Phys. **45**, 574 (1973).

25. V. E. Fortov and I. T. Yakubov, *Physics of Nonideal Plasma* (OIKhF AN SSSR, Moscow, 1984), Chaps. 4, 5.

26. V. S. Volokitin, I. O. Golosnoĭ, and N. N. Kalitkin, Mat. Model. **7** (4), 11 (1995).

27. S. Yu. Gus'kov, G. V. Ivanenkov, A. R. Mingaleev, *et al.*, Fiz. Plazmy **26**, 797 (2000) [Plasma Phys. Rep. **26**, 745 (2000)].

28. G. V. Ivanenkov, S. A. Pikuz, D. B. Sinars, *et al.*, Fiz. Plazmy **26**, 927 (2000) [Plasma Phys. Rep. **26**, 868 (2000)].

Translated by N. F. Larionova

Dynamics of the Implosion of a Tungsten Wire Array onto the Central Aluminum Wire

Yu. L. Bakshaev*, P. I. Blinov*, S. A. Dan'ko*, M. I. Ivanov, D. Klír***, V. D. Korolev*,
J. Kravárik***, J. Krása****, P. Kubeš***, V. I. Tumanov*, A. S. Chernenko*,
A. V. Chesnokov*****, and A. Yu. Shashkov*, and L. Juha******

*Russian Research Centre Kurchatov Institute, pl. Kurchatova 1, Moscow, 123182 Russia
**Research Institute of Pulsed Systems, Moscow, 115304 Russia
***Czech Technical University, Technická 2, 16627 Prague 6, Czech Republic
****Institute of Physics, Czech Academy of Sciences, Na Slovance 2, 18221 Prague 8, Czech Republic
*****Institute of Applied Physics and High Technologies, ul. Raspletina 4/1, Moscow, 123060 Russia
Received November 22, 2001

Abstract—Results are presented from the studies of the magnetic implosion of a tungsten wire liner onto an aluminum wire at currents of 2.0–2.6 MA. The experiments were carried out in the S-300 high-power pulsed facility at the Russian Research Centre Kurchatov Institute. The liner is composed of 50 wires 6 µm in diameter and 1 cm in length, which are equally spaced on a circle 1 cm in diameter. An aluminum wire 120 µm in diameter is positioned at the array axis. The liner implosion was accompanied by the generation of VUV and soft X-ray emission. The parameters of the pinch plasma produced during the liner implosion onto the aluminum wire were determined from the time-resolved spectral measurements by a five-channel polychromator. The ion and electron densities turned out to be equal to $n_i \approx 4 \times 10^{19}$ cm^{-3} and $n_e \approx 4 \times 10^{20}$ cm^{-3}, respectively, and the electron temperature was $T_e \approx 40$ eV. The radiation energy measured in the range 50–600 eV was 2–10 kJ. The sources of soft X-ray emission in hydrogen- and helium-like aluminum lines were the bright spots and local objects (clouds) formed in the plasma corona at an electron temperature of 200–500 eV and electron density of 10^{21}–10^{22} cm^{-3}. The possibility of both the generation of an axial magnetic field during the liner implosion and the conversion of the energy of this field into soft X-ray emission is discussed. © 2002 MAIK "Nauka/Interperiodica".
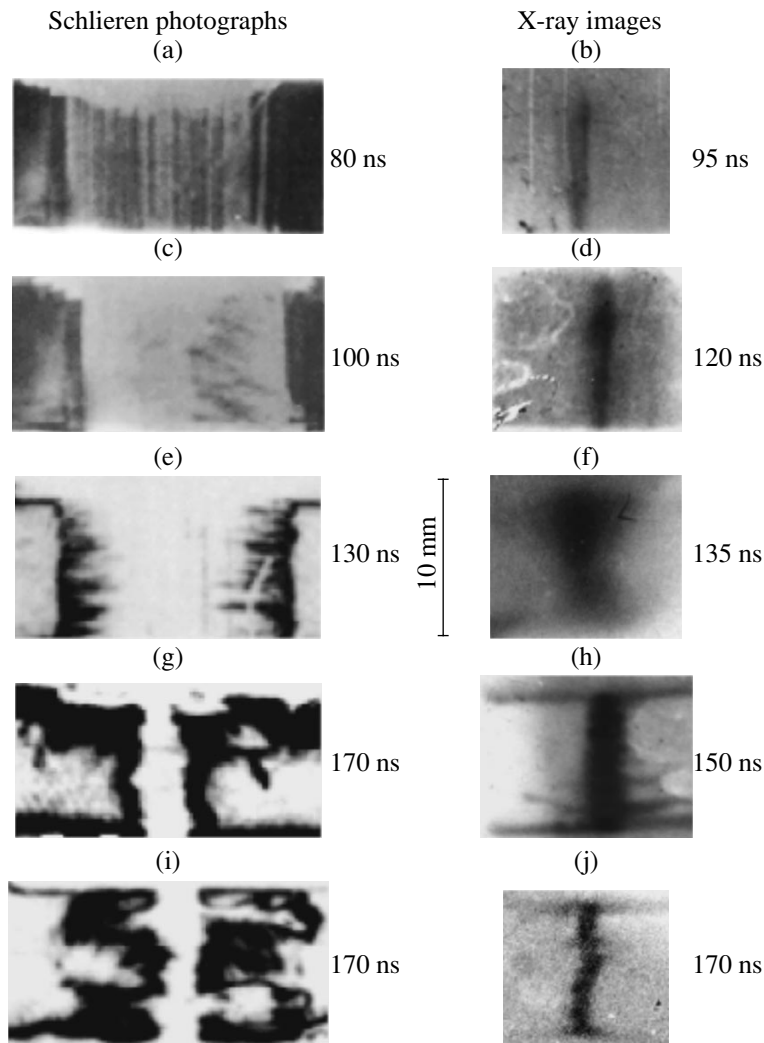
1. INTRODUCTION

High-density and high-temperature Z-pinches that form during the electrodynamic implosion of light liners are high-power sources of VUV and soft X-ray (SXR) emission [1, 2]. The implosion of gas puffs and wire arrays is achieved by using high-power current generators capable of producing 20-MA currents through the load with a rise time of 10^{14} A/s [3]. Most thermal radiation in the photon energy range from tens to hundreds of electronvolts is emitted from the corona, which is formed at the pinch axis in the phase of maximum compression. Only a few percent of the total radiation is emitted from unstable and randomly located hot spots. These spots are the sources of radiation with photon energies of several kiloelectronvolts. Recently, the results have been published of the measurements of the plasma corona formed during the implosion of the plasma-focus shell by a megaampere current onto a wire positioned at the discharge axis [4]. A fairly large diameter of the central aluminum wire used in these experiments was apparently a stabilizing factor, because the material of the central wire remained in the solid state [5], while the corona plasma was confined by the high magnetic field. High-energy photons were emitted from helical and annular structures [6]. The dense corona plasma can be used as an efficient SXR source, as well as an active medium for producing inverse population in recombination schemes proposed for creating X-ray lasers [7]. In our study, the parameters of the plasma generated during the implosion of a liner consisting of tungsten wires onto an aluminum wire 120 µm in diameter are investigated with the help of different diagnostics with a temporal, spatial, and spectral resolution. The experiments were carried out in the S-300 facility (4 MA, 70 ns) [8].

2. EXPERIMENTAL RESULTS

Experiments on studying the implosion of a tungsten liner onto an aluminum wire were carried out in the S-300 eight-module high-power pulsed facility generating a current in a load of up to 3 MA with a rise time of 100 ns. The cylindrical liner assembly 1 cm in diameter, consisting of 60–80 tungsten wires 6 µm in diameter and 1 cm in length, imploded onto an aluminum wire (120 or 250 µm in diameter), which was positioned at the liner axis. Information about the pinch dynamics was obtained with the following diagnostics:

Schlieren photographs

(a)

80 ns

(c)

100 ns

(e)

130 ns

(g)

170 ns

(i)

170 ns

X-ray images

(b)

95 ns

(d)

120 ns

(f)

135 ns

(h)

150 ns

(j)

170 ns

10 mm

Fig. 1. Schlieren photographs and X-ray images demonstrating the time evolution of the imploding plasma.

(i) optical photography with a streak camera observing the plasma in the radial direction with a slit oriented perpendicular to the central-wire axis (time resolution of 1 ns and space resolution of 0.05 mm) and three frame image converters recording the plasma images with an exposure time of 3 ns and intervals between frames of 10–15 ns;

(ii) frame-by-frame photography in the SXR range with the help of image converters with an exposure time of 3 ns;

(iii) X-ray measurements in the radial and axial directions with the help of two absolutely calibrated PIN diodes equipped with beryllium foils of thickness 100–300 μm and providing a temporal resolution of 3–4 ns, an SPPD11-04 semiconductor detector equipped with X-ray filters (100 and 300 μm Be and 10 μm mylar + 10 μm Al foils) and operating in the photon energy range 0.4–40 keV, and an SPPD11-02 detector equipped with 20-μm-thick copper filters and oper-

ating in the range 0.4–30 keV with a temporal resolution of ≤9 ns;

(iv) measurements of radiation in the photon energy range 0.1–4 keV by means of VUV diodes with gold cathodes (the spectral sensitivity of the diodes was equalized by using 0.1-μm films with a 0.01-μm deposited lead layer);

(v) X-ray measurements in the photon energy range 1–10 keV with an absolutely calibrated convex mica crystal spectrometer;

(vi) SXR photography with a two-pinhole camera (with two 100-μm-diameter pinholes filtered by mylar and aluminum foils) viewing the plasma in the radial direction;

(vii) study of the plasma dynamics with the use of two-frame laser shadow and schlieren photographs;

(viii) time-resolved measurements of the plasma X-ray emission spectrum with a five-channel polychro-
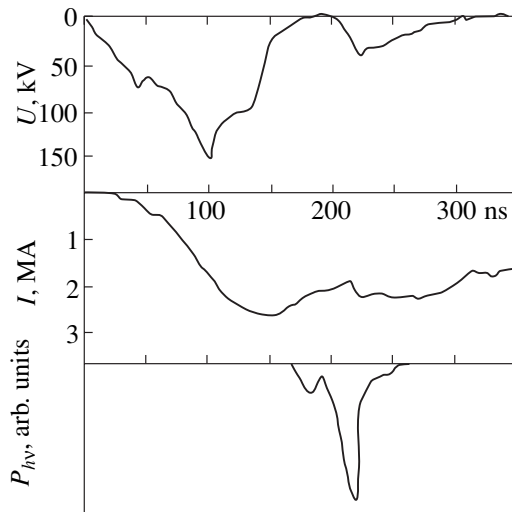
Fig. 2. Oscillograms of the voltage U, current I, and signal $P_{h\nu}$ from the radially viewing PIN diode filtered with a 100-μm-thick beryllium foil.

mator [9] in spectral ranges of 50–70, 90–180, 180–280, 280–400, and 400–900 eV; and

(ix) measurements of the time-integrated X-ray radiation with luminescent dosimeters.

The evolution of the liner implosion is shown in Fig. 1. The figure presents a series of photographs obtained with the schlieren diagnostics and X-ray frame cameras in different experiments. It can be seen in Fig. 1a that, 80 ns after the beginning of the current pulse, some wires are still in their initial positions. At that time, a radiating precursor forms at the axis of the liner (Figs.1b, 1d). Such a precursor was observed in many other experiments on the acceleration of hollow gas puffs and wire-array liners [10, 11]. The plasma precursor is formed by radial plasma flows originating on the tungsten wires and imploding toward the axis [12]. The existence of this precursor depends on whether or not a central wire is present in the discharge. Most of the wire mass is involved in implosion after the wires are completely evaporated at 90–100 ns after the current start (Fig. 1c). Then, the tungsten plasma accelerates to velocities of $(1–2) \times 10^7$ cm/s (Figs. 1c, 1f). At the end of implosion, by 160–180 ns after the current start, the plasma pinch reaches its minimum diameter. The value of the minimum diameter (1.5–3 mm) was estimated from the photographs obtained with the X-ray and optical image converters, the streak camera, and the schlieren diagnostics (Figs. 1g, 1h, 1i, 1j). The duration of the phase corresponding to the minimum pinch diameter was determined from the streak-camera images and turned out to be 5–30 ns. In the course of implosion, the current decreases and high-frequency oscillations and knees appear in the current pulse oscillogram; a sharp increase in the voltage (the second peak) measured with an Ohmic divider mounted at the output of the energy concentrator is also observed (Fig. 2).

During the implosion, we observed the generation of VUV and SXR pulses. Photons in the VUV spectral range corresponding to 10–40 eV were emitted over the entire surface of the liner. The semiconductor diodes filtered with beryllium foils of thickness 100–300 μm
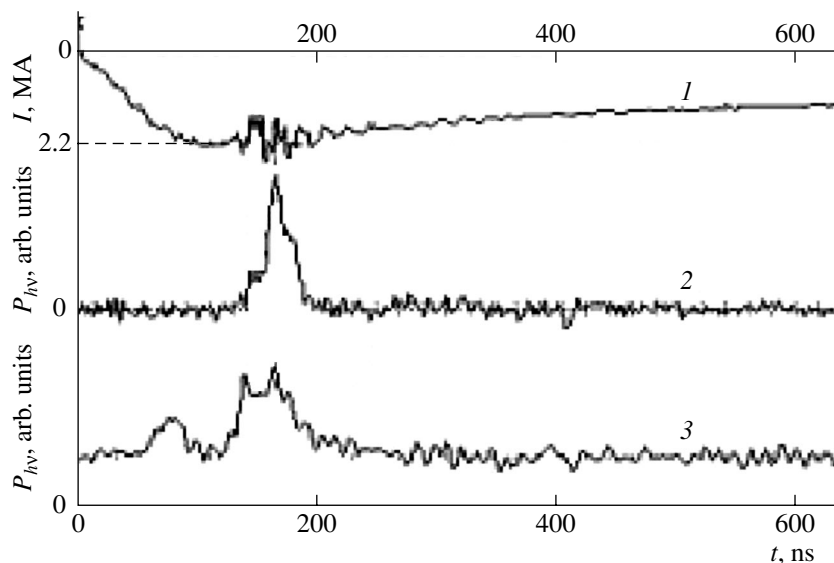
Fig. 3. Oscillograms of (*1*) the current and the signals from the (*2*) radially and (*3*) axially viewing PIN diodes filtered with 300-μm-thick beryllium foils (shot no. 00-10-7-1).

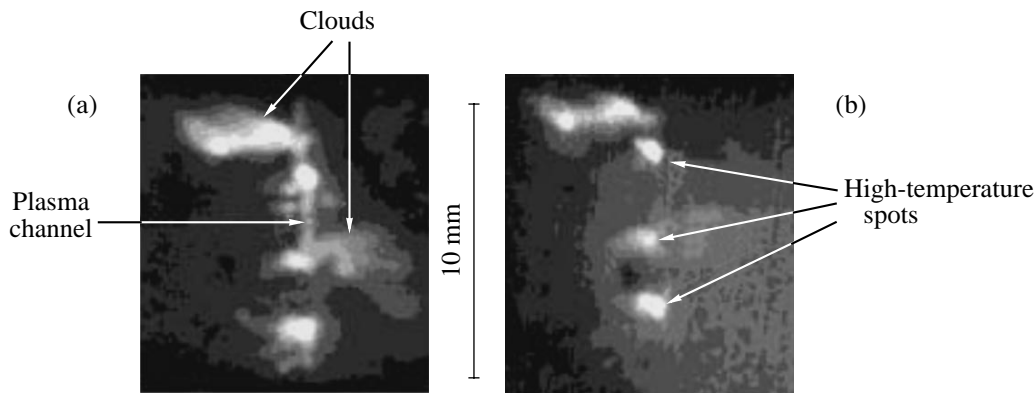**Fig. 4.** Pinhole images recorded with the use of mylar films of thickness (a) 1.5 and (b) 12 μm (shot no. 12-6-1).

(Fig. 3) detected SXR emission with photon energies of several kiloelectronvolts. The full width at half-maximum (FWHM) of the pulse was 20–40 ns, and the total energy and power were 5–20 J and 200–500 MW, respectively.

Figure 4 illustrates the pinhole-camera images of the radiating plasma. The radiation spectrum in a photon energy range of several kiloelectronvolts is shown in Fig. 5. The two-pinhole camera was filtered with 1.5- or 12-μm mylar film. The radiation recorded by the pinhole camera was emitted from the inner regions of the pinch. The 12-μm mylar foil absorbed the photons with energies below 700–800 eV, whereas the 1.5-μm mylar film absorbed the photons with energies of 300–400 eV. Figure 4a differs from Fig. 4b by the presence of a radiating plasma channel with the helical surface emitting the photons with energies below 700–800 eV. These radiating plasma channels were observed in nearly 50% of experiments. In the others experiments in which the radiating channels were absent, the pinhole camera with a thin foil recorded two to four bright spots.

Figure 5 shows the lines of the hydrogen- and helium-like aluminum ions, which correspond to photon energies of several kiloelectronvolts. These lines are emitted from the bright spots and clouds with a characteristic size of 1–4 mm. It should be noted that neither the radiating channels in the pinhole-camera images nor the aluminum lines were observed in experiments with the imploding liner when the central wire was absent. After the pinching phase, the compressed plasma expanded with a typical velocity of $(0.5–2.5) \times 10^7$ cm/s.

Figure 6 shows the typical oscillograms of the signals from the polychromator detectors operating in energy ranges of 90–180, 280–400, and 400–900 eV (shot no. 00-11-01-1). The time behavior of the radiated power for different photon energies for this shot is demonstrated in Fig. 7. The time dependences of the total radiation power and the temperature (in the range 50–600 eV) are shown in Fig. 8. SXR pulses with the largest amplitudes and photon energies lying in the range

100–150 eV were observed 120–180 ns after the current start. The total radiation energy in the range 50–600 eV amounted to 2–10 kJ. This energy was approximately the same both in the presence and in the absence of the wire at the liner axis and depended only slightly on the discharge current. It was found that the FWHM of the pulses detected in the different polychromator channels depended strongly on the photon energy (Fig. 9). For the VUV emission with photon energies of $h\nu < 50$ eV, the FWHM was ≈100 ns, whereas for higher energies, it was 50–80 ns for $h\nu \approx$ 60 eV, 30–50 ns for $h\nu \approx 120$ eV, and 15–30 ns for $h\nu \approx$ 600 eV. In the presence of the central aluminum wire, the FWHM of the pulses increased from 25 to 35 ns for the same radiation energy. In shot no. 00-11-01-1 (Fig. 6), two SXR pulses were recorded by the channel corresponding to a photon energy of 600 eV at a current of 2.4 MA. The FWHM of both pulses was about 20 ns, and the delay time of the second pulse was ≈20 ns.

The streak camera made it possible to observe the time evolution of the plasma corona in visible light in the direction transverse to the wire axis over 200 ns after the current start (in this case, the slit was oriented parallel to the electrodes and located at a distance of 4 mm from the faces of both electrodes). In Fig. 10
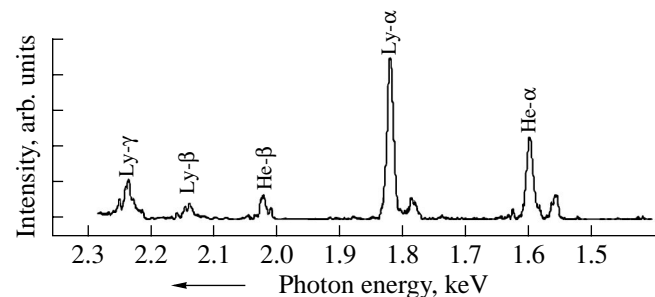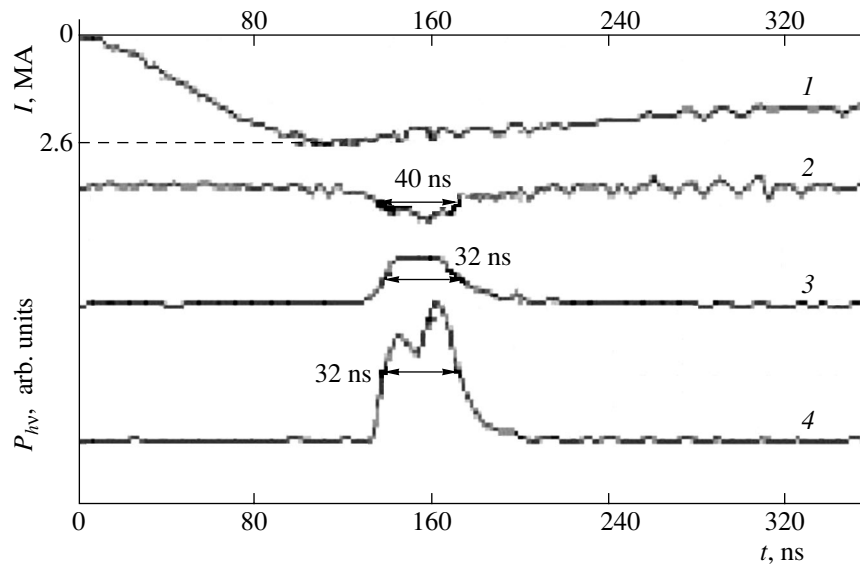

Fig. 5. X-ray spectrum for the upper spot in Fig. 4a (shot no. 12-6-1).

Fig. 6. Oscillograms of the (*1*) current and SXR pulses in the polychromator channels corresponding to photon energies of (*2*) 120, (*3*) 340, and (*4*) 600 eV (shot no. 00-11-01-1).

(shot no. 00-11-1-1), we can see that the implosion begins 100 ns after the current start. The liner is imploded over ≈ 50 ns with a velocity of $\sim 6 \times 10^6$ cm/s and reaches its minimum diameter equal to ≈ 1.7 mm.
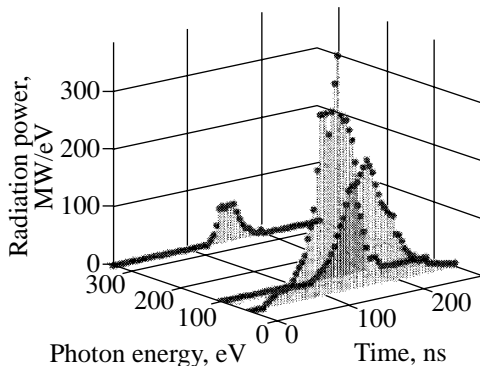
Fig. 7. Spectrum of the radiation power as a function of time and photon energy (shot no. 00-11-01-1).
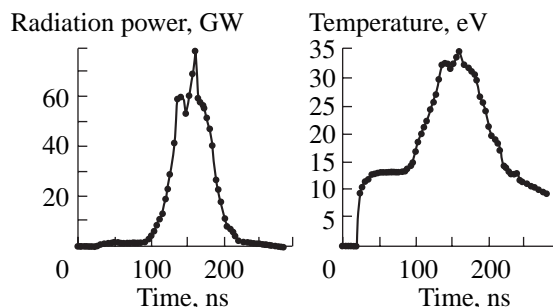
Fig. 8. Time dependences of the radiation power and the plasma temperature (shot no. 00-11-01-1).

Over the following 20 ns, the diameter remains unchanged; then, it increases to 4 mm over 10–15 ns, which corresponds to an expansion velocity of $(7–10) \times 10^6$ cm/s. Over the following 20 ns, the diameter again does not change; then, we observe the fast plasma expansion in the radial direction.

The intensity of VUV and SXR pulses generated during the implosion of a tungsten wire array was high enough to destroy 230-nm-thick polymethylmethacrylate and 350-nm-thick teflon films even when the samples were positioned at a fairly large distance (≈ 50 cm) from the source.

3. DISCUSSION

The implosion of the wire array starts after the tungsten wires evaporate (about 100 ns after the current start). The X-ray pulse corresponding to photon energies of about several kiloelectronvolts with a total energy of about 20 J is emitted from two to four clouds ≈ 1 mm in diameter in the pinch phase of implosion. This pulse was detected in the hydrogen- and helium-like aluminum lines. In the photon energy range of about several kiloelectronvolts, the FWHM of the pulse was 20–40 ns. The electron temperature and density were estimated from the line intensities of the spectral lines, assuming the plasma to be in thermal equilibrium, and were found to be 200–500 eV and $10^{21}–10^{22}$ cm^{-3}, respectively. In the pinhole images recorded with a 1.5-μm aluminized mylar foil, we can see two types of structures formed in the pinch core. These structures emit photons with energies above 200 eV. The structures of the first type are helical plasma channels, and the structures of the second type are bright spots 1–2 mm in diameter. The radiation in the spectral range corresponding to several kiloelectronvolts is

emitted from the spots and clouds. Probably, the clouds are formed by the explosion of the helical channels and the spots.

The plasma that is confined in the channels by the magnetic field has a lower temperature (about 70–100 eV) and a higher density in comparison with that in the clouds. The energy density in the channels is sufficient for this energy to be converted into radiation. The presence of the hydrogen- and helium-like aluminum lines in the liner spectrum evidences that the channels are formed in the corona of the central wire. The existence of helical channels indicates that an axial magnetic field can be generated in the wire corona. As a result, the plasma in the channels is compressed by this field and, then, is confined by the strong azimuthal magnetic field, as was suggested in [6]. Probably, the clouds of high-temperature plasma are formed due to the dissipation of magnetic energy.

The total radiation power in the range 50–600 eV and the ion temperature (of about ≈ 40 eV) were estimated by processing the SXR signals of shot no. 00-11-01-1 (Figs. 7, 8). The total radiation energy was determined from the measured signals in the absolutely calibrated polychromator channels, assuming that the X-ray flux is uniform over the solid angle 4π sr. The total electromagnetic energy in the range 50–600 eV was about 2–10 kJ both in the presence and in the absence of the wire on the liner axis and depended only slightly on the discharge current. Almost the same values of the total energy (about 2–8 kJ) in the spectral range 0.1–4 keV were obtained from the measurements with VUV diodes with gold cathodes in combination with thin 0.1-μm foils with a deposited lead layer. The radiation power in this photon energy range attained 2×10^{11} W.

The average ion density can be estimated from the values of the total mass of the tungsten liner (250 μg) and the pinch radius (≈ 1 mm). The plasma temperature in the pinch was estimated at 40 eV, assuming the pinch radiation to be blackbody radiation with a maximum energy of 120 eV. Taking into account that, according to the Saha equation, the degree of ionization is $Z \approx 10$, we can estimate the electron density as $n_e \approx 4 \times 10^{20}$ cm^{-3}. This estimate corresponds to a thermal pressure in the pinch of 2×10^9 Pa. At the same time, for a current of 2 MA, the azimuthal magnetic field in the compression phase is on the order of 2×10^6 G, which corresponds to a magnetic pressure of 2×10^{10} Pa. This points to the fact that the magnetic energy can play a dominant role in the pinch dynamics. The hypothesis of the conversion of the internal magnetic field into VUV and SXR emission is confirmed by the streak-camera images of two compression phases shown in Fig. 10, which illustrates the change in the pinch diameter from 2 to 5 mm during the period of magnetic confinement. Apparently, in this case, the configuration of the magnetic field changes abruptly. These two phases correlate in time with two peaks of X-ray emission with a photon energy of 600 eV (see Fig. 6). They are observable due to their
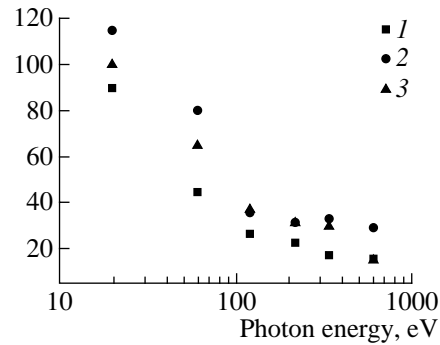
Fig. 9. FWHM of the VUV and SXR pulses as a function of the photon energy (*1*) in the absence of a central wire, (*2*) with an Al central wire 100 μm in diameter and (*3*) with a C central wire 100 μm in diameter.
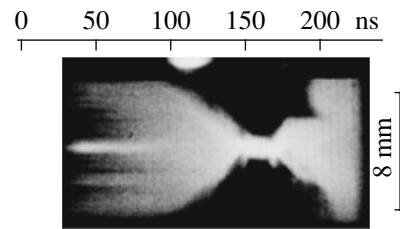
Fig. 10. Streak-camera image of the tungsten wire array (shot no. 00-11-01-1).

short FWHM. In the range 50–300 eV, both phases are not separated.

For an electron temperature of 40 eV, density of $\approx 4 \times 10^{20}$ cm^{-3}, and degree of ionization of 10, we can estimate the Spitzer conductivity as $\sigma \sim 10^4$ Ω^{-1} m^{-1}. This value is one order of magnitude lower than that calculated assuming the Joule heating (in this case, the radiation energy is $(2–10) \times 10^4$ J) or determined from the duration of the compression phase (20–30 ns), which is governed by the magnetic-field diffusion. Apparently, a conductivity of $\sim 10^5$ Ω^{-1} m^{-1} is a more appropriate estimate.

The disturbance of the balance between the magnetic pressure B_φ^2 and the thermal pressure may be attributed to the generation of a chaotic magnetic field [13]. The chaotic magnetic field may be generated due to the transformation of a fraction of the azimuthal component B_φ of the pinch magnetic field into the radial B_r and azimuthal B_z components. This transformation may be caused by the inhomogeneity of the plasma density in the pinch regions where the azimuthal magnetic field exists and the electric current flows [14]. The formation of helical plasma channels is indirect evidence of the generation of the axial mag-

netic field. The high values of the photon energy and the power of thermal emission from the plasma are probably related to the fast transformation of the axial component of the magnetic field, generation of high electric fields, and acceleration of electrons.

4. CONCLUSION

Thermal VUV emission and SXR emission in a photon energy range of several kiloelectronvolts are generated in the pinch phase of the liner implosion. The thermal radiation is emitted from the pinch column with a temperature of ≈ 40 eV and an electron density of $\approx 4 \times 10^{20}$ cm^{-3}. The SXR pulse with a FWHM of 20–40 ns is generated in the wire corona, specifically, in two to four high-temperature spots and clouds 1–2 mm in diameter. The total radiation energy emitted in the hydrogen- and helium-like aluminum lines in the spectral range on the order of several kiloelectronvolts amounts to ≈ 20 J. The electron temperature and the electron density calculated from the line intensities are 200–500 eV and 10^{21}–10^{22} cm^{-3}, respectively. These values are close to the plasma parameters required to produce an inverse population in a recombining aluminum plasma. As to the plasma structure, it is necessary to continue experimental studies of the possibility of creating an extended homogeneous plasma and to choose the optimum initial Z-pinch configuration.

A disturbance of the balance between the magnetic and thermal pressures in the pinch may be attributed to the generation of a chaotic magnetic field. As a result, both the radial and axial components of the magnetic field are generated during the liner plasma implosion. The subsequent conversion of the energy of the chaotic magnetic field into thermal energy results in an additional pressure. It seems plausible that some fraction of the pinch plasma is confined by the magnetic field in the helical structures. The high-energy emission from the plasma may be attributed to the fast transformation of the axial component of the magnetic field, which results in the generation of high electric fields and electron acceleration.

ACKNOWLEDGMENTS

REFERENCES

1. T. W. L. Sanford, R. B. Spielman, G. O. Allshouse, *et al.*, IEEE Trans. Plasma Sci. **26**, 1086 (1998).
2. I. K. Aĭvazov, M. B. Bekhtev, V. V. Bulan, *et al.*, Fiz. Plazmy **16**, 645 (1990) [Sov. J. Plasma Phys. **16**, 373 (1990)].
3. D. D. Ryutov, M. S. Derzon, and M. R. Matzen, Rev. Mod. Phys. **72**, 167 (2000).
4. M. Scholz, M. Paduch, K. Tomaszewski, *et al.*, Czech. J. Phys. **50**, Suppl. 3, 150 (2000).
5. N. A. Bobrova, T. L. Razinkova, and P. V. Sasorov, Fiz. Plazmy **18**, 517 (1992) [Sov. J. Plasma Phys. **18**, 269 (1992)].
6. P. Kubeš, J. Kravárik, Yu. L. Bakshaev, *et al.*, Fiz. Plazmy **28**, 329 (2002) [Plasma Phys. Rep. **28**, 296 (2002)].
7. R. C. Elton, *X-ray Lasers* (Academic, Boston, 1990; Mir, Moscow, 1994).
8. A. S. Chernenko, Yu. M. Gorbulin, Yu. G. Kalinin, *et al.*, in *Proceedings of the 11th International Conference on High Power Particle Beams, Prague, 1996*, Ed. by K. Jungwirth and J. Ulschmied (Inst. of Plasma Physics, Acad. of Sci. Czech Rep., Prague, 1996), Vol. 1, p. 154.
9. A. S. Chernenko, P. I. Blinov, S. A. Dan'ko, *et al.*, Czech. J. Phys. **50**, Suppl. 3, 91 (2000).
10. I. K. Aĭvazov, V. D. Vikharev, G. S. Volkov, *et al.*, Pis'ma Zh. Éksp. Teor. Fiz. **45**, 23 (1987) [JETP Lett. **45**, 28 (1987)].
11. S. L. Bogolyubskiĭ, A. G. Volkov, E. M. Gordeev, *et al.*, Pis'ma Zh. Tekh. Fiz. **13**, 901 (1987) [Sov. Tech. Phys. Lett. **13**, 375 (1987)].
12. V. V. Aleksandrov, A. V. Branitskiĭ, G. S. Volkovich, *et al.*, Fiz. Plazmy **27**, 99 (2001) [Plasma Phys. Rep. **27**, 89 (2001)].
13. Yu. L. Bakshaev, P. I. Blinov, A. S. Chernenko, *et al.*, in *Proceedings of the 17th Conference on Fusion Energy, Yokohama, Japan, 1998*, Vol. 3, p. 879.
14. L. A. Artsimovich and R. Z. Sagdeev, *Plasma Physics for Physicists* (Atomizdat, Moscow, 1979), p. 320.

Translated by N. F. Larionova

Weakly Ionized Plasma in a Supersonic Plasma Flow

V. A. Pavlov

St. Petersburg State University, Universitetskaya nab. 7/9, St. Petersburg, 199164 Russia
Received June 28, 2001; in final form, January 25, 2002

Abstract—The structure of the ion acoustic precursor of a shock wave in a weakly ionized collision-dominated plasma is studied numerically. It is shown that the simultaneous action of the nonlinearity, dispersion, and dissipation leads to the formation of an oscillating profile of the ion density in the precursor. There exist regimes in which the charged-particle density decreases abruptly and simultaneously the number of maxima in its profile within the precursor becomes smaller as the shock wave velocity increases in a jumplike manner. This effect is analogous to the corresponding hydrodynamic effect in narrow shallow channels (the "Houston's horse" effect). In the stage preceding this jumplike process, local regions may appear in which the degree of plasma ionization is elevated. Such plasma "bunches" give rise to the strong reverse action of the charged particles on the neutral component, resulting in the "stretching" of the precursor. This phenomenon is resonant in character and occurs in a narrow range of shock wave velocities. © *2002 MAIK "Nauka/Interperiodica".*

In recent years, there has been much interest in the nonlinear processes in weakly ionized plasmas. Thus, the related topics have been the subject of regular international conferences such as the Workshops on Weakly Ionized Plasmas (Norfolk, VA, 1997–2001), the Workshops on Magnetoplasma Aerodynamics in Aerospace Applications (Moscow, 1999–2001), and the Workshops on Thermochemical Processes in Plasma Aerodynamics (St. Petersburg, 2000–2001). An interesting problem in this line of research is that of studying the plasma structure in a supersonic flow, whose velocity is higher than the ion acoustic speed. The plasma precursor that forms ahead of a shock wave has a number of "exotic" features [1, 2].

The problem will be treated in a formulation analogous to that in [1, 2]. Specifically, we investigate a one-dimensional steady-state plasma precursor of a strong shock wave. We assume that the precursor structure depends on the combination $z - ct$, where z is the coordinate, t is the time, and $c = $ const is the shock wave velocity. We also assume that the electron and ion temperatures ahead of the shock front satisfy the condition $T_e \gg T_i$, which refers to the ion acoustic approximation. Taking into account the nonlinearity, elastic collisions, dispersion, ion viscosity, and electron heat conduction, we can obtain the following equation for the dimensionless velocity of the ion plasma component, $V_i = w/c$ (where w is the dimensional ion velocity) ahead of the shock front [2]:

$$\frac{d^3 V_i}{dx^3} d^2 = (1 - V_i)\frac{d^2 V_i}{dx^2} MA$$

$$+ 0.5[M^2(1 - V_i) - (1 - V_i)^{-1}]\frac{dV_i}{dx} - 0.5 V_i M. \quad (1)$$

Here, $x = \xi_1^{-1}(z - ct)$, $\xi_1 = V_s \nu^{-1}$, V_s is the ion acoustic speed, ν is the effective frequency of collisions between the ions and neutrals (the effect of electron heat conduction is incorporated into the representation of ν [1]), $d = D\xi_1^{-1}$, D is the electron Debye radius, $A = 0.5\sqrt{5}T_i T_e^{-1}$ is the dimensionless ion viscosity coefficient, and $M = cV_s^{-1}$ is the ion Mach number. The dimensionless ion density in a steady-state shock wave is represented as $n_i = n_i/n_{i0} = (1 - V_i)^{-1}$, where the zero subscript denotes unperturbed parameter values. Equation (1) was derived under the assumption that the reverse action of the charged particles on neutrals is negligible. In this approximation, there are upper limits on the amplitude of the ion density perturbations and on the degree of plasma ionization. As will be seen below, Eq. (1) admits solutions describing the appearance of regions in which the degree of plasma ionization becomes elevated under certain conditions. Of course, in order to provide a correct description of the fields in these regions, where the reverse action of the charges on the neutral component and on the shock wave itself is strong, the model should be refined to include the self-consistent interaction between the neutral and charged plasma components.

It should be noted that Eq. (1) fails to correctly describe the processes occurring in the plasma in the region $x < 0$ (behind the shock front): in this region, the above condition of the ion acoustic approximation is violated, so that the corresponding equation, in contrast to Eq. (1), contains an external source term accounting for the field of the shock wave of the neutral component. Instead of the closed problem with an external source on the interval $-\infty < x < \infty$, we will solve the corresponding approximate Cauchy problem on the

interval $0 \le x < \infty$ under the assumption that, in the region $x < 0$, the ions are totally entrained by neutral particles. The results obtained in this way are approximations to the solutions to the closed problem with a source.

In order to solve Eq. (1) in the region $x \ge 0$, it is necessary to formulate three boundary conditions. The condition required for solving the equation analytically is imposed ahead of the shock front at infinity: $V_i(\infty) = 0$, which corresponds to a limiting transition to the unperturbed state. The remaining two boundary conditions should ensure the "matching" of the fields at the shock front. They can be derived from the solution to the closed problem in the region behind the front ($x < 0$). However, instead of doing so, we formulate the second boundary condition approximately. The assumption that the charges are totally entrained by the front of a strong shock wave gives $V_i(0) \approx 2(\gamma + 1)^{-1}$, where $\gamma \approx 1.4$ is the ratio of the specific heat capacities. In this approximate approach, the third boundary condition is difficult to formulate, because it may be chosen in different ways, e.g., as a selection rule reflecting a certain feature.

For the numerical integration of Eq. (1) by the Runge–Kutta method (based on the rkadapt Matcad 8/2000 software package), all of the three boundary conditions were imposed at the initial point $x = 0$ so as to provide the limiting transition $V_i \longrightarrow 0$ as $x \longrightarrow \infty$. This indicates that the two conditions on the derivatives $V_i'(0)$ and $V_i''(0)$ should simultaneously ensure the limiting transition to the unperturbed state at infinity and the rule for selecting the solution. It should be noted that, with $d = 0$ and $A = 0$, Eq. (1) is a first-order differential equation, in which case, however, the solution to the physical problem in question should satisfy the two boundary conditions, $V_i(0)$ and $V_i(\infty) = 0$. For $M < 1$, Eq. (1) has a continuous solution. In contrast, for $M > 1$, a zero boundary value at infinity, $V_i(\infty)$, can only be achieved by introducing a discontinuity [2]. In the plasma precursor, the discontinuity is smoothed by the dispersion ($d \ne 0$) and viscosity ($A > 0$) effects.

The general solution to Eq. (1) can be represented as

$$V_i = C_1 f_1 + C_2 f_2 + C_3 f_3. \qquad (2)$$

Here, $C_n = \text{const}$; the function f_1 decreases asymptotically at infinity; $f_1 \propto \exp(-x x_0^{-1})$; the remaining two functions increase without bound at infinity, $f_2, f_3 \longrightarrow \infty$

as $x \longrightarrow \infty$, and x_0 is a positive root of the dispersion relation

$$d^2 = x_0[MA - 0.5(M^2 - 1)x_0 - 0.5Mx_0^2]. \qquad (3)$$

Thus, in the absence of dispersion ($d \longrightarrow 0$), we obtain the representation

$$x_0 = \sqrt{\left(\frac{M^2 - 1}{2M}\right)^2 + 4A} - \frac{M^2 - 1}{2M} > 0. \qquad (4)$$

We are interested in such solutions to Eq. (1) that have the form $V_i = C_1 f_1$, $C_2 = C_3 \equiv 0$. Because of a certain (finite) inaccuracy of numerical integration, special measures should be taken in order to prevent the appearance of the terms with f_2 and f_3 in the region $x > x_0$. We denote by x_m the maximum value of x in numerical calculations (in a theoretical analysis, we have $x_m = \infty$). If we increase the numerical value x_m, we must simultaneously increase both the accuracy with which to choose the $V_i'(0)$ and $V_i''(0)$ boundary values (the $V_i(0)$ value is fixed and thus cannot be changed) and the number of integration steps in order to satisfy the condition $V_i(x_m) \longrightarrow 0$. It is this procedure that ensures the above zero boundary values at infinity for any ion Mach number. Without refinement of the boundary values $V_i'(0)$ and $V_i''(0)$, an increase in x_m will be accompanied by an increase in $V_i(x_m)$ because of the strong effect of f_2 and f_3 at a fixed accuracy of $V_i'(0)$ and $V_i''(0)$ in the region $x > x_0$. In calculations, not only the boundary condition $V_i(x_m) \longrightarrow 0$ was controlled but also the true shape of the exponential asymptotic profile $V_i \propto \exp(-x x_0^{-1})$ was checked. With increasing x_m, the phase trajectory in phase space (V_i, V_i', V_i'') approached the origin of the coordinates according to the asymptotic law $V_i \propto \exp(-x x_0^{-1})$.

Without using the rule for selecting a solution, it is possible to construct a number of solutions such that $V_i \longrightarrow 0$ as $x_i \longrightarrow \infty$ by specifying all of the three boundary conditions at the point $x = 0$. In order to illustrate different possible ways of constructing the solution, Figs. 1 and 2 show the profiles $n_i = n_i(x)$, having five maxima and three maxima, respectively. The profiles, which were calculated for $M = 1.3$, $d = 0.05$, and $A = 0$, show that different types of precursors can, in principle, be formed at the same values of the Mach number and at the same levels of dispersion and viscosity by different excitation mechanisms, namely, by creating different boundary conditions at the shock front $x = 0$ that ensure an unperturbed state at infinity ($x = \infty$). In this case, the question of whether different precursors can actually be formed at the same d, A, and M values remains open.

The rule for selecting a solution to the physical problem at hand can be formulated on the basis of the properties of the exact analytic solution to Eq. (1) with $d = 0$ and $A = 0$. In this situation, we arrive at the following representations at the shock front:

$$V_i(0) = 5/6, \quad V_i'(0) = -5M(36 - M^2)^{-1},$$
$$V_i''(0) = 30M^2(36 - M^2)^{-2}. \tag{5}$$

The related function $n_i(x)$ is shown in Fig. 3. In the region $x \approx 1.29$, there are discontinuities in the functions V_i and $n_i(x)$, in which case the higher derivatives in Eq. (1) come into play in order to smooth the discontinuities in the situation with $d \neq 0$ and $A > 0$. As a result, in this region inside the precursor, the ion density profile should become the steepest and there should be inflection points of the corresponding curves. This case corresponds to the profile shown in Fig. 1. Let us analyze how this solution changes as the ion Mach number M increases. Figure 4 shows the dependence of the maximum value n_{max} of the dimensionless density on M; here, the parameter $N = 5, 4, 3, 2, 1$, and 0 is the number of maxima in the ion density within the precursor. For $M < 1.47$, there exists a precursor with five maxima. As $M \longrightarrow 1.47$, the perturbation amplitude grows without bound, in which case it is necessary to refine the model. The transformation of the solution in the range $M > 1.47$ can be interpreted as follows. We suppose that some possible fluctuations of the shock wave velocity cause no significant energy transfer to the system. Under this assumption, the onset of fluctuations with Mach numbers close to $M = 1.47$ can lead to an abrupt change in the boundary value $V_i''(0)$. This effect should manifest itself as the appearance of the $n_i(x)$ profile with four maxima, in which case the profile of the perturbed ion density sharply rearranges—the number of maxima per unit length reduces and the value n_{max} decreases abruptly. (It should be stressed that, in regimes with $M < 1.47$, the nonlinear system is fairly fluctuation-resistant, so that the fluctuations do not change the fields qualitatively.) This phenomenon is a plasma analogue of the so-called Houston's horse effect in hydrodynamics. For a plasma, this effect was predicted for the first time in my earlier paper [2] on the basis of analytic estimates. In the range $M \geq 1.52$, a solution can be constructed that has an even smaller number of maxima, namely, three maxima. A further increase in M up to 1.56 leads to a similar situation: first, the value n_{max} increases; then, for $M \geq 1.56$, the boundary value $V_i''(0)$ changes abruptly, thereby making it possible to construct a solution with two maxima; and so on. Finally, for $M \geq 1.70$, the last plasma bunch collapses completely and the ion density profile becomes monotonic. In Fig. 4, the dashed curves illustrate the states that occur as the Mach number decreases; the maximum density n_{max} is seen to change monotonically. If we restrict ourselves to fluctuations
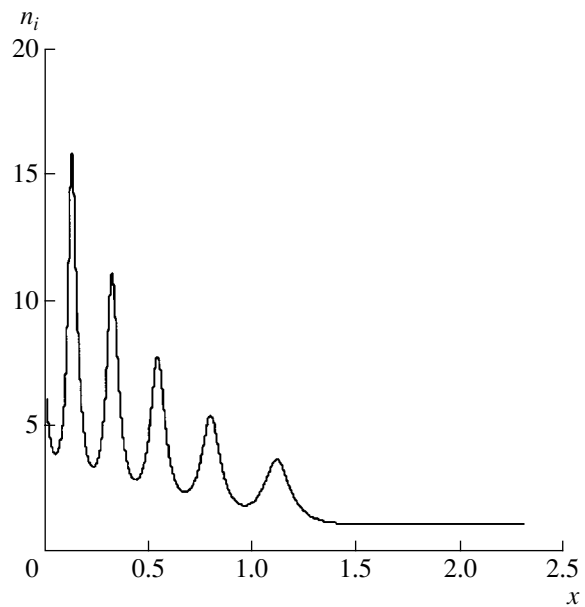
Fig. 1. Profile $n_i(x)$ at $M = 1.3$, $A = 0$, and $d = 0.05$ for boundary conditions $V_i(0) = 5/6$, $V_i'(0) = -3.883149$, and $V_i''(0) = 37.343069$.
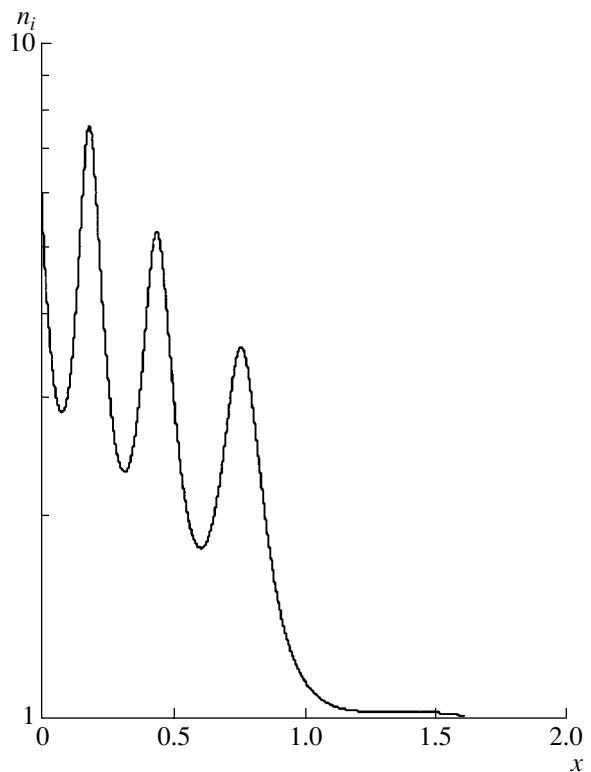
Fig. 2. Profile $n_i(x)$ at $M = 1.3$, $A = 0$, and $d = 0.05$ for boundary conditions $V_i(0) = 5/6$, $V_i'(0) = -3.539449$, and $V_i''(0) = -37.6539314$.
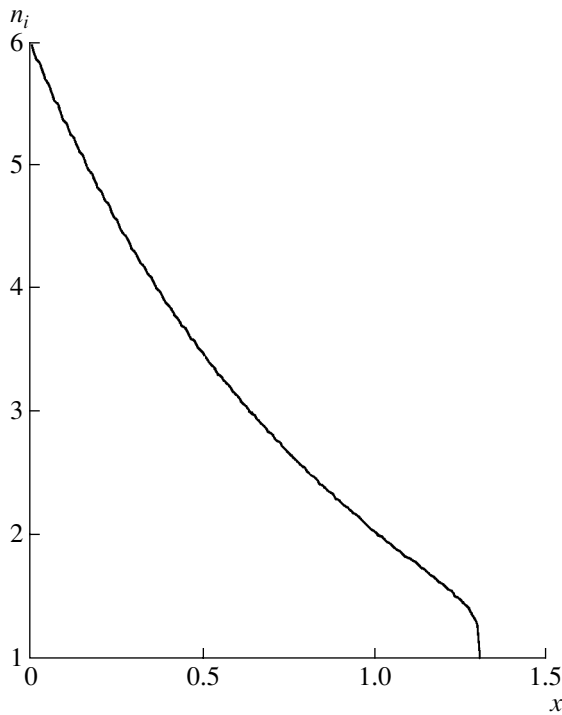
Fig. 3. Profile $n_i(x)$ at $M = 1.3$, $A = 0$, and $d = 0$.

that cause no significant energy transfer to the system, then we can see that, as M decreases, the fields do not change qualitatively. Thus, the system exhibits a peculiar hysteresis effect with respect to a decrease and an increase in M. This indicates that, as the Mach number decreases from the value characteristic of the state in which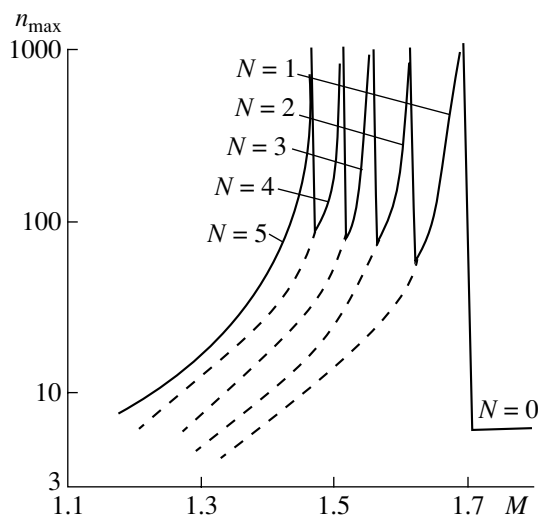 the ion density profile has less than five maxima, the maximum density n_{max}, first, decreases in the downward direction along a solid curve and, then, changes along a dashed curve. Of course, when the nonlinear system described by Eq. (1) is subjected to specially created nonautonomous forces, the hysteresis effect can be eliminated at the expense of the external energy.

With allowance for viscosity, the effect under consideration takes place at higher Mach numbers M. In this case, the highest peak in the ion density profile changes its position: it can occur either in the leading or trailing edge of the precursor. Figure 5 shows the profiles $n_{max} = n_{max}(M)$ calculated for the conditions typical of steady glow discharges in experiments on anomalous gas flows in ballistic devices [3]: the pressure is $P = 40$ torr, the degree of ionization is about $\alpha \sim 5 \times 10^{-6}$, the ion temperature is $T_i \sim 1500$ K, and the electron temperature is $T_e \sim 1$ eV. With these parameters, the above two dimensionless coefficients are equal to $d = 0.05$ and $A = 0.13$. It is of interest to note that the resonance effect is pronounced even when the dissipation is strong. The ion density increases considerably only in a narrow range of Mach numbers, so that we may speak of a peculiar nonlinear resonance. It should be noted that, in the stage preceding the Houston's horse effect, a local region appears in which the degree of plasma ionization is elevated. In this region, one of the assumptions made in deriving Eq. (1) is violated (i.e., the assumption that the self-consistent interaction between the neutral and charged plasma components is negligible), so that the model should be appropriately refined. Although the problem in a refined formulation has not
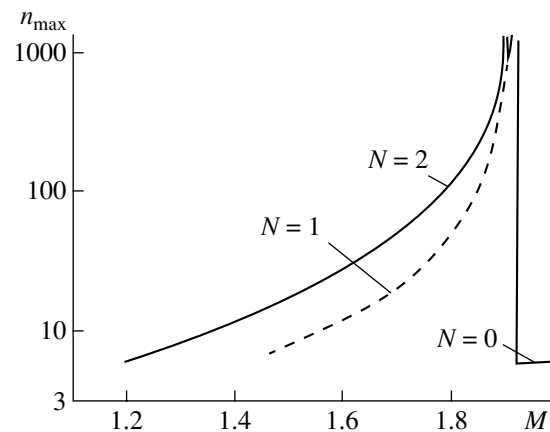

Fig. 4. Dependence $n_{max}(M)$ at $A = 0$ and $d = 0.05$ (N is the number of maxima within the precursor).

Fig. 5. Dependence $n_{max}(M)$ at $A = 0.13$ and $d = 0.05$ (N is the number of maxima within the precursor).

yet been solved rigorously, we can estimate the spatial scale of the perturbed region in question:

$$\xi_2 \approx a\nu^{-1} \approx (V_s\sqrt{T_n T_e^{-1}})\nu^{-1}(n_n n_i^{-1})_0$$
$$\approx \xi_1\sqrt{T_n T_e^{-1}}(n_n n_i^{-1})_0, \qquad (6)$$
$$\sqrt{T_n T_e^{-1}}(n_n n_i^{-1})_0 > 1,$$

where $\xi_1 \approx \nu^{-1}V_s$ is the characteristic spatial scale in the situation when the charged particles do not have the reverse effect on neutrals and a is the speed of sound. The reverse action of the charged component on the neutral component results in the stretching of the precursor of a shock wave.

REFERENCES

1. V. A. Pavlov, Fiz. Plazmy **22**, 182 (1996) [Plasma Phys. Rep. **22**, 167 (1996)].
2. V. A. Pavlov, Fiz. Plazmy **26**, 543 (2000) [Plasma Phys. Rep. **26**, 507 (2000)].
3. V. A. Pavlov and Yu. L. Serov, in *Reports of the 2nd Workshop on Magnetoplasma Aerodynamics in Aerospace Applications, Moscow, 2000*, p. 125.

Translated by G. V. Shepekina

<div align="center">

NONIDEAL
PLASMA

Suppression of the Dissociative Phase Transition in Plasma Mixtures of Molecular and Noble Gases

</div>

M. Bonitz*, P. R. Levashov**, I. A. Mulenko***, E. N. Oleĭnikova***, V. S. Filinov**,
V. E. Fortov**, and A. L. Khomkin***

*Faculty of Physics, University of Rostock, Germany
**High Energy Density Research Institute, Russian Academy of Sciences,
Izhorskaya ul. 13/19, Moscow, 127412 Russia
***Institute for High Temperatures Scientific Association, Russian Academy of Sciences,
ul. Izhorskaya 13/19, Moscow, 127412 Russia

Abstract—The thermodynamic properties of a hydrogen–helium plasma are calculated both by the quantum Monte Carlo method and by using a chemical model. It is shown that the previously observed anomalous behavior of the isotherms of superdense molecular gases (the so-called dissociative phase transition) is suppressed in plasma mixtures of molecular and noble gases. © 2002 MAIK "Nauka/Interperiodica".

1. INTRODUCTION

In [1, 2], the thermodynamic parameters of a superdense plasma of molecular gases were calculated both by the quantum Monte Carlo method [3] and by using the chemical model of a nonideal chemically reacting plasma [4, 5]. In both cases, simulations showed the anomalous behavior of the isotherms of a superdense hydrogen plasma in the submegabar and megabar pressure ranges. Calculations by the chemical model showed that, under certain conditions, a van der Waals loop characteristic of the gas–liquid phase transition appears in the phase diagram of a molecular gas plasma. The typical values of the critical temperature T_c turned out to be on the order of the dissociation energy of molecules or molecular ions, depending on what particles are dominant in the region where the temperature is close to the critical temperature. Numerical simulations by the quantum Monte Carlo method also showed the presence of a loop typical of phase transitions. It should be noted that an abrupt change in density is accompanied by an abrupt change in the plasma composition. The anomalous behavior observed was called the dissociative phase transition, because, when going over along the spinodal from the rarified phase to the dense one, the molecule density decreases sharply (by nearly five to seven orders of magnitude) due to the intense dissociation caused by the high pressure.

At the same time, for noble-gas plasmas, calculations by the chemical model demonstrate the monotonic behavior of the isotherms as the specific volume decreases. Although the interaction between plasma particles is rather strong, the calculated values of the thermodynamic parameters differ only slightly from those predicted by the ideal-gas model, as was pointed out in [5]. Since there are no molecules in a noble-gas

plasma, no anomaly is observed in the isotherms of this plasma. In this context, the question arises as to the character of the phase diagrams of mixtures containing molecular and noble gases. Intuitively, it is clear that the anomalous effects observed in [1, 2] should disappear as the mole fraction of the noble gas in the mixture increases.

The objective of this paper is to illustrate how the dissociative phase transition in the plasma mixture of a molecular and noble gas is suppressed as the noble gas fraction in the mixture increases. As an example, the thermodynamic properties of a superdense hydrogen–helium plasma are calculated both by the quantum Monte Carlo method and by using the chemical model of a multicomponent plasma. An analysis of the calculation results obtained by using both approaches allows us to conclude that the phase transition gradually disappears as the helium fraction in the mixture increases.

## 2. RESULTS OF ANALYTICAL AND NUMERICAL CALCULATIONS

In this paper, we do not describe the calculation procedures, because they are described in detail in [3–5]. We only note their basic points.

When calculating by the quantum-mechanical Monte-Carlo method, we selected a system of 100 nuclei; the number of seed electrons was given by the ratio of the hydrogen and helium mole fractions in the mixture. The thermodynamic quantities were calculated as the logarithmic derivatives of the statistical sum [6]. The statistical sum of the quantum system was expressed through the density matrix, which was approximately represented in the form of integrals over trajectories [3, 6].

The chemical model is based on the separation of the spectrum of free and bound states of the Coulomb and neutral subsystems of the plasma. The Coulomb corrections to the thermodynamic functions were calculated as exact asymptotic expansions in terms of the activity powers in the grand canonical ensemble [4]. When calculating the atomic statistical sum, we used the nearest neighbor approximation. The corrections for the interactions with the participation of neutrals were written as a series expansion in terms of the density with allowance for all the types of charge–neutral and neutral–neutral binary and triple interactions [5]. The second and third virial coefficients due to the interaction of different types of free particles were calculated in [7] for the Hill pseudopotentials [8] constructed on the initial Lennard-Jones potentials (12-6) and (12-4).

By using previously developed procedures of calculating the thermodynamic properties of a nonideal plasma, we analyze their behavior on the phase diagram for a hydrogen–helium mixture over a wide range of densities and temperatures. First, we present the results of calculations obtained by the chemical model. Their analysis seems to be more convenient and simple and provides the possibility of obtaining a large body of information. Then, we compare these results with the quantum-mechanical Monte Carlo method. The results of the latter are most important and demonstrative, because they can be regarded as a numerical experiment. However, in this method, it is rather difficult to obtain a large body of numerical data because of serious computational problems. For this reason, calculations were performed for some isotherms with certain specified compositions (He : H = 7 : 93 and 33 : 67).

We consider a nonideal muticomponent hydrogen–helium plasma. We specify the plasma components as e^-, H, H^+, H^-, H_2, H_2^+, He, He^+, He^{++}, He_2^+, and HeH^+. The other possible components can be omitted because of the low probability of their formation. In calculations, we varied the mass density ρ, the plasma temperature T, and the mole fractions of hydrogen and helium in the mixture, c_H and c_{He}. As in [1, 2], the region of the phase diagram with an anomalous behavior of isotherms is studied by moving along the isotherm with a small step in the density. As was mentioned above, the isotherms of noble gas plasmas have no singularities because, in this case, there is no molecular components in the plasma. Hence, it is convenient to begin calculations for a helium plasma and, then, to increase the hydrogen fraction in the mixture. The results of calculations of the plasma composition along each preceding isotherm can be used as an initial approximation when calculating the next one. The main parameter distinguishing one curve from another is the hydrogen or helium mole fraction in the mixture ($c_H + c_{He} = 100\%$).
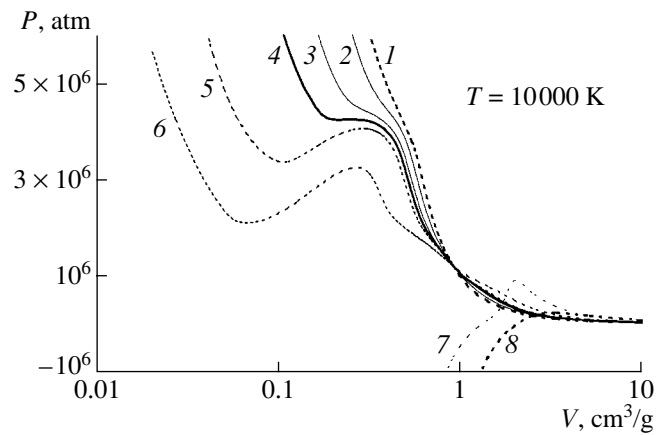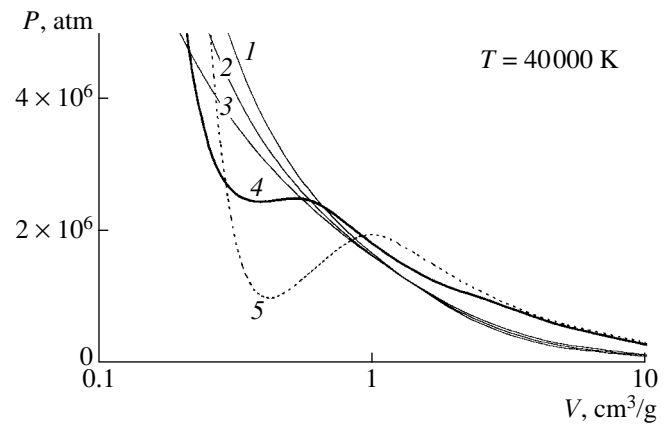

Fig. 1. Isotherm $T = 10^4$ K for a hydrogen–helium plasma. The mole fraction of the components in the mixture (H : He, %): (*1*) pure helium, (*2*) 10 : 90, (*3*) 20 : 80, (*4*) 25 : 75, (*5*) 30 : 70, (*6*) 50 : 50, (*7*) 90 : 10, and (*8*) pure hydrogen.

Figure 1 shows the isotherm $T = 10^4$ K of the hydrogen–helium mixture at different values of c_H and c_{He}. The isotherm of pure helium is the monotonic curve *1*. As the hydrogen mole fraction in the mixture increases, the behavior of the isotherm gradually changes (curves *2*, *3*) and a distinct inflection point appears at $c_H = 25\%$ (curve *4*). This point corresponds to a mass density of ≈ 4 g/cm^3 and a pressure of ≈ 4.25 Mbar. At a temperature of $T = 10^4$ K, the molar concentrations (25% H and 75% He) in curve *4* can be considered to be critical for the phase transition studied in [1, 2] in pure hydrogen. As the hydrogen mole fraction increases further, a characteristic van der Waals loop appears (curves *5*, *6*). Then, this loop degenerates into instability (curves *7*, *8*), which means that a stable solution for the dense phase is absent. Hence, according to calculations by the chemical model, the dissociative phase transition at $T = 10^4$ K is suppressed when the helium concentration in the mixture is higher than $c_{He} = 75\%$. Similar dependences for the isotherms $T = 3 \times 10^4$ K and 4×10^4 K are shown in Figs. 2 and 3. It is seen that, as the plasma temperature increases, the critical helium concentration required for suppressing the phase transition decreases rapidly (from 56% for $T = 3 \times 10^4$ K to 10% for 4×10^4 K). The critical temperature for the dissociative transition in pure hydrogen calculated by the chemical model is about 5×10^4 K [1, 2].
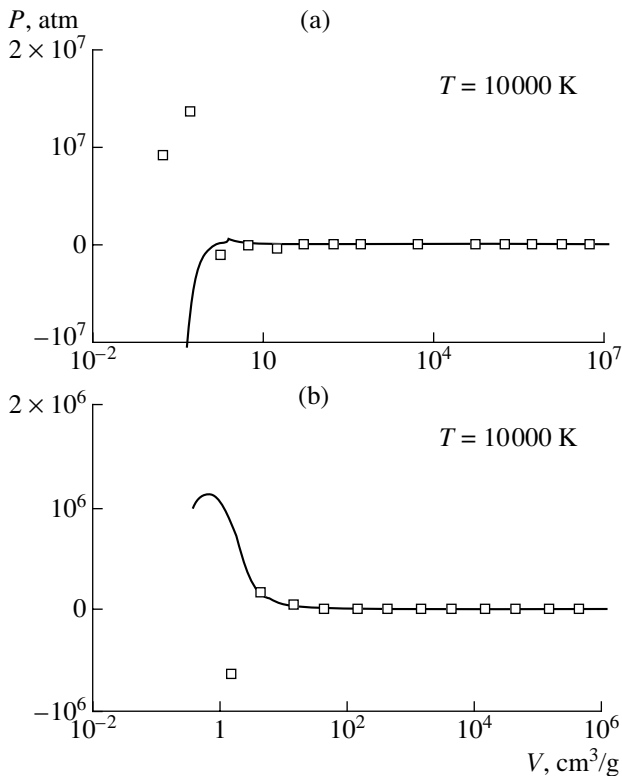
Now, we compare the results of calculations by the chemical model with the data from quantum-mechanical Monte Carlo calculations. An analysis of the diagrams shows that, over a wide range of temperatures for different helium concentrations in the range of low and moderate pressures, the results obtained with these two methods almost coincide (see Figs. 4–9). This agreement means that the quantum Monte Carlo method not only provides the reliable values of thermodynamic quantities for the specified ensemble of 100 nuclei, but also allows one to qualitatively trace the plasma com-
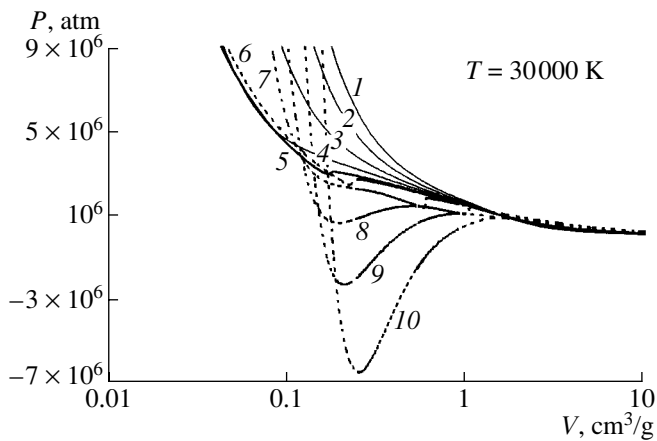
Fig. 2. Isotherm $T = 3 \times 10^4$ K for a hydrogen–helium plasma. The mole fraction of the components in the mixture (H : He, %): (*1*) pure helium, (*2*) 10 : 90, (*3*) 20 : 80, (*4*) 30 : 70, (*5*) 44 : 56, (*6*) 50 : 50, (*7*) 70 : 30, (*8*) 80 : 20, (*9*) 90 : 10, and (*10*) pure hydrogen.

Fig. 3. Isotherm $T = 4 \times 10^4$ K for a hydrogen–helium plasma. The mole fraction of the components in the mixture (H : He, %): (*1*) pure helium, (*2*) 10 : 90, (*3*) 20 : 80, (*4*) 90 : 10, and (*5*) pure hydrogen.
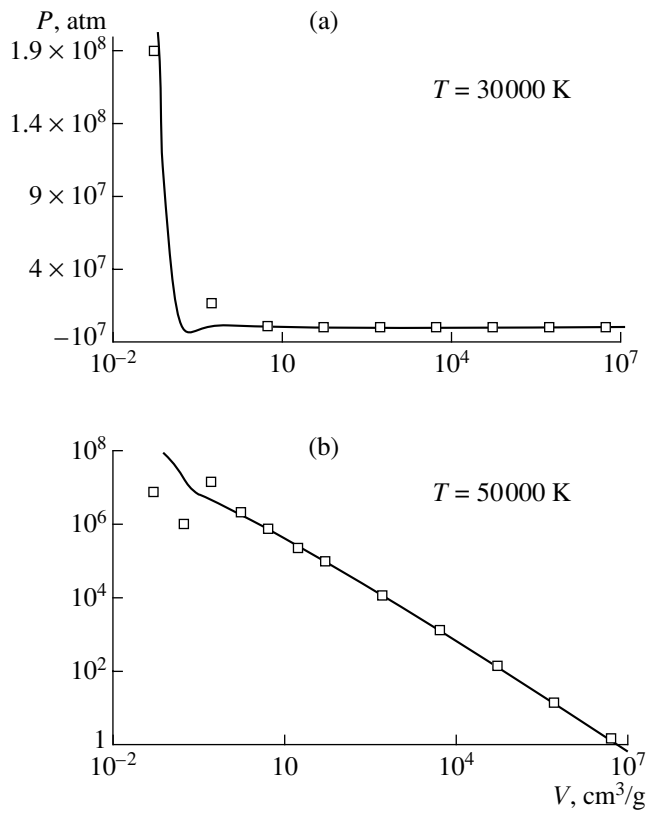
Fig. 4. Comparison of the results of calculations of the pressure for the isotherm $T = 10^4$ K by the chemical model (curves) and the Monte Carlo method (squares) for different helium mole fractions in the mixture: (a) 7 and (b) 33%.
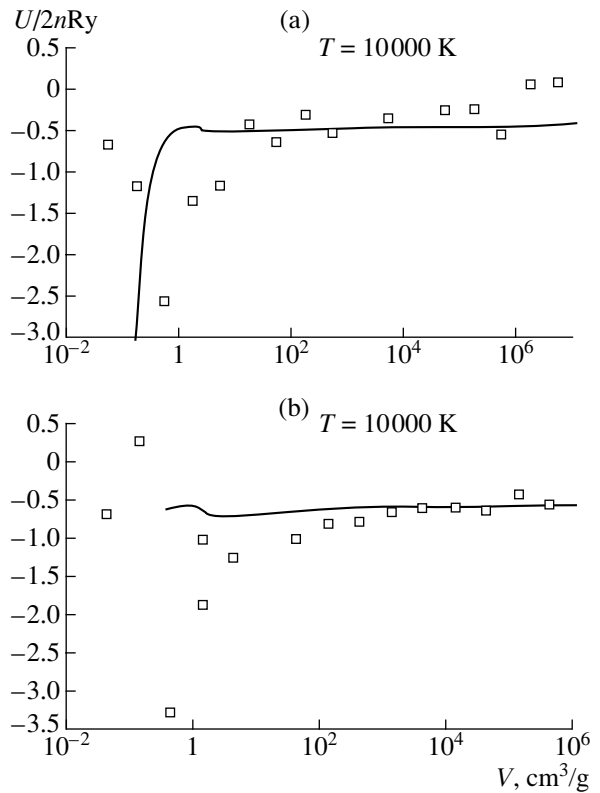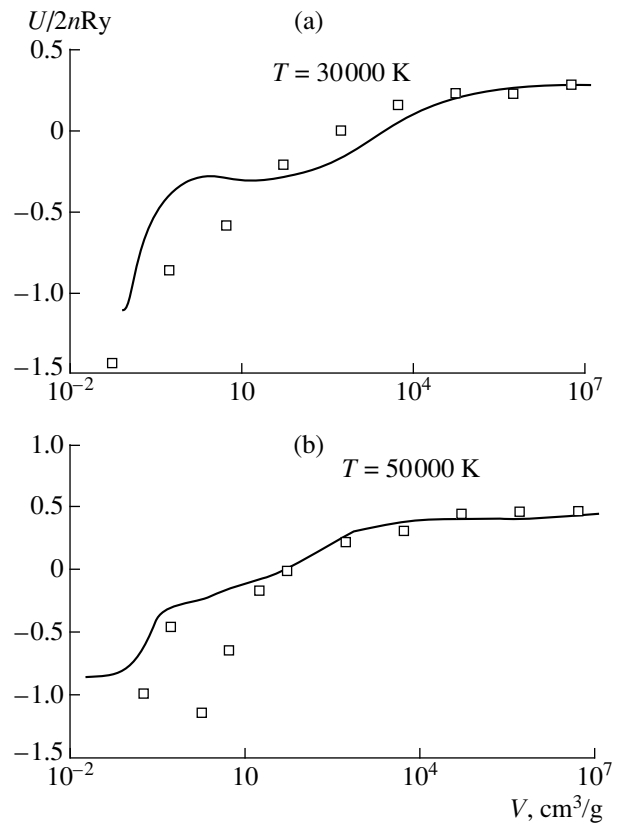
Fig. 5. Comparison of the results of calculations of the internal energy for the isotherm $T = 10^4$ K by the chemical model (curves) and the Monte Carlo method (squares) for different helium mole fractions in the mixture: (a) 7 and (b) 33%.

position. In other words, these calculations account (at least qualitatively) for the formation of bound states (atoms, molecules, etc.).

Moreover, for $T = 10^4$ K and a low helium concentration, both methods result in the appearance of the phase transition (Figs. 4, 5), whose positions in the

Fig. 6. Comparison of the results of calculations of the pressure for isotherms $T =$ (a) 3×10^4 and (b) 5×10^4 K by the chemical model (curves) and the Monte Carlo method (squares) for a helium mole fraction of 7%.


Fig. 7. Comparison of the results of calculations of the internal energy for isotherms $T =$ (a) 3×10^4 and (b) 5×10^4 K by the chemical model (curves) and the Monte Carlo method (squares) for a helium mole fraction of 7%.

phase diagrams calculated by the two methods are in qualitative agreement. However, there is a significant quantitative difference. According to the Monte Carlo calculations, the helium concentration at which the phase transition is suppressed turns out to be ~40%, whereas the calculations by the chemical model give 75%.

At higher temperatures of $T > 3 \times 10^4$ K, the quantum-mechanical Monte Carlo calculations (Figs. 6, 7) do not result in the appearance of anomalies in the phase diagram even at a low helium concentration, whereas the calculations by the chemical model show the existence of anomalies at least up to $T = 5 \times 10^4$ K. It should also be noted that the agreement between the calculations with respect to the internal energy is, of course, worse than that with respect to the pressure.

At $T > 5 \times 10^4$ K (the critical temperature of the dissociative phase transition obtained by the chemical model), the results of calculations of the plasma pressure obtained with both methods agree well up to 10^8 atm (Fig. 8). In this case, the plasma mass density is on the order of 10 g/cm^3. The density range in which the data on the internal energy obtained with both meth-
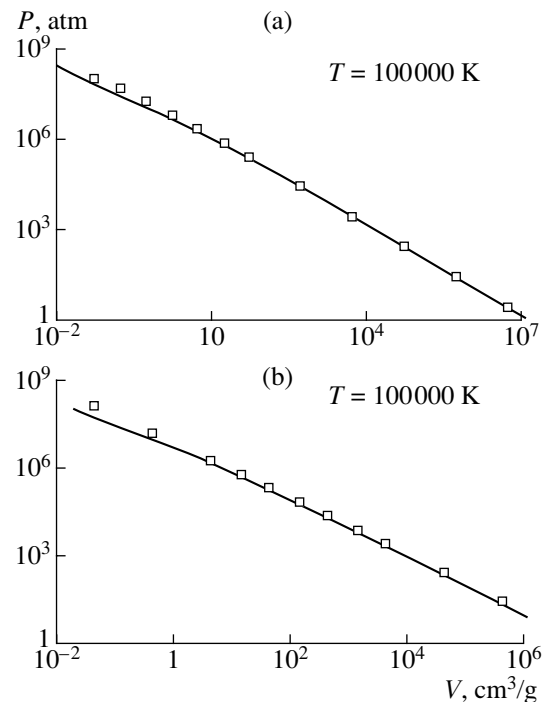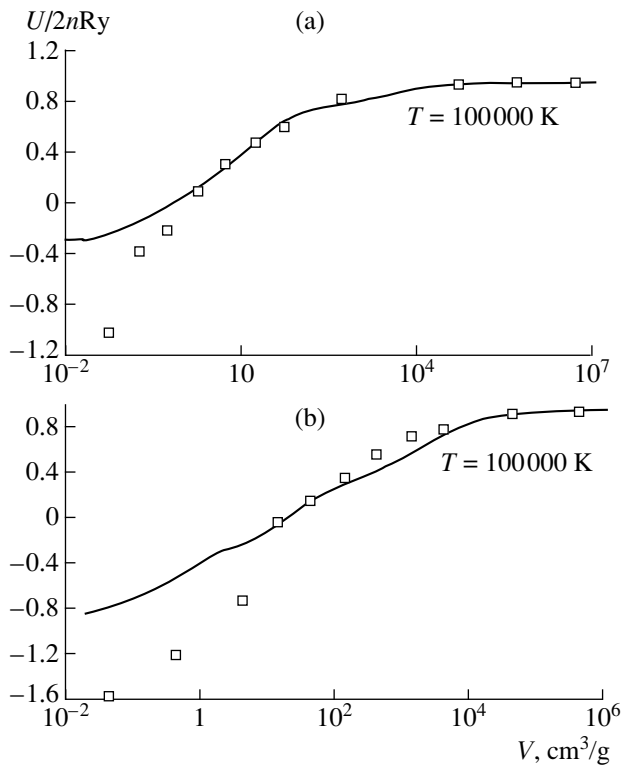

Fig. 8. Same as in Fig. 4 for isotherm $T = 10^5$ K.

Fig. 9. Same as in Fig. 5 for isotherm $T = 10^5$ K.

theless, an important result is that, in both cases, we observed the specific anomaly in the isotherms in the phase diagrams of hydrogen–helium plasma mixtures. The anomaly observed is of the same nature as that for pure hydrogen (the dissociative phase transition [1, 2]). The phase transition disappears gradually as the helium fraction in the mixture increases. Although both methods give different numerical values of the critical helium concentration above which the phase transition is suppressed, both of these methods indicate that the anomaly disappears as the He mole fraction in the mixture increases.

As a rule, noble gases are atomic. In our opinion, this fact confirms the dissociative nature of this phase transition [1, 2], because, according to our calculations, the phase transition in noble gases is absent due to the low concentration of molecular components.

ods are in good agreement expands significantly (Fig. 9).

3. CONCLUSION

A substantial quantitative difference between the results obtained by the Monte Carlo method and by using the chemical model at high pressures and low temperatures is related to the fact that the calculations were performed in the parameter range in which the chemical model is no longer applicable. Under these conditions, computations by the quantum Monte Carlo method are also characterized by poor stability. Never-

REFERENCES

1. M. Bonitz, I. A. Mulenko, E. N. Oleĭnikova, *et al.*, Fiz. Plazmy **27**, 1085 (2001) [Plasma Phys. Rep. **27**, 1025 (2001)].
2. I. A. Mulenko, E. N. Olejnikova, A. L. Khomkin, *et al.*, Phys. Lett. A **289**, 141 (2001).
3. V. S. Filinov, M. Bonitz, and V. E. Fortov, Pis'ma Zh. Éksp. Teor. Fiz. **72**, 361 (2000) [JETP Lett. **72**, 245 (2000)].
4. A. L. Khomkin, V. S. Vorob'ev, I. A. Mulenko, and E. N. Oleĭnikova, Fiz. Plazmy **27**, 369 (2001) [Plasma Phys. Rep. **27**, 347 (2001)].
5. I. A. Mulenko, E. N. Oleĭnikova, V. B. Soloveĭ, and A. L. Khomkin, Teplofiz. Vys. Temp. **39**, 13 (2001).
6. R. P. Feynman and A. R. Hibbs, *Quantum Mechanics and Path Integrals* (McGraw-Hill, New York, 1965).
7. I. A. Mulenko, V. B. Soloveĭ, A. L. Khomkin, and V. N. Tsurkin, Teplofiz. Vys. Temp. **37**, 518 (1999).
8. T. L. Hill, *Statistical Mechanics: Principles and Selected Applications* (McGraw-Hill, New York, 1956; Inostrannaya Literatura, Moscow, 1960).

Translated by N. F. Larionova

Study of the Linear Conversion of Lower Hybrid Waves in the FT-1 Tokamak by the Enhanced Time-of-Flight Scattering Technique

A. D. Gurchenko, E. Z. Gusakov, V. V. Korkin, M. M. Larionov, K. M. Novik, Yu. V. Petrov, A. Yu. Popov, V. L. Selenin, and A. Yu. Stepanov

Ioffe Physicotechnical Institute, Russian Academy of Sciences,
ul. Politekhnicheskaya 26, St. Petersburg, 194021 Russia

Abstract—The propagation of lower hybrid (LH) waves in a tokamak plasma in the presence of an LH resonance surface is studied experimentally with the use of a specially elaborated technique based on the backscattering of the probing microwave radiation in the upper hybrid resonance region. The technique provides resolution in the wave vectors of the scattering density fluctuations. The conditions are determined under which the LH wave propagates in accordance with the predictions of linear theory and is converted into the short-wavelength ion Bernstein mode. The parameter range is found in which the predictions of linear theory fail to hold and the nonlinear effects come into play during LH wave conversion. The radial wavelengths of the LH and ion Bernstein waves are determined. © 2002 MAIK "Nauka/Interperiodica".

1. INTRODUCTION

In the early 1970s, a method based on the linear conversion of slow waves in the lower hybrid resonance (LHR) region was proposed to heat the ion component in a tokamak plasma. This method was implemented in many devices with different geometric dimensions and plasma parameters over a wide range of heating wave frequencies (from 300 MHz to 2.5 GHz) [1]. In spite of numerous experimental studies, the role of the LHR in the absorption of slow waves was not clearly established and attempts to achieve efficient and reproducible ion heating were unsuccessful. Instead, these experiments revealed a complicated picture of the nonlinear interaction of lower hybrid (LH) waves with a plasma. To study this interaction, it was necessary to elaborate new sensitive methods for the local diagnostics of plasma oscillations in high-temperature tokamak plasmas.

The method of enhanced scattering (ES) of microwaves in the vicinity of the upper hybrid resonance (UHR) [2–4] is an efficient tool for studying short-wavelength density oscillations and waves in tokamak plasmas. This method, which has significantly progressed in the past decade [4–10], implies that a probing extraordinary wave is launched from the high-field side, whereas the observation is made of a wave scattered backward by low-frequency plasma density fluctuations near the UHR surface, whose position is given by the equality

$$\omega_i^2 = \omega_{ce}^2(x) + \omega_{pe}^2(x), \qquad (1)$$

where ω_i is the probing frequency, ω_{ce} is the electron cyclotron frequency, and ω_{pe} is the electron plasma frequency. As the hybrid resonance is approached, the radial wavenumber of the probing wave increases rapidly and becomes much higher than the wavenumber in vacuum $k_0 = \omega_i/c$. That is why the method turns out to be very sensitive to small-scale oscillations. The amplitudes of both the probing and backscattered waves increase as the wavenumber increases, which ensures high scattering efficiency and high spatial resolution of measurements. If the radial component of the wave vector q of fluctuations lies in the range

$$2k_0 \ll q \ll \rho_{ce}^{-1}, \qquad (2)$$

where ρ_{ce} is the electron Larmor radius, the location of the measurement region is determined by the UHR position. For shorter wavelength fluctuations, the position of the backscattering point, given by relation (1), can differ from the position of the UHR point. In the ES technique, one or two closely spaced antennas are used to launch the probing waves and to receive the scattered signals. Information about the spatial distribution of plasma fluctuations can be obtained by displacing the UHR layer, for which purpose either the probing frequency or the magnetic field is varied.

Since the wave vectors of the incident $\mathbf{k}_i(x)$ and scattered $\mathbf{k}_s(x)$ waves change significantly, the Bragg resonance condition for ES, which has the form

$$\mathbf{k}_i(x) - \mathbf{k}_s(x) = -\mathbf{q}, \qquad (3)$$

can be satisfied over a wide range of the wave vectors $\mathbf{q}$ of the scattering fluctuations. For this reason, the ES

signal is, in fact, integrated over the wave vectors of the plasma fluctuations. This circumstance reduces the amount of prior information required to perform the measurements and allows one to restrict the analysis to one-dimensional scattering, which is a significant advantage of the technique under discussion. At the same time, because of the above-mentioned integral character of this technique, the resolution in the wave vectors is poor and the data obtained with this method are, to a great extent, qualitative. Recently, some ways have been proposed to improve the resolution in wave vectors [5–8] by using the effect of decreasing the group velocities of the incident and scattered waves in the UHR region. It was shown theoretically [5, 6] that this effect can ensure a very long delay time of the ES signal, t_d. In the geometrical-optics approximation, this time is determined by the expression

$$t_d = 2 \int_{x_0}^{x_s(q)} dx/V_g, \tag{4}$$

where x_0 is the horn coordinate and V_g is the group velocity of the extraordinary wave. For fluctuations satisfying inequality (2), the delay time depends linearly on the radial component q of the wave vector of the scattering fluctuations:

$$t_d = 2q\omega_i \left| \frac{\partial \omega_{pe}^2}{\partial x} + \frac{\partial \omega_{ce}^2}{\partial x} \right|^{-1}. \tag{5}$$

This dependence was confirmed in several linear plasma devices [7–10], in which spontaneous and parametric ion-acoustic turbulence and the propagation of LH waves excited by external antennas were studied.

In this study, the time-of-flight ES diagnostics is used to investigate the propagation of LH waves in a tokamak plasma and the conversion of these waves into ion Bernstein waves. A brief description of the experiment in the FT-1 tokamak is given, and the experimental results are presented and discussed.

2. DESCRIPTION OF THE EXPERIMENT

The experiments were carried out in the FT-1 tokamak [11] with a major radius of $R = 62.5$ cm and a minor radius of $a = 15$ cm. The maximum toroidal magnetic field in the center of the chamber was $B(0) = 1$ T, the plasma current was $I_p = 30$ kA, the central electron density was $n_e(0) = (7–13) \times 10^{12}$ cm^{-3}, and the central electron temperature was $T_e(0) = 400$ eV. In the experiments, we used a set of conventional electromagnetic diagnostics and a one-channel interferometer. The density profile was determined before the experiments with the help of a four-channel interferometer. In some discharges, we monitored charge-exchange neutral fluxes, soft X-ray emission, and the emission at the first harmonic of the electron cyclotron resonance (ECR). LH waves at a frequency of 360 MHz were excited with the

help of a loop antenna positioned in the limiter shadow at the low-field side of the tokamak. The magnetron power was up to 50 kW. In what follows, the section in which the LH-wave antenna was installed is called the LH section. At the high-field side, opposite the LH-wave antenna, two horn antennas for launching and receiving extraordinary microwaves were positioned in the equatorial plane. The angle corresponding to a level of 3 dB in the antenna directional patterns was ±20° about the equatorial plane. The fraction of the ordinary mode in the total antenna power was less than 2%. Three additional horn antennas were installed in the section spaced at 180° from the LH-section in the toroidal direction. Two of these antennas were positioned in the equatorial plane at the high-field side and served as an emitter and a receiver of extraordinary waves. The third antenna was installed in the same section at the low-field side and was used in this experiment for calibration measurements, in which the probing wave was launched in the absence of a plasma. For these antennas, the angle corresponding to a level of 3 dB in the directional pattern was ±8° and the ordinary mode fraction was less than 1%. Below, the poloidal section in which these antennas were installed will be called the ES section.

The estimate by formula (4) shows that, under the FT-1 experimental conditions, the delay time of the ES signal is fairly long and can exceed 10 ns. In principle, such delay times could be measured with a stroboscopic technique based on the amplitude modulation [7–10]. This technique, which was tested in previous experiments, makes it possible to estimate the wave-number spectrum of oscillations. Unfortunately, because of the low power of the scattered signal, which is only one order of magnitude higher than the power of electron cyclotron emission from the plasma, the loss of the scattered signal that is inherent in this technique cannot be tolerated. In our experiment, we used a technique based on the harmonic amplitude modulation of the incident wave with the subsequent analysis of the phase delay in the modulated scattered power. This technique allowed us to determine the average wave-number of fluctuations within the frequency range under study.

Figure 1 shows a schematic diagram of the measurements. A probing power of 20 mW at a frequency of 28.1 GHz from a standard signal generator G_0 was modulated in the amplitude with a 10-MHz modulation generator MG with the help of a p–i–n diode M and was gained to a level of 50 W at the output of an amplifier A_0 based on the travelling-wave tube with a 1-GHz amplification band. To suppress the strays from the magnetron, a filter F_1 was installed at the output of the travelling-wave tube; the filter attenuation exceeded 15 dB when tuning away from the probing frequency by ±360 MHz. A power of 20 W transmitted into the probing horn was launched into the plasma as an extraordinary wave. The scattered radiation was ana-
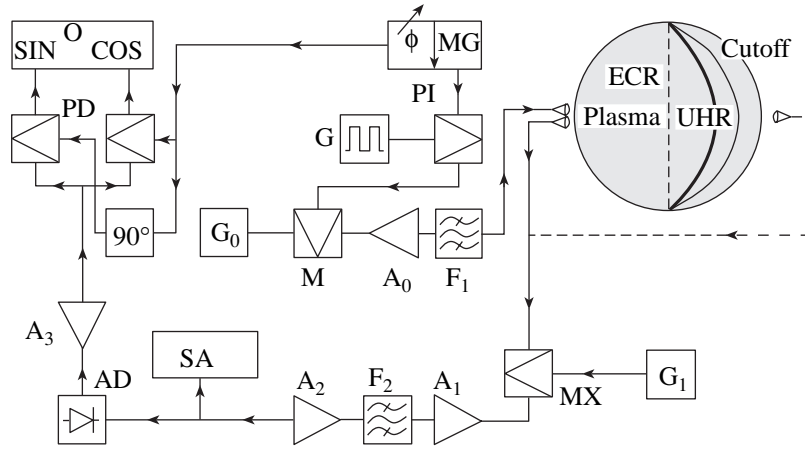
Fig. 1. Schematic of the diagnostics: (G_0) probing generator, (M) modulator, (A_0) microwave amplifier based on the travelling-wave tube, (F_1) microwave filter, (MG) modulation generator, (PI) phase inverter, (G) square-wave generator, (G_1) heterodyne, (MX) mixer, (A_1, A_2, A_3) intermediate-frequency amplifiers, (F_2) filter, (SA) spectrum analyzer, (AD) amplitude detector, (PD) phase detector with two quadrature channels, and (O) oscillograph.

lyzed with the help of a superheterodyne receiver tuned to a signal shifted by 360 MHz from the probing frequency toward the higher (blue satellite) or lower (red satellite) frequencies by extracting the intermediate frequency in a mixer MX with the use of a generator G_1 as a heterodyne. After the 20-dB amplification (A_1) of the modulated signal at an intermediate frequency of 920 MHz, its spectrum and phase delay relative to the modulation of the incident power were studied in the 60-MHz band. This was made possible by using a filter F_2, which produced the 3-dB attenuation when tuning away from the frequency 920 MHz by ±30 MHz and the 10-dB attenuation when turning away by ±40 MHz. After the filter F_2, the signal was additionally amplified by 40 dB with the help of an amplifier A_2. To obtain the spectrum of the scattered signal, we used a spectrum analyzer SA with an operating time of 2 ms. Before the phase measurements, we performed an additional amplitude detection of the received signal with the help of an amplitude detector AD. After the detection and amplification by 30 dB (an amplifier A_3), the signal was fed to one of the inputs of a phase detector PD, based on the quadrature circuit. 10-MHz oscillations from the second output of the generator MG were fed as a reference signal to the other input of the phase detector. From the outputs of the phase detector PD, the signals were fed to an oscillograph O and amplitude-to-digital converter, after which they were stored in a computer. To simplify the interpretation of the phase measurements, 10-MHz modulation oscillations were additionally inverted with the help of a phase inverter PI, in which their phase was changed by 180° at a repetition rate of 1 kHz by using a square-wave generator G. As a consequence, the PD output signals were 1-kHz oscillations. The phase-tunable 10-MHz output of the generator MG was used to calibrate the circuit. For this

purpose, the amplitude of the signal from the PD output in one of the channels was set at zero. By convention, this channel was referred to as the sinusoidal one, whereas the second channel was referred to as the cosinusoidal one. The phase shift φ was determined from the phase curve

$$\varphi = \arctan(S/C), \qquad (6)$$

where S and C are the amplitudes of 1-kHz oscillations in the sinusoidal and cosinusoidal channels, respectively. The scattered-signal power P_S in the 60-MHz band was determined from the formula

$$P_S = \sqrt{S^2 + C^2}, \qquad (7)$$

and the signal delay time t_d (in s) was calculated as

$$t_d = \frac{1}{2\pi \times 10^7} \arctan(S/C). \qquad (8)$$

To measure the signal spectrum, we interrupted the amplitude modulation of the probing radiation for 2 ms (this is seen in the phase curves in Fig. 2). To compensate the phase shift due to the propagation of the scattered and probing waves through the transmission lines, the system was calibrated in the absence of a plasma. In the ES section, the probing wave was launched from the horn situated at the high-field side into the horn situated at the opposite side. For calibration, we used signals at the probing frequency (Fig. 2a) and the frequency shifted by 360 MHz from the probing frequency with the help of an imitator. The phase between two outputs of the 10-MHz generator was tuned such that the signal in the sinusoidal channel became zero (Fig. 2a). In the LH section, the calibration was performed using a signal at the probing frequency that was reflected from the chamber wall. In the presence of the plasma, the ratio
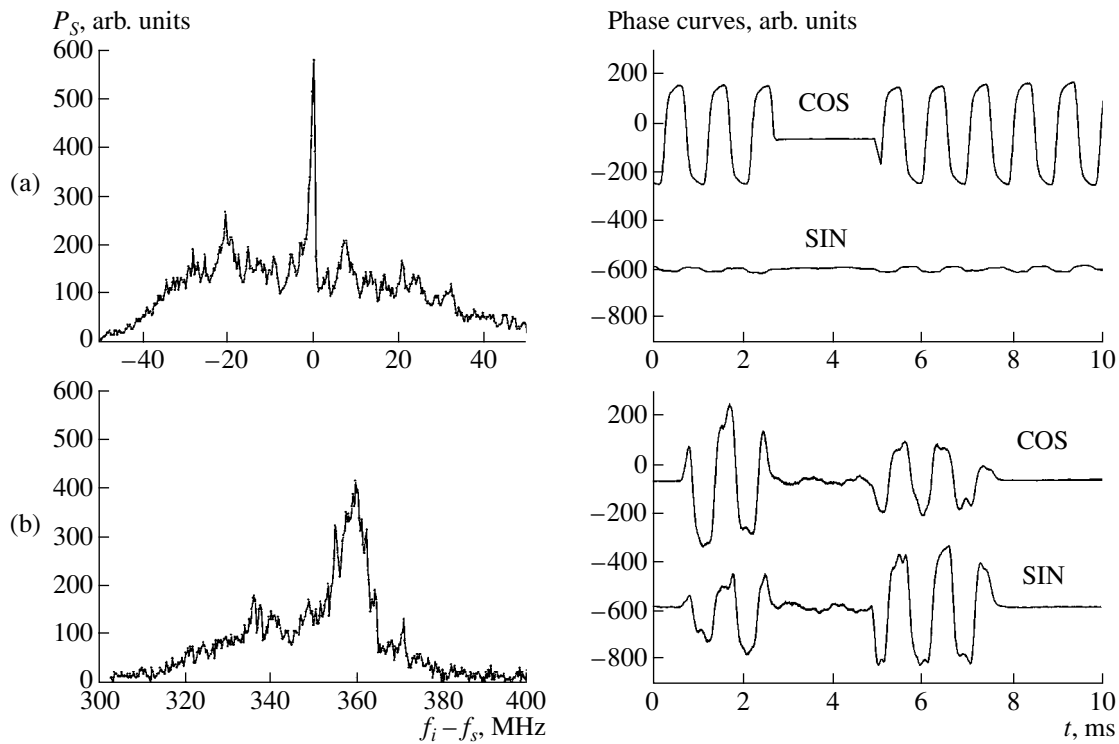
Fig. 2. Frequency spectra and phase curves of the signal measured during the calibration of the system at the probing frequency (a) without a plasma and (b) by scattering in the plasma at the magnetron frequency.

between the amplitudes in the sinusoidal and cosinusoidal channels changed (Fig. 2b) and the LH-wave spectrum was substantially broader than the magnetron spectrum.

3. DISCUSSION OF THE EXPERIMENTAL RESULTS

In the experiments, we studied how the frequency spectrum, the power P_S, and the delay time t_d of the ES signal within the 60-MHz frequency band depended on the toroidal magnetic field, which was varied from shot to shot. These dependences were constructed for both the red and blue satellites corresponding to the propagation of LH waves into and out of the plasma, respectively. The delay time t_d derived from the values of the signals in the quadrature channels was recalculated by formula (5) to the corresponding value of the radial wavenumber q. If the obtained values turned out to be close to the reciprocal of the electron Larmor radius, they were refined with the exact expression (4). The dependences on the magnetic field were represented in terms of the electron density in the UHR point, n_{UH}, calculated from relationship (1), taking into account current values of the density and field in the discharge. It should be noted that the local density value at the scattering point $x_s(q)$ given by relation (3) coincided with n_{UH} only for fluctuations with wavenumbers satisfying inequality (2). In the figures, we present the val-

ues of the power and delay time at the beginning (circles) and end (triangles) of the microwave pulse. The measurements for the red and blue satellites are shown by open and closed symbols, respectively. The frequency spectra were constructed as functions of the average value of n_{UH} measured over a 2-ms interval in the middle of the microwave pulse.

Figure 3 shows the results of the measurements of q and P_S in the ES section in the regime with a low density ($n_e(0) = 7 \times 10^{12}$ cm^{-3} before the microwave pulse) and low LH power ($P_{LH} = 22$ kW). As can be seen in Fig. 3a, the values of the radial wavenumber of LH oscillations for both spectral satellites increase as n_{UH} increases, i.e., as the UHR resonance is shifted deeper into the plasma. For $n_{UH} = 3 \times 10^{12}$ cm^{-3}, the wavenumbers reach a maximum value of $q = 400$ cm^{-1} and, then, arrive at a level of $q = 200$–150 cm^{-1} at $n_{UH} = (3.5$–$5.5) \times 10^{12}$ cm^{-3}. At lower densities in the UHR region ($n_{UH} < 3 \times 10^{12}$ cm^{-3}), the ES powers P_S for the red and blue components of the spectrum (Fig. 3b) are comparable to each other. However, at higher densities in the UHR region, the red component is dominant and the power of the UH wave propagating into the plasma is almost three times as large as that of the wave propagating toward the plasma boundary. In the dependence of P_S on n_{UH} for the red satellite, we can see a peak in the region $n_{UH} = 3.5 \times 10^{12}$ cm^{-3}, where the wavenumbers fall down to a level of $q = 200$ cm^{-1}. Under the same
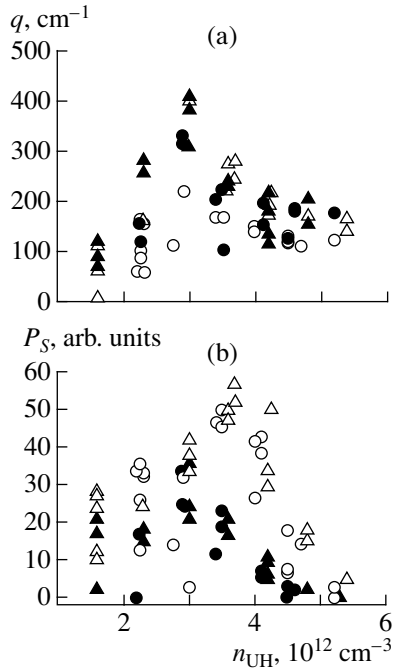
Fig. 3. (a) Radial wavenumbers and (b) the scattered-signal power in the ES section of the tokamak for a discharge with $n_e(0) = 7 \times 10^{12}$ cm^{-3} and $P_{LH} = 22$ kW.

conditions, the 3-MHz wide UH line shifted by 360 MHz toward lower frequencies from the probing frequency is dominant in the spectrum (Fig. 4a); however, its intensity decreases at lower values of n_{UH}. At $n_{UH} < 3 \times 10^{12}$ cm^{-3}, the intensity of this line becomes comparable with that of the LH line shifted by 360 MHz toward higher frequencies (Fig. 4b) and the width of the scattering spectrum increases substantially. The large wavenumbers observed in the experiment cannot be assigned to LH waves, because they are possible only for ion Bernstein waves ($q = 400$ cm^{-1}) or the waves in the linear conversion regions ($q = 200$–150 cm^{-1}). The observations described above may be explained on the assumption that, for $n_{UH} > 3 \times 10^{12}$ cm^{-3} ($B < 1.0$ T), the scattering point is located in the region of the main flux of the wave energy reaching the LHR surface. To confirm this assumption, we performed a one-dimensional analysis of the dispersion curves of the LH, ion Bernstein, and probing extraordinary waves. These dependences are presented in Fig. 5 by the dotted lines for the LH (curves 2) and ion Bernstein (curves 3) waves with $N_\parallel = 7$ and by the solid line for the difference between the radial components of the wave vectors of the incident and scattered waves, $k_i - k_s$ (curves 1). It is seen that, for the density $n_{UH} = 3.5 \times 10^{12}$ cm^{-3} ($B = 0.95$ T),
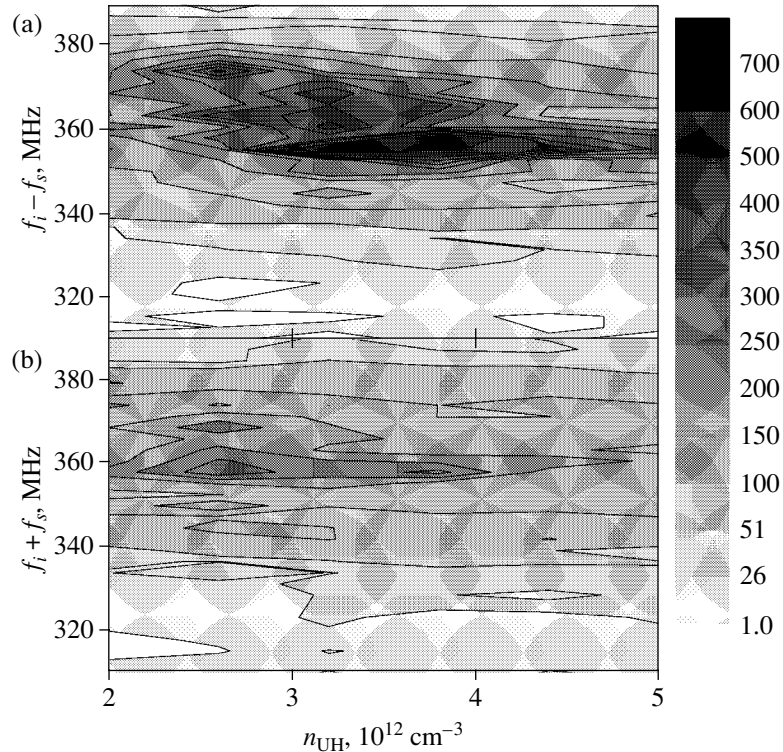
Fig. 4. Spectra of the scattered signal for the (a) red and (b) blue satellites as functions of n_{UH} in the ES section of the tokamak for a discharge with $n_e(0) = 7 \times 10^{12}$ cm^{-3} and $P_{LH} = 22$ kW.

q, cm^{-1}
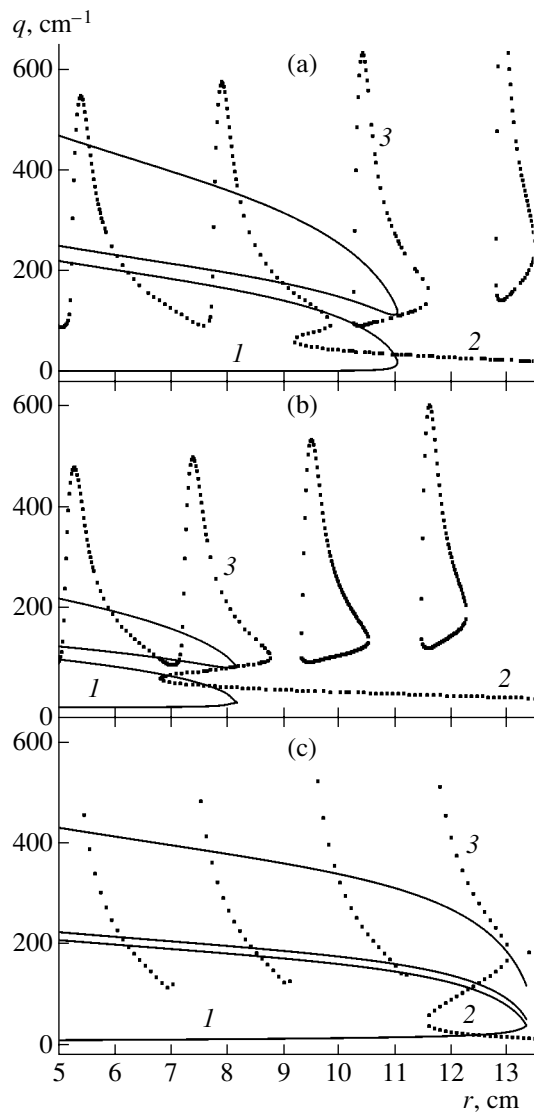
Fig. 5. (*1*) The difference between the radial components of the wave vectors of the incident and scattered waves and the dispersion curves of (*2*) LH and (*3*) ion Bernstein waves for: (a) $n_e(0) = 7 \times 10^{12}$ cm^{-3} and $B = 0.95$ T, (b) $n_e(0) = 7 \times 10^{12}$ cm^{-3} and $B = 0.85$ T, and (c) $n_e(0) = 1.7 \times 10^{13}$ cm^{-3} and $B = 0.85$ T.

the Bragg resonance condition (3) for the radial components of the wave vectors, $k_i - k_s = q$, is satisfied for $q = 130$, 180, and 370 cm^{-1} on the ion Bernstein branch (Fig. 5a). For a higher density in the UHR point, $n_{UH} = 4.7 \times 10^{12}$ cm^{-3} (or a lower magnetic field of $B = 0.85$ T), the Bragg resonance conditions can be satisfied only in the LHR region and on the "warm" branch; in this case, we have $q \simeq 100$ cm^{-1} (Fig. 5b). For a higher central density, $n_e(0) = 1.7 \times 10^{13}$ cm^{-3}, and a magnetic field as low as $B = 0.85$ T, the Bragg resonance condition can be satisfied not only for the LH wave, but also on the

warm branch at $q = 150$ and 200 cm^{-1} (Fig. 5c). Strictly speaking, the analysis performed is valid only when the wave propagates in the radial direction, which, for LH waves, takes place only after linear conversion. Hence, although both values of the wavenumbers are close to those in Fig. 3a, it necessary to verify that the linear conversion of the LH wave at $B = 0.95$ T can occur in the ES section. The LH ray trajectories in the (φ, θ) plane (where φ and θ are the toroidal and poloidal angles, respectively) calculated for different magnetic fields (Fig. 6) confirm that this situation is quite possible. As is seen, the lengths of the ray trajectories starting in the LH section with the initial value of the refractive index $N_\parallel = 7$ are very short (Fig. 6a). These trajectories make only a half toroidal revolution and end when the wave is absorbed in the LHR region in the ES section. The segment of the ray trajectory representing the warm LH mode propagating outward and the Bernstein harmonic traveling into the plasma column is oriented radially. This segment is projected into a point on the (φ, θ) plane. When calculating the ray trajectories at the edge of the discharge, we assumed that, besides protons, the plasma also contains completely ionized nitrogen ions. The value of the effective charge number in this case was taken to be equal to $Z_{eff} = 1.8$. This value is close to the estimate given in [12] for a low-density FT-1 discharge, although it is lower than the values typical of this tokamak. Note that the waves starting with lower values of $N_\parallel$ have longer trajectories which can finish even beyond the ES section. At lower values of the magnetic field, when the LHR region is shifted deeper into the plasma, these trajectories make a complete revolution and reach the LH section.

It should be noted that, according to the ray-tracing calculations, the ES signal at strong magnetic fields and low values of n_{UH} was observed well apart from the resonance cone of LH waves emitted by the antenna. This signal is probably produced via ES by the LH waves that have changed their propagation direction substantially after scattering repeatedly by low-frequency turbulent density fluctuations. This hypothesis is indirectly confirmed by the broad scattering spectra and the fact that the red and blue satellites have nearly the same amplitudes.

Figure 7 shows the results of the measurements of q and P_S in the LH section under the same operating conditions. The values of the wavenumbers observed in this section are somewhat lower than those in the ES section; however, their dependences on n_{UH} (Fig. 7a) are similar to those shown in Fig. 3a for the ES section. At the same time, the behavior of the power of the scattered signal turned out to be different. The P_S value increases as the UHR region approaches the LH antenna, is minimum at $n_{UH} = 3 \times 10^{12}$ cm^{-3}, and then increases monotonically as n_{UH} increases to the maximum value attainable in the experiment. Outside the ES section, the ES signal powers for the red and blue satellites were almost the same everywhere, except for the

narrow region near the LH antenna, where the red satellite was higher than the blue one by 30–50%. Figure 8 shows the frequency spectra of the ES signal for the LH section. In the red component of the spectrum (Fig. 8a), the LH line at a frequency of 360 MHz does not show up against the background of many other lines observed over a certain range of n_{UH} (e.g., of the radial coordinate). In the blue component (Fig. 8b), the 360-MHz LH line is dominant in the spectrum for $n_{UH} > 2.5 \times 10^{12}$ cm^{-3}. As a whole, this line is noticeably broader (up to 10 MHz in the half-width). At $n_{UH} > 4.5 \times 10^{12}$ cm^{-3}, the amplitude of the red satellite is lower than that of the blue satellite.

The described features of the ES signal in the LH section can be explained qualitatively based on the ray-tracing analysis. First of all, the increase in the signal in the vicinity of the LH antenna may be attributed to the scattering by the intense LH wave just detached from the antenna. This is also supported by the fact that, at the plasma edge, the relatively low q value can be assigned immediately to the LH wave. The increase in the signal at low magnetic fields and, accordingly, high values of n_{UH}, are explained as follows. In this case, the LHR occurs deeper in the plasma and, in the LH section, the possibility exists of the linear conversion of waves with low longitudinal velocities ($3 < N_\parallel < 5$), which appear to be dominant in the spectrum excited by the antenna. At high magnetic fields, these waves are converted before they make a complete toroidal revolution, as is shown in Fig. 6a for a wave with $N_\parallel = 7$. In these measurements, the higher wavenumbers were observed, which may be explained by the displacement of the UHR region toward the plasma edge and, as a consequence, the higher wavenumbers of the incident and scattered waves in the this region (Fig. 5c). Note that, as in the case of Fig. 3, the scattering spectra are observed far from the calculated position of the resonance cone of the LH wave; the plausible explanation is that, in the plasma, there are LH waves that have been scattered repeatedly by turbulent density fluctuations and do not have any definite propagation direction.

Figure 9 presents the results of the measurements of q and P_S in the ES section for a discharge with the same value of the LH power $P_{LH} = 22$ kW, but with a higher density before the microwave pulse ($n_e(0) = 1.3 \times 10^{13}$ cm^{-3}). In this case, somewhat lower (in comparison with the ES section) radial wavenumbers may be explained by the lower values of the longitudinal refractive index for LH waves arriving at the LH section after a complete toroidal revolution. As the density in the UHR region increases, the wavenumbers (Fig. 9a) increase to a maximum level of $q = 550$ cm^{-1} at $n_{UH} = 3 \times 10^{12}$ cm^{-3} and, then, decrease to $q = 350$–250 cm^{-1} at $n_{UH} = (4.2$–5.5$) \times 10^{12}$ cm^{-3}. The ES signal power P_S for the red spectral component is higher than that for the blue one (Fig. 9b) by only 30–40% for $n_{UH} > 4.2 \times 10^{12}$ cm^{-3} ($B < 0.90$ T). For the lower values of n_{UH}, the
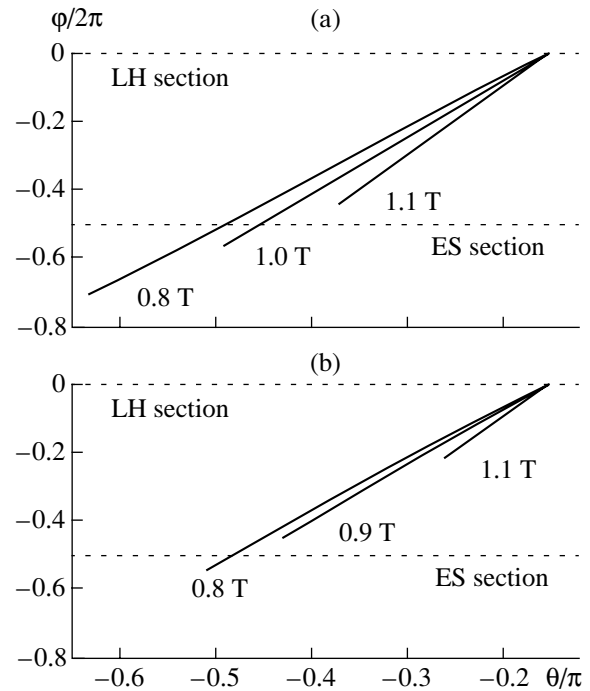
Fig. 6. Projections of LH ray trajectories starting in the LH section (a) for the initial value of the refractive index $N_\parallel = 7$ in a discharge with an initial (before the microwave pulse) central density of $n_e(0) = 7 \times 10^{12}$ cm^{-3} and (b) for $N_\parallel = 3$ in a discharge with $n_e(0) = 1.3 \times 10^{13}$ cm^{-3}.
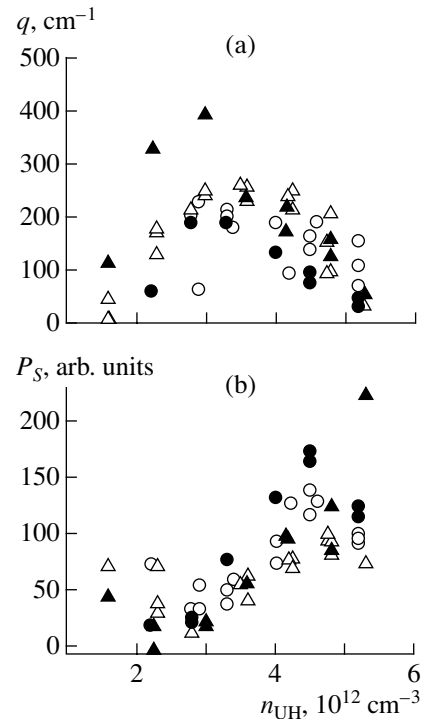
Fig. 7. (a) Radial wavenumbers and (b) the scattered-signal power in the LH section of the tokamak for a discharge with $n_e(0) = 7 \times 10^{12}$ cm^{-3} and $P_{LH} = 22$ kW.
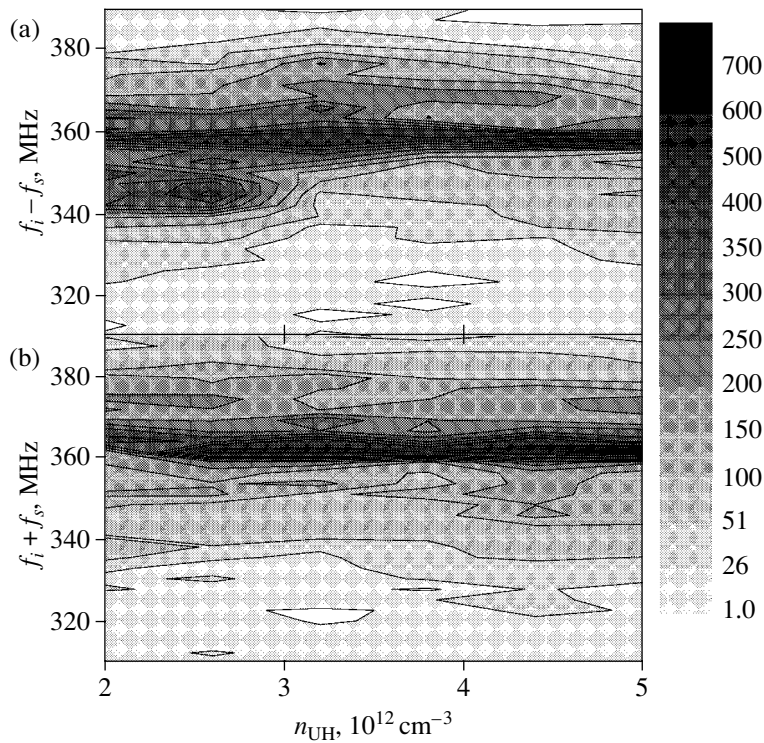
Fig. 8. Spectra of the scattered signal for the (a) red and (b) blue satellites as functions of n_{UH} in the LH section of the tokamak for a discharge with $n_e(0) = 7 \times 10^{12}$ cm^{-3} and $P_{LH} = 22$ kW.
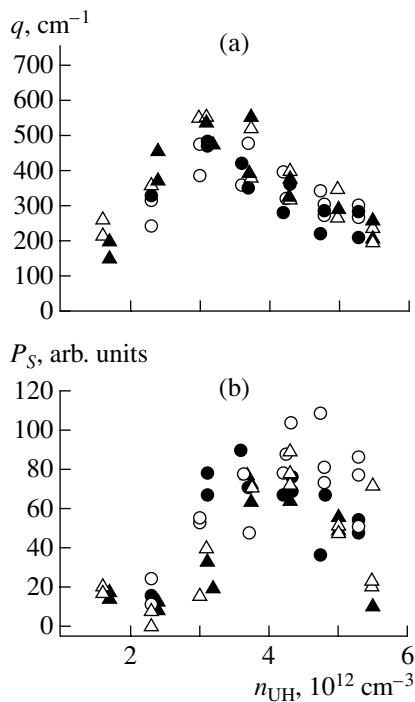
Fig. 9. (a) Radial wavenumbers and (b) the scattered-signal power in the ES section of the tokamak for a discharge with $n_e(0) = 1.3 \times 10^{13}$ cm^{-3} and $P_{LH} = 22$ kW.

difference is even smaller. In comparison with Fig. 3b, the maximum of P_S for the red spectral component is shifted to the range $n_{UH} = 4.5 \times 10^{12}$ cm^{-3} ($B = 0.87$ T), nearer to the maximum possible values of n_{UH}. The frequency spectra for the red and blue satellites are shown in Fig. 10. The 360-MHz line is well pronounced in these spectra. The amplitude of this line (which corresponds to the LH wave) in the red satellite (Fig. 10a) dominates over the blue satellite (Fig. 10b) only at $n_{UH} > 3.8 \times 10^{12}$ cm^{-3} ($B < 0.93$ T).

The ray-tracing analysis shows that, since, in this case, the LHR region is located nearer to the plasma edge, the waves corresponding to the high values of $N_\parallel$ are converted not reaching the ES section. This is true for $N_\parallel = 7$ at any magnetic field permitting the use of the ES diagnostics. Calculations performed for $N_\parallel = 3$ show (Fig. 6b) that the ray trajectories arrive at the ES section only at $B < 0.9$ T. These calculations confirm qualitatively that the spectrum can contain LH waves such that ES in the LHR region occurs in the ES section and also show that these waves are absent in the LH section. For the LH section, this conclusion is confirmed by the relevant measurements described below.

The n_{UH} dependences of the wavenumbers and the ES signal power measured in the LH section under the same operating conditions are similar to those in Fig. 7. The values of the wavenumbers at the plasma edge do

Fig. 10. Spectra of the scattered signal for the (a) red and (b) blue satellites as functions of n_{UH} in the ES section of the tokamak for a discharge with $n_e(0) = 1.3 \times 10^{13}$ cm^{-3} and $P_{LH} = 22$ kW.
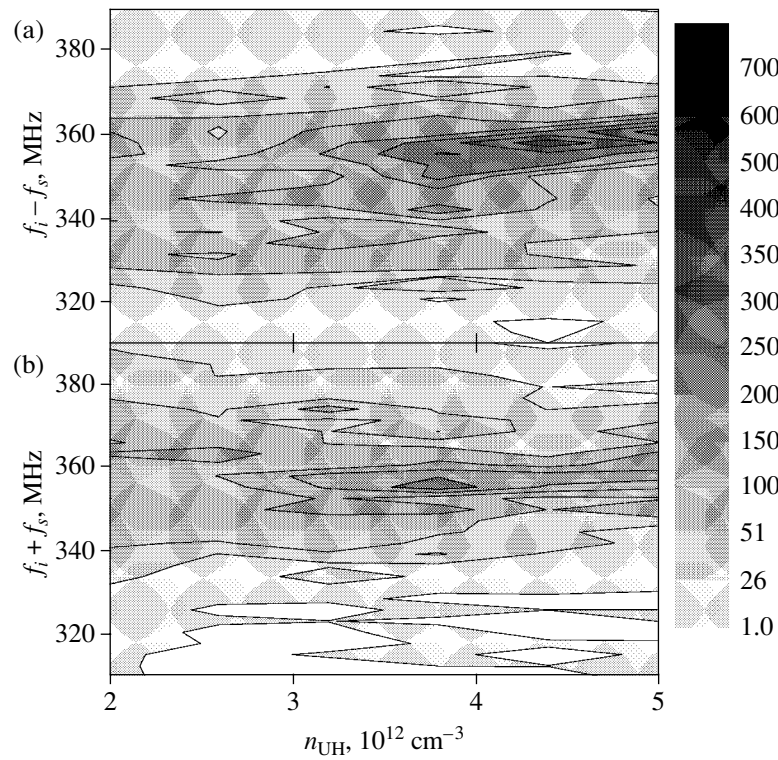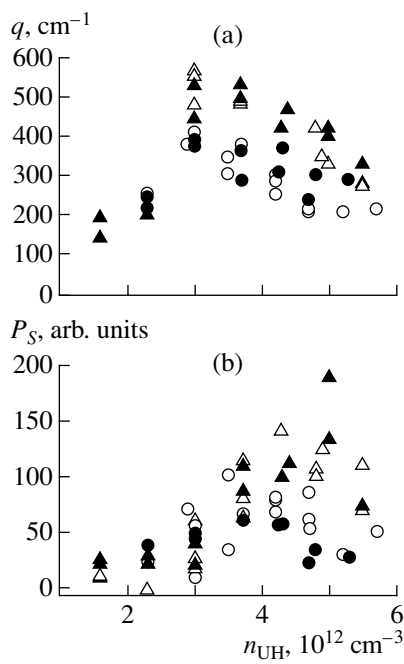

Fig. 11. (a) Radial wavenumbers and (b) the scattered-signal power in the ES section of the tokamak for a discharge with $n_e(0) = 7 \times 10^{12}$ cm^{-3} and $P_{LH} = 50$ kW.

Fig. 12. (a) Radial wavenumbers and (b) the scattered-signal power in the LH section of the tokamak for a discharge with $n_e(0) = 7 \times 10^{12}$ cm^{-3} and $P_{LH} = 50$ kW.
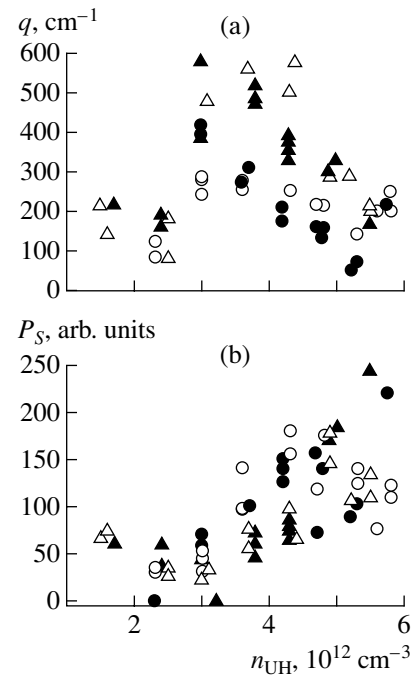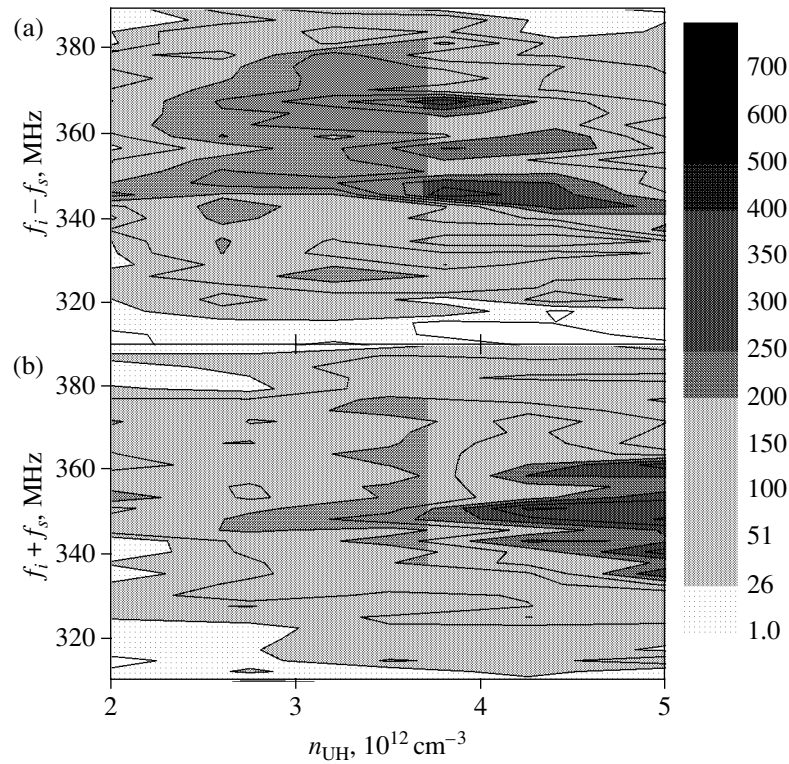
Fig. 13. Spectra of the scattered signal for the (a) red and (b) blue satellites as functions of n_{UH} in the ES section of the tokamak for a discharge with $n_e(0) = 1.3 \times 10^{13}$ cm^{-3} and $P_{LH} = 50$ kW.

not exceed $q = 150$ cm^{-1}. At $n_{UH} = 2.5 \times 10^{12}$ cm^{-3}, the wavenumbers increase sharply up to a level of $q = 550$ cm^{-1} and, then, decrease gradually to $q = 200$ cm^{-1} at $n_{UH} = 5.5 \times 10^{12}$ cm^{-3}. The level of the ES signal power and its dependence on n_{UH} are the same for the red and blue satellites. At $n_{UH} < 2.5 \times 10^{12}$ cm^{-3}, the signal increases as the antenna is approached. After passing a minimum at $n_{UH} = 2.5 \times 10^{12}$ cm^{-3}, the value of P_S increases monotonically as n_{UH} increases to its maximum value. The frequency spectra at the red and blue sides appear to have nearly the same amplitudes, and both spectra have no dominant lines at the pumping frequency 360 MHz.

Figure 11 shows the results of the measurements for the ES section in a discharge with a low density before the microwave pulse ($n_e(0) = 7 \times 10^{12}$ cm^{-3}), but with a high power ($P_{LH} = 50$ kW). As a whole, this experiment is characterized by the higher wavenumber values. After passing through a maximum value of $q = 500$ cm^{-1} at $n_{UH} = 3 \times 10^{12}$ cm^{-3}, the wavenumbers (see Fig. 11a) decrease to a level of $q = 270$ cm^{-1} more gradually than in Figs. 3b and 9b. The increase in the wavenumbers by the end of the microwave pulse seems to be analogous to the effect observed when comparing Figs. 3a and 9a and may be explained by the fact that the density increases to $n_e(0) = 1.2 \times 10^{13}$ cm^{-3} during the high-

power microwave pulse. The dependences of P_S on n_{UH} for both satellites are very similar. By the end of the microwave pulse, the amplitude of the signal increases in both spectral components. The frequency spectra, which are very similar for the red and blue satellites, become somewhat broader, whereas the 360-MHz line does not show up.

As the LH power increases, the wavenumbers observed in the LH section are also larger (Fig. 12a) than those in Fig. 7a. The wavenumbers of LH oscillations near the antenna are $q = 180$ cm^{-1}; they increase sharply to $q = 550$ cm^{-1} at $n_{UH} = 3 \times 10^{12}$ cm^{-3} and, then, decrease to $q = 200$ cm^{-1} at $n_{UH} = 5.5 \times 10^{12}$ cm^{-3}. As in the ES section, the wavenumbers increase by the end of the microwave pulse. The dependences of the ES signal power for both satellites (Fig. 12b) are close to each other. As in Fig. 7b, the value of P_S increases as the antenna is approached, is minimum at $n_{UH} = 2.5 \times 10^{12}$ cm^{-3}, and, then, increases monotonically as the density in the UHR region increases to its maximum value. In the frequency spectra, which were similar for both satellites, the 360-MHz line does not show up.

In a discharge with a high LH power ($P_{LH} = 50$ kW) and a high density before the microwave pulse ($n_e(0) = 1.3 \times 10^{13}$ cm^{-3}), the wavenumbers observed in the ES section turned out to be even higher and attained a value of $q = 760$ cm^{-1} and the wavenumbers in the LH section
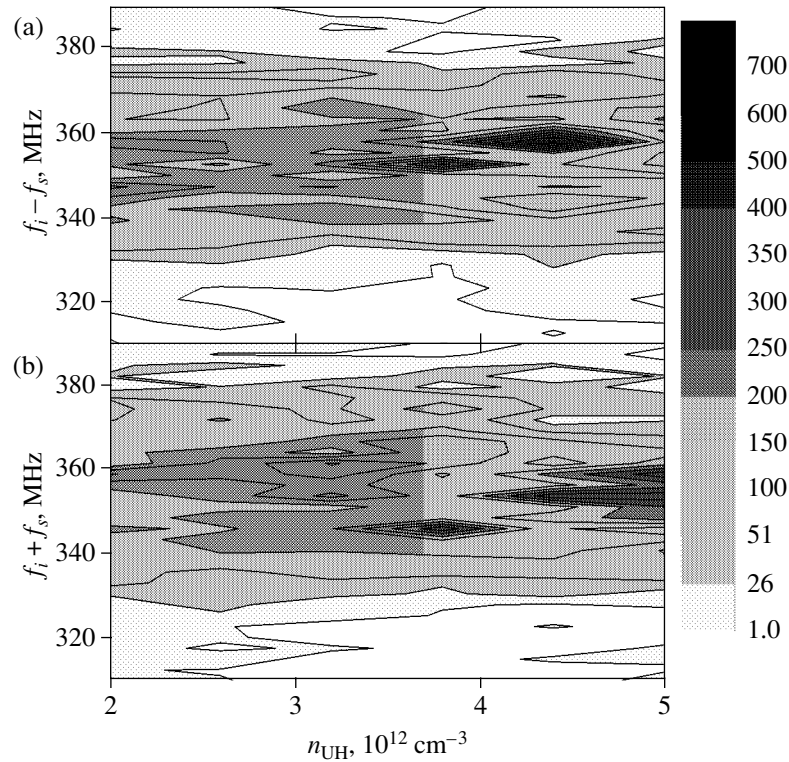
Fig. 14. Spectra of the scattered signal for the (a) red and (b) blue satellites as functions of n_{UH} in the LH section of the tokamak for a discharge with $n_e(0) = 1.3 \times 10^{13}$ cm^{-3} and $P_{LH} = 50$ kW.

attained $q = 730$ cm^{-1}. As in the LH section (Fig. 12a), the wavenumbers near the antenna were relatively low ($q = 180$ cm^{-1}), increased sharply as n_{UH} increased, and then decreased gradually to $q = 180$ cm^{-1} at $n_{UH} = 5.5 \times 10^{12}$ cm^{-3}. It should be noted that such a decrease was observed in both experimental sections at all combinations of the LH power and the electron density in the discharge. Most probably, this effect is due to the fact that the values of $k_i - k_s$ decrease in the plasma core (as is seen in Fig. 5b) and the high values of q can no longer be measured. The dependences of P_S on the n_{UH} were close in each section. The behavior of the ES signal power remains the same as in a discharge with a low density and a high microwave power (Figs. 11b, 12b). Figure 13 illustrates the frequency spectra for the ES section. It is seen that the spectra of the red (Fig. 13a) and blue (Fig. 13b) satellites differ insignificantly. These spectra contain a set of narrow lines, whose amplitudes are comparable with or exceed that of the 360-MHz line. The spectral lines are observed over a wide range of n_{UH} and their positions are spaced by a frequency close to the ion cyclotron frequency. Figure 14 shows the spectra measured in the ES section under the same operating conditions. There is no substantial difference between the satellites. The spectral lines with the highest amplitudes correspond to the frequencies different from 360 MHz. In contrast to regime with a

low density and low LH power (Fig. 8a), these lines are observed over a wider range of n_{UH} and, hence, exist in a larger spatial region. The features of the frequency spectra observed and the dependences of P_S and q on n_{UH} confirm to the fact that, as the microwave power and $n_e(0)$ increase, the picture of the wave propagation predicted by linear theory fails to hold and the role of nonlinear effects becomes important.

4. CONCLUSION

The study of the propagation of LH waves in a tokamak plasma by means of a specially elaborated time-of-flight diagnostics based on the backscattering of microwaves in the UHR region shows the efficiency of this method. The following features of the propagation and conversion of LH waves were observed (some of them being observed for the first time):

At the plasma edge, far from the calculated position of the resonance cone of the LH wave, its frequency spectrum turned out to be very broad (broader than 10 MHz) and no dominant direction of the energy propagation was detected. The radial wavelength of these oscillations, which are probably produced through the scattering by spontaneous density fluctuations, is 0.06–0.12 cm; this corresponds to very slow LH waves with $N_\parallel > 15$.

In a discharge with a low plasma density and a low microwave power, we observed the effects indicating that the propagation and transformation of LH waves occurred in accordance with linear theory. The frequency spectrum appeared to be narrow, and its width was no larger than 3 MHz. The wave propagated predominantly into the plasma. The radial wavelength, in this case, was equal to 0.03 cm, which corresponded to the region of the linear conversion of the LH wave into a warm mode. In addition, this was the first time in tokamak experiments that we could observe small-scale Bernstein waves at high harmonics of the ion cyclotron frequency; these waves were produced via liner conversion in the LHR region. The radial wavelength corresponding to these waves amounted to 0.010–0.015 cm.

At a higher microwave power and higher plasma density in the discharge, the picture of the LH wave propagation was somewhat different from that predicted by linear theory. The ES frequency spectra in the vicinity of the pumping frequency became broader, and the lines shifted by a frequency close to the ion cyclotron frequency appeared in these spectra. The values of the wavenumbers nearly doubled. For the short-wavelength component of the LH wave, which could be observed with the help of the ES diagnostics, no dominant direction of the energy flux was observed. All these observations provide evidence that, even at a relatively low input microwave power of 50 kW, the nonlinear effects play a significant role in the propagation and conversion of LH waves.

ACKNOWLEDGMENTS

REFERENCES

1. V. E. Golant and V. I. Fedorov, *RF Plasma Heating in Toroidal Devices* (Consultants Bureau, New York, 1989), p. 111.
2. A. D. Piliya, Zh. Tekh. Fiz. **36**, 2195 (1966) [Sov. Phys. Tech. Phys. **11**, 1639 (1966)].
3. I. Fidone, Phys. Fluids **16**, 1680 (1973).
4. K. M. Novik and A. D. Piliya, Plasma Phys. Controlled Fusion **35**, 357 (1994).
5. E. Z. Gusakov and A. D. Piliya, Pis'ma Zh. Tekh. Fiz. **18** (10), 63 (1992) [Sov. Tech. Phys. Lett. **18**, 325 (1992)].
6. B. Brusehaber, E. Z. Gusakov, M. Kramer, *et al.*, Plasma Phys. Controlled Fusion **36**, 997 (1994).
7. V. I. Arkhipenko, V. N. Budnikov, E. Z. Gusakov, *et al.*, in *Proceedings of the International Conference on Plasma Physics, Innsbruck, 1992*, ECA, Vol. 16C, Part II, p. 1203.
8. V. I. Arkhipenko, V. N. Budnikov, E. Z. Gusakov, *et al.*, Pis'ma Zh. Éksp. Teor. Fiz. **59**, 393 (1994) [JETP Lett. **59**, 420 (1994)].
9. V. I. Arkhipenko, B. Brusehaber, V. N. Budnikov, *et al.*, Plasma Phys. Controlled Fusion **37A**, 347 (1995).
10. B. Brusehaber and M. Kramer, Plasma Phys. Controlled Fusion **39**, 389 (1997).
11. I. P. Gladkovskiĭ, V. E. Golant, V. V. D'yachenko, *et al.*, Zh. Tekh. Fiz. **43**, 1632 (1973) [Sov. Phys. Tech. Phys. **18**, 1029 (1973)].
12. S. I. Lashkul, M. M. Larionov, L. S. Levin, and Yu. V. Petrov, Zh. Prikl. Spektrosk. **54**, 887 (1991).

Translated by N. F. Larionova

Boundary Conditions for the Electromagnetic Field in a Waveguide with a Thin-Walled Annular Plasma in the Context of Application to Plasma Microwave Electronics

M. V. Kuzelev

Institute of General Physics, Russian Academy of Sciences, ul. Vavilova 38, Moscow, 117942 Russia
Received December 14, 2001

Abstract—Effective boundary conditions for the electromagnetic field of the slow surface waves of a thin-walled annular plasma in a metal waveguide are derived and justified. With the boundary conditions obtained, there is no need to solve field equations in the plasma region of the waveguide, so that the dispersion properties of plasma waveguides can be investigated analytically for an arbitrary strength of the external magnetic field. Examples are given that show how to use the effective boundary conditions in order to describe surface waves with a normal and an anomalous dispersion. The boundary conditions are then employed to construct a theory of the radiative Cherenkov instabilities of a thin-walled annular electron beam in a waveguide with a thin-walled annular plasma. The single-particle and collective Cherenkov effects associated with low- and high-frequency surface waves in an arbitrary external magnetic field are studied analytically. The method of the effective boundary conditions is justified in the context of application to the problems of plasma relativistic microwave electronics. © 2002 MAIK "Nauka/Interperiodica".

INTRODUCTION

The theoretical investigation of electromagnetic waves in a circular waveguide in which the radial plasma profile is a piecewise constant function and the plasma is affected by an external magnetic field is a complicated and laborious task. The reason is that the electromagnetic field in the plasma region of the waveguide is represented as the superposition of four cylindrical functions with complex arguments, which results in an extremely complicated dispersion relation for the wave spectra [1–3]. Even in the simplest case of a waveguide completely filled with a plasma, a comprehensive examination of the spectra can be conducted only by numerical methods [4]. For a waveguide with an annular plasma (this case is very important from a practical standpoint), the dispersion relation is difficult not only to solve but even to write [5]. It is because of the complexity of description that the theory of the excitation of electromagnetic waves by an electron beam in a plasma-filled waveguide in an external magnetic field of finite strength is still far from being fully elaborated. However, the development of plasma relativistic microwave electronics created a demand for such a theory. Another important case is that of a waveguide with a thin-walled annular plasma. In this case, there is no need to solve the field equations in the plasma region and some types of plasma waves can be described analytically by incorporating the thin-walled annular plasma only into certain effective boundary conditions for the field equations. These boundary conditions and their application to plasma microwave electronics are the subject of the present paper.

1. FORMULATION OF THE PROBLEM AND BASIC RELATIONSHIPS

We consider a vacuum metal waveguide with a circular cross section of radius R. Let there be a thin annular plasma column with the mean radius r_p and the thickness $\Delta_p \ll r_p < R$ inside the waveguide. In other words, the plasma that fills the waveguide is treated as a tube with a thin wall. As was mentioned above, a complete mathematical description of such a plasma waveguide is extremely complicated because of the many different types of plasma and electromagnetic waves. Among these are surface plasma waves with phase velocities lower than the speed of light, two of which are especially interesting from the standpoint of plasma relativistic microwave electronics [6–8]. The objective of the present study is to construct a theory of these two waves by including the plasma in the equations for electromagnetic fields in vacuum through certain effective boundary conditions. This approach makes it possible to substantially simplify not only the theory of surface plasma waves but also the theory of their excitation by high-density relativistic electron beams. Below, the following three systems will be studied separately: a waveguide in an infinitely strong external longitudinal magnetic field, a waveguide in the absence of a magnetic field, and a waveguide in an

external longitudinal magnetic field of finite strength. Although the first two systems are particular cases of the third one, they are of considerable practical and methodological interest in their own right.

We introduce cylindrical coordinates $\{r, \varphi, z\}$ in such a way that the z-axis coincides with the symmetry axis of the waveguide. We restrict ourselves to considering azimuthally symmetric waves and represent the electromagnetic field components in the form $F(r)\exp(-i\omega t + ik_z z)$, where ω is the angular frequency, k_z is the longitudinal wavenumber, and $F(r)$ is the amplitude of any component of the field vectors. The field components in the vacuum regions of the waveguide (i.e., at $r < r_p - \Delta_p/2$ and $r_p + \Delta_p/2 < r < R$) are denoted by $F(r) \equiv F^{(0)}(r)$. Analogously, the field components in the plasma region ($r_p - \Delta_p/2 < r < r_p + \Delta_p/2$) are denoted by $F(r) \equiv F^{(p)}(r)$.

We assume that any electromagnetic field component $F(r)$ is continuous at the boundaries between different mediums. In the case at hand, these are the inner boundary $r_1 = r_p - \Delta_p/2$ of the plasma tube and its outer boundary $r_2 = r_p + \Delta_p/2$. The conditions for the field component to be continuous at the plasma boundaries have the form

$$F^{(0)}(r_1) = F^{(p)}(r_1), \quad F^{(p)}(r_2) = F^{(0)}(r_2). \quad (1.1)$$

We retain only the terms that are linear in the small annular plasma thickness Δ_p and use the expansions

$$F^{(p)}(r_{1,2}) = F^{(p)}(r_p) \mp \frac{1}{2}\Delta_p \frac{dF^{(p)}}{dr}. \quad (1.2)$$

As a result, we obtain from conditions (1.1) the relationship

$$F^{(0)}(r_2) - F^{(0)}(r_1) = \Delta_p \frac{dF^{(p)}}{dr}. \quad (1.3)$$

It is well known that, in the vacuum regions of the waveguide, the electromagnetic field components are described by linear combinations of cylinder functions of the argument $\chi_0 r$, where

$$\chi_0^2 = k_z^2 - \frac{\omega^2}{c^2}. \quad (1.4)$$

Under the strong inequality

$$|\chi_0|\Delta_p \ll 1, \quad (1.5)$$

we take into account the smoothness of cylinder functions and write the approximate relationship

$$F^{(0)}(r_2) - F^{(0)}(r_1) \approx F^{(0)}(r_p + 0) - F^{(0)}(r_p - 0), \quad (1.6)$$

which holds exactly in the limit $\Delta_p \longrightarrow 0$. Hence, from relationships (1.3) and (1.6), we finally obtain

$$\{F^{(0)}(r_p)\} \equiv F^{(0)}(r_p + 0) - F^{(0)}(r_p - 0)$$
$$= \lim_{\Delta_p \to 0}\left(\Delta_p \frac{dF^{(p)}}{dr}\right). \quad (1.7)$$

Relationship (1.7) is a local one, because it relates the field components at the same point r_p. Consequently, relationship (1.7) can be used as a boundary condition. However, in this way, the necessary formal transformations of this relationship should rest on a constructive physical approach. A description of the plasma in terms of the boundary condition of the form (1.7) will be called an "infinitely thin plasma approximation." It should be stressed that this approximation, as well as the basic expansion (1.2), removes from consideration electromagnetic waves whose fields are localized in the plasma volume. That is why we restrict ourselves to considering surface waves. However, it is precisely these waves that are of interest in the context of application to plasma microwave electronics.

Note that, if the right-hand side of relationship (1.7) equals zero, then the corresponding field component is continuous at an infinitely thin plasma cylinder. However, this does not mean that the field component is not perturbed by the plasma in the waveguide: there may be a discontinuity in its radial derivative. If the right-hand side of relationship (1.7) is nonzero, then the field component at the plasma cylinder is discontinuous. The discontinuity should not be understood in the strict sense (i.e., as a discontinuity in a continuous physical quantity), but merely as a strong change of the field component on the radial distance Δ_p across the plasma region in the waveguide. For a small plasma thickness Δ_p, such a strong change in the field component may conveniently be regarded as a discontinuity.

2. INFINITELY STRONG EXTERNAL MAGNETIC FIELD

Here, we consider a waveguide in an infinitely strong external magnetic field. We are interested in E-waves, whose electromagnetic field has the only nonzero components E_z, E_r, and B_φ, which satisfy the Maxwell equations [9]

$$ik_z E_r - \frac{dE_z}{dr} = i\frac{\omega}{c}B_\varphi, \quad k_z B_\varphi = \frac{\omega}{c}E_r,$$
$$\frac{1}{r}\frac{d}{dr}(rB_\varphi) = -i\frac{\omega}{c}\varepsilon_\| E_z, \quad (2.1)$$

where $\varepsilon_\| = 1 - \omega_p^2/\omega^2$ is the longitudinal dielectric function of the plasma and ω_p is the electron Langmuir frequency. In the vacuum regions of the waveguide, we should set $\varepsilon_\| = 1$.

Equations (2.1) yield, first, the expressions for the components E_r and B_φ,

$$E_r = -i\frac{k_z}{\chi_0^2}\frac{dE_z}{dr}, \quad B_\varphi = -i\frac{\omega}{c\chi_0^2}\frac{dE_z}{dr} \quad (2.2)$$

and, second, the equation for the component E_z,

$$\frac{1}{r}\frac{d}{dr}\left(r\frac{dE_z}{dr}\right) - \chi_0^2\varepsilon_\parallel E_z = 0. \quad (2.3)$$

Equation (2.3) with the boundary condition $E_z(R) = 0$ at the metal waveguide wall constitutes the eigenvalue problem for determining the spectra of E-waves. The solvability condition for this problem yields the following exact dispersion relation for the wave spectra $\omega = \omega(k_z)$ [10]:

$$D(\omega, k_z) \equiv \frac{k_p J_1(k_p r_1) + Q J_0(k_p r_1)}{k_p Y_1(k_p r_1) + Q Y_0(k_p r_1)}$$
$$\quad (2.4)$$
$$- \frac{k_p J_1(k_p r_2) + P J_0(k_p r_2)}{k_p Y_1(k_p r_2) + P Y_0(k_p r_2)} = 0.$$

Here, we have introduced the notation

$$Q = \chi_0\frac{I_1(\chi_0 r_1)}{I_0(\chi_0 r_1)}, \quad k_p^2 = -\chi_0^2\varepsilon_\parallel,$$
$$\quad (2.5)$$
$$P = \varphi_0\frac{I_1(\chi_0 r_2)K_0(\chi_0 R) + I_0(\chi_0 R)K_1(\chi_0 r_2)}{I_0(\chi_0 r_2)K_0(\chi_0 R) - I_0(\chi_0 R)K_0(\chi_0 r_2)},$$

where $J_l(x)$ and $Y_l(x)$ are Bessel and Neumann functions, $I_l(x)$ are modified Bessel functions of the first kind, and $K_l(x)$ are lth order modified Bessel functions of the second kind. The dispersion relation (2.4) not only describes the frequency spectra but also makes it possible to determine the transverse structure of the waveguide field. Thus, the expressions for the components $\{E_z(r), E_r(r), B_\varphi(r)\}$ can readily be obtained by substituting the eigenfrequencies $\omega(k_z)$ found from the dispersion relation (2.4) into Eqs. (2.3) and (2.2). Since these expressions are very involved, we do not write them out here and restrict ourselves to the relevant graphic representations obtained by solving the exact dispersion relation (2.4) numerically.

The results of a numerical solution of the exact dispersion relation (2.4) are illustrated in Fig. 1, in which curve *1* shows the dispersion law for the slow ($\omega < k_z c$) surface plasma wave in which we are interested here. Figure 2 illustrates the r dependence of the electromagnetic field components E_z, E_r, and B_φ calculated for this wave at the point A on the dispersion curve in Fig. 1 ($k_z = 6$ cm^{-1}). The corresponding calculations were carried out for the following parameter values of the plasma waveguide: $R = 2$ cm, $\omega_p = 10^{11}$ rad s^{-1}, $r_p = 1$ cm, and $\Delta_p = 0.1$ cm. Figure 1 also shows the "light" straight line $\omega = k_z c$ and curve *1a*, with which we will be concerned below. In Fig. 1 (and in subsequent analogous
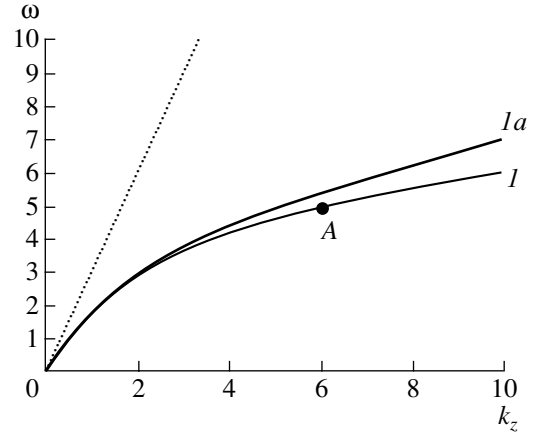
Fig. 1. Dispersion curves of the low-frequency slow surface wave of a thin-walled annular plasma in a waveguide in an infinitely strong external magnetic field: (*1*) solution to the exact dispersion relation and (*1a*) solution in the infinitely thin plasma approximation.

figures), the frequency is measured in 10^{10} rad s^{-1} and the wavenumber is expressed in inverse centimeters. Note that here we are interested only in the so-called cable plasma wave, whose frequency is the highest among all slow ($\omega < k_z c$) plasma waves [10, 11]. This wave has the highest phase velocity, and its transverse fundamental mode has the smallest transverse wavenumber. For $\Delta_p \ll r_p$, other plasma waves have far lower frequencies and thus are of no interest for the purposes of plasma relativistic microwave electronics. Recall also that their fields are localized in the plasma region of the waveguide, so that they cannot, in principle, be described by expansions (1.2).

From Fig. 2, we can see that, in the plasma region, the component E_z changes relatively insignificantly (Fig. 2a). Therefore, for the wave at hand, we have

$$\lim_{\Delta_p \to 0}\left(\Delta_p\frac{dE_z^{(p)}}{dr}\right) = 0. \quad (2.6)$$

On the contrary, the component B_φ (as well as E_r) changes strongly, which allows us to set

$$\lim_{\Delta_p \to 0}\left(\Delta_p\frac{dB_\varphi^{(p)}}{dr}\right) \neq 0. \quad (2.7)$$

The field structure just described is governed by the features of plasma polarization during the excitation of a cable plasma wave. In an infinitely strong magnetic field, the plasma electrons experience no transverse motion, so that the plasma is polarized only by longitudinal electron motion. In this case, it is only the space charge perturbations that are produced in the plasma volume and no surface charges are induced on the inner and outer boundaries of the plasma tube. In the language of potential theory, the plasma behaves as if it were a conventional layer. Mathematically, this circum-
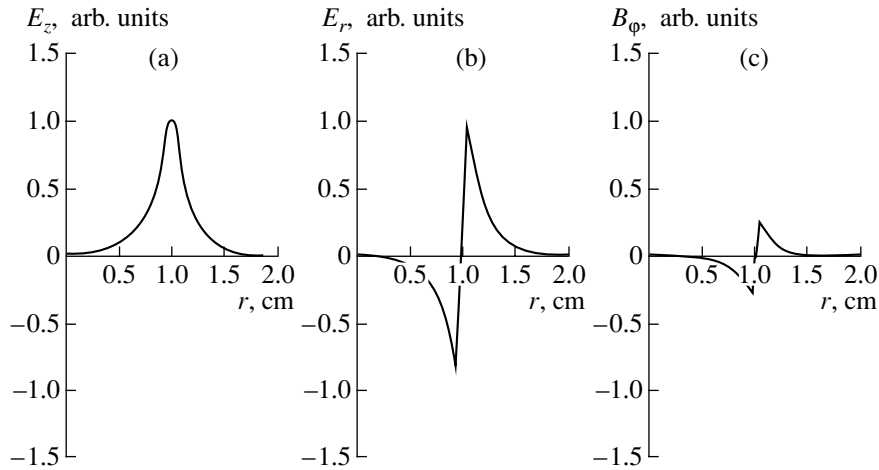
Fig. 2. Components E_z, E_r, and B_φ of the electromagnetic field of a low-frequency surface wave, calculated at point *A* on the dispersion curve *1* from Fig. 1.

stance is reflected by the limiting expressions (2.6) and (2.7).

From expressions (1.7) and (2.6), we obtain the first boundary condition for the field equations in vacuum:

$$\{E_z^{(0)}(r_p)\} = 0. \tag{2.8}$$

From expressions (1.7) and (2.7) and the second of expressions (2.2), we obtain the relationship

$$\left\{\frac{dE_z^{(0)}}{dr}(r_p)\right\} = \lim_{\Delta_p \to 0}\left(\Delta_p \frac{d^2 E_z^{(p)}}{dr^2}\right). \tag{2.9}$$

The second derivative of $E_z^{(p)}$ in this relationship can be determined from Eq. (2.3) with allowance for the inequality $\Delta_p \ll r_p$:

$$\frac{d^2 E_z^{(p)}}{dr^2} = \chi_0^2 \varepsilon_\parallel E_z^{(p)}. \tag{2.10}$$

Substituting expression (2.10) into relationship (2.9) gives

$$\left\{\frac{dE_z^{(0)}}{dr}(r_p)\right\} = \chi_0^2 \lim_{\Delta_p \to 0}(\Delta_p \varepsilon_\parallel E_z^{(p)}). \tag{2.11}$$

The limit on the right-hand side of equality (2.11) is calculated to be

$$\lim_{\Delta_p \to 0}(\Delta_p \varepsilon_\parallel E_z^{(p)}) = \lim_{\Delta_p \to 0}\left[\left(\Delta_p - \frac{\Delta_p \omega_p^2}{\omega^2}\right)E_z^{(p)}\right]$$
$$= -\lim_{\Delta_p \to 0}\left(\frac{\Delta_p \omega_p^2}{\omega^2}E_z^{(p)}\right) = -\Delta_p \frac{\omega_p^2}{\omega^2}E_z^{(0)}(r_p). \tag{2.12}$$

When calculating limit (2.12), we took into account the following two circumstances: first, the product $\Delta_p \omega_p^2$ is

proportional to the total number of plasma electrons per unit length and thus is constant and, second, the continuity of the tangential component of the field and relationships (2.8) imply that the limiting value of $E_z^{(p)}$ is $E_z^{(0)}(r_p)$. We thus arrive at the following effective boundary conditions for an infinitely thin plasma cylinder in the case of excitation of the cable plasma wave of interest to us:

$$\{E_z^{(0)}(r_p)\} = 0,$$
$$\left\{\frac{dE_z^{(0)}}{dr}(r_p)\right\} = -\Delta_p \chi_0^2 \frac{\omega_p^2}{\omega^2}E_z^{(0)}(r_p). \tag{2.13}$$

Note that the second of the boundary conditions (2.13) is usually obtained by making the replacement

$$\omega_p^2 \longrightarrow \Delta_p \delta(r - r_p)\omega_p^2 \tag{2.14}$$

in the longitudinal dielectric function $\varepsilon_\parallel$ and then by integrating Eq. (2.3) over *r* in the vicinity of the plasma [10, 11].

However, the effective boundary conditions in the infinitely thin plasma approximation cannot always be obtained simply by integrating the field equations: in this way, it is often necessary to involve additional physical considerations.

The significance of the effective boundary conditions (2.13) lies in the fact that they greatly simplify mathematical matters, because there is no need to solve field equations in the plasma region of the waveguide. To be specific, let us derive the dispersion relation of the plasma wave in the infinitely thin plasma approximation and compare the resulting dispersion curve with the corresponding dispersion curve shown in Fig. 1. We also analyze the amount of information that is lost in

describing the plasma on the basis of the effective boundary conditions, or, in other words, we determine the extent to which the infinitely thin plasma approximation is inaccurate. In the vacuum regions (where $\varepsilon_\parallel = 1$), Eq. (2.3) has the solution

$$E_z^{(0)} = \begin{cases} AI_0(\chi_0 r), & r < r_p \\ B\left[I_0(\chi_0 r) - K_0(\chi_0 r)\dfrac{I_0(\chi_0 R)}{K_0(\chi_0 R)}\right], & r_p < r < R. \end{cases} \quad (2.15)$$

Substituting solution (2.15) into the boundary conditions (2.13) and eliminating the constants A and B, we arrive at the familiar dispersion relation for determining the frequency spectra of the waves in a waveguide with an infinitely thin plasma tube in an infinitely strong external magnetic field [10, 11]:

$$r_p \Delta_p \frac{\omega_p^2}{\omega^2} \chi_0^2 I_0^2(\chi_0 r_p)\left[\frac{K_0(\chi_0 r_p)}{I_0(\chi_0 r_p)} - \frac{K_0(\chi_0 R)}{I_0(\chi_0 R)}\right] = 1. \quad (2.16)$$

The dispersion curve $\omega(k_z)$ shown by heavier curve *1a* in Fig. 1 was calculated by solving the dispersion relation (2.16) for the same parameter values of the plasma and of the waveguide as those used to obtain the dispersion curve *1* by solving the exact dispersion relation (2.4). The two curves are seen to coincide in the long-wavelength range, in which inequality (1.5) is satisfied. However, when this inequality fails to hold, the dispersion curves deviate from one another. In the limit of large k_z values, the curve calculated from the exact dispersion relation asymptotically approaches ω_p, because the wave field becomes locked in the plasma volume. On the contrary, as k_z increases, the dispersion curve obtained in the infinitely thin plasma approximation approaches infinity according to the law

$$\omega = \omega_p \sqrt{k_z \Delta_p/2}. \quad (2.17)$$

It is clear that, for $k_z \Delta_p > 1$, dependence (2.17) proved to be incorrect. This is the main drawback of the infinitely thin plasma approximation. This approximation fails to describe the structuring of the field distribution in the plasma volume. However, in the short-wavelength range ($k_z \Delta_p > 1$), this structuring is important. On the other hand, the model of an infinitely thin annular plasma is valid under inequality (1.5), i.e., in the case that is of primary interest for the purposes of plasma relativistic microwave electronics.

3. WAVEGUIDE IN THE ABSENCE OF AN EXTERNAL MAGNETIC FIELD

Now, we proceed to the analysis of a waveguide in the absence of an external magnetic field. We are again interested in E-waves, whose electromagnetic field has the only nonzero components E_z, E_r, and B_φ, which satisfy the Maxwell equations

$$ik_z E_r - \frac{dE_z}{dr} = i\frac{\omega}{c}B_\varphi, \quad k_z B_\varphi = \frac{\omega}{c}\varepsilon_\perp E_r,$$

$$\frac{1}{r}\frac{d}{dr}(rB_\varphi) = -i\frac{\omega}{c}\varepsilon_\parallel E_z, \quad (3.1)$$

where the transverse dielectric function $\varepsilon_\perp = 1 - \omega_p^2/\omega^2$ of the plasma coincides with its longitudinal dielectric function $\varepsilon_\parallel$ [9]. In Eqs. (3.1), we must set $\varepsilon_\perp = \varepsilon_\parallel = 1$ in the vacuum regions of the waveguide.

From Eqs. (2.1), we obtain the expressions for the components E_r and B_φ,

$$E_r = -i\frac{k_z}{\chi^2}\frac{dE_z}{dr}, \quad B_\varphi = -i\frac{\omega}{c\chi^2}\varepsilon_\perp\frac{dE_z}{dr} \quad (3.2)$$

and the equation for the component E_z,

$$\frac{1}{r}\frac{d}{dr}\left(r\frac{dE_z}{dr}\right) - \chi^2 E_z = 0; \quad (3.3)$$

where $\chi^2 = k_z^2 - \varepsilon_\perp \omega^2/c^2$. Equation (3.3) is supplemented with the conventional boundary condition $E_z(R) = 0$. In the resulting eigenvalue problem, the dispersion relation for the spectra of the symmetric E-waves in a waveguide with an annular plasma in the absence of an external magnetic field has the form [9, 12]

$$D(\omega, k_z) \equiv \frac{qI_1(\chi r_1) - QI_0(\chi r_1)}{qK_1(\chi r_1) + QK_0(\chi r_1)}$$

$$- \frac{qI_1(\chi r_2) - PI_0(\chi r_2)}{qK_1(\chi r_2) - PK_0(\chi r_2)} = 0. \quad (3.4)$$

Here, we have introduced the notation

$$Q = \frac{I_1(\chi_0 r_1)}{I_0(\chi_0 r_1)}, \quad q = \varepsilon_\perp \frac{\chi_0}{\chi},$$

$$P = \frac{K_1(\chi_0 r_2)I_0(\chi_0 R) + I_1(\chi_0 r_2)K_0(\chi_0 R)}{K_0(\chi_0 r_2)I_0(\chi_0 R) - I_0(\chi_0 r_2)K_0(\chi_0 R)}. \quad (3.5)$$

Figure 3 shows the dispersion curves of slow ($\omega < k_z c$) surface plasma waves. The curves were obtained by solving Eq. (3.4) numerically for the following parameter values of the plasma waveguide: $R = 2$ cm, $\omega_p = 10^{11}$ rad s^{-1}, $r_p = 1$ cm, and $\Delta_p = 0.1$ cm. We can see that there are two surface waves: a low-frequency wave with a normal dispersion (curve *1*) and a high-frequency wave whose dispersion becomes anomalous as k_z increases (curve *2*). In the limit $k_z \longrightarrow \infty$, the dispersion curves both approach the frequency $\omega_p/\sqrt{2}$ [9, 12]. Figure 4 displays the r profiles of the components E_z, E_r, and B_φ of the electromagnetic field of the low-frequency wave. The profiles were calculated at point A of the dispersion curve *1* ($k_z = 6$ cm^{-1}).
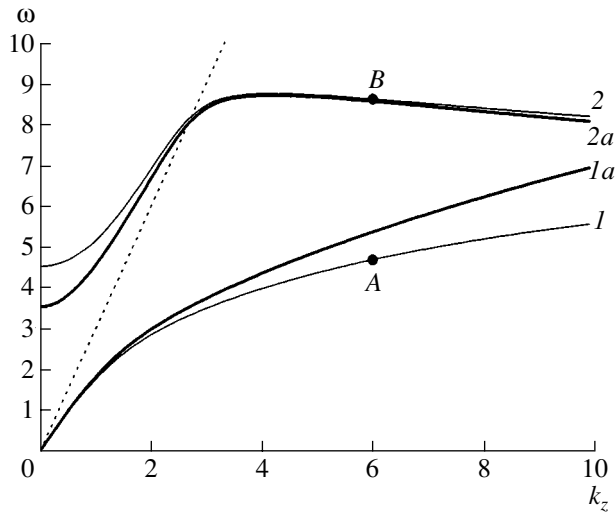
Fig. 3. Dispersion curves of the slow surface waves of a thin-walled annular plasma in a waveguide in the absence of an external magnetic field. Curves *1* and *1a* refer to a low-frequency wave with a normal dispersion and were calculated by solving the exact dispersion relation and in the infinitely thin plasma approximation, respectively. Curves *2* and *2a* refer to a high-frequency wave with an anomalous dispersion and were calculatedby solving the exact dispersion relation and in the infinitely thin plasma approximation, respectively.

According to Fig. 4, the components of the electromagnetic field of the low-frequency wave on the whole behave as the components of the wave field in the presence of an infinitely strong external magnetic field (Fig. 2); certain differences are observed only in the plasma region, but they are unimportant in view of the small plasma thickness. Consequently, the low-frequency wave satisfies relationships (2.6) and (2.7). As a

result, writing relationship (1.7) for the components E_z and B_φ and using the second of expressions (3.2) and Eq. (3.3), we arrive at the boundary conditions (2.13) for the low-frequency wave.

Now, we consider a high-frequency surface plasma wave with an anomalous dispersion (Fig. 3, curve *2*). The *r* profiles of the components E_z, E_r, and B_φ of the electromagnetic field of this wave are depicted in Fig. 5. The components were calculated at point *B* of the dispersion curve *2* ($k_z = 6$ cm^{-1}). We can see that the field structure in Fig. 5 differs radically from those in Figs. 2 and 4. The component E_z changes strongly across the plasma region (Fig. 5a). We can even say that, over the radial distance Δ_p, the component E_z undergoes a jump, in contrast to the component B_φ, which is continuous across this radial interval (Fig. 5c). The field structure just described is governed by the features of plasma polarization in this wave. In the absence of an external magnetic field, the plasma is polarized primarily by transverse electron motion. The excitation of a high-frequency surface wave gives rise to surface charges of opposite sign on the boundaries of the plasma tube, while the space charge inside the plasma remains unperturbed. In the terminology of potential theory, the plasma behaves as if it were a double layer. Mathematically, this circumstance is reflected by the limiting expressions

$$\lim_{\Delta_p \to 0} \left(\Delta_p \frac{dE_z^{(p)}}{dr} \right) \neq 0, \qquad (3.6)$$

$$\lim_{\Delta_p \to 0} \left(\Delta_p \frac{dB_\varphi^{(p)}}{dr} \right) = 0. \qquad (3.7)$$

Formula (1.7), the second of expressions (3.2), and
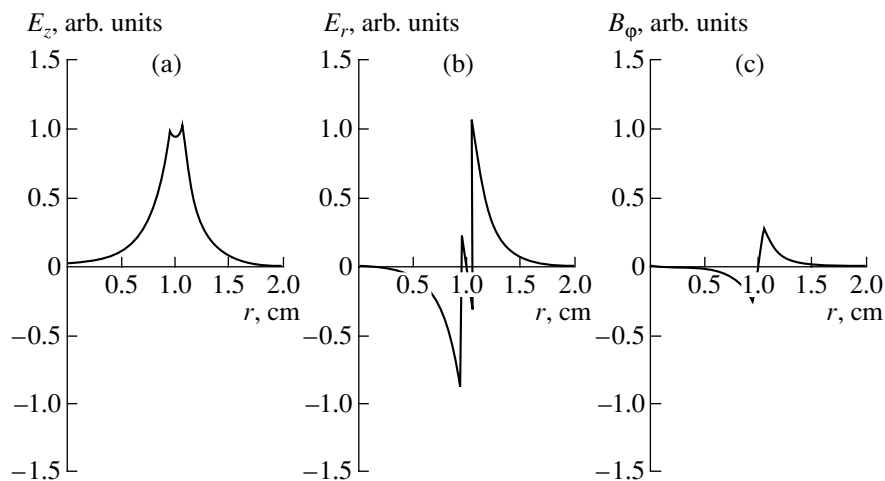
Fig. 4. Components E_z, E_r, and B_φ of the electromagnetic field of a low-frequency surface wave calculated at point *A* on the dispersion curve *1* from Fig. 3.
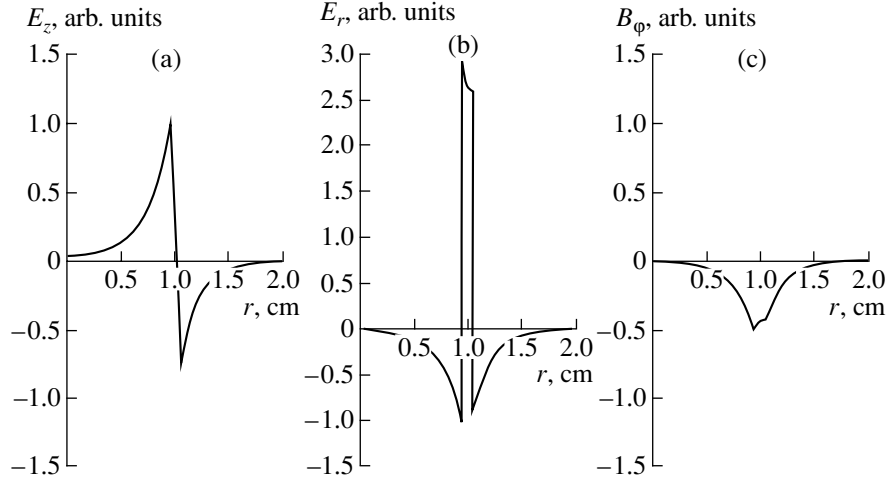
Fig. 5. Components E_z, E_r, and B_φ of the electromagnetic field of a high-frequency surface wave calculated at point B on the dispersion curve *2* from Fig. 3.

relationship (3.7) yield one of the boundary conditions:

$$\left\{\frac{dE_z^{(0)}}{dr}(r_p)\right\} = 0. \tag{3.8}$$

Let us calculate limit (3.6). First, using the second of expressions (3.2), we transform this limit to

$$\lim_{\Delta_p \to 0}\left(\Delta_p \frac{dE_z^{(p)}}{dr}\right) = i\frac{c\chi^2}{\omega\varepsilon_\perp}\lim_{\Delta_p \to 0}(\Delta_p B_\varphi^{(p)}). \tag{3.9}$$

Then, taking into account the fact that the physical component B_φ is continuous, we substitute the vacuum value $B_\varphi^{(0)}(r_p)$ into relationship (3.9) in order to express it in terms of the derivative of E_z with respect to r. As a result, we obtain

$$\lim_{\Delta_p \to 0}\left(\Delta_p \frac{dE_z^{(p)}}{dr}\right) = \frac{\chi^2}{\chi_0^2\varepsilon_\perp}\lim_{\Delta_p \to 0}\left(\Delta_p \frac{dE_z^{(0)}}{dr}\right). \tag{3.10}$$

Since the derivative is finite, the limiting value (3.10) vanishes, which indicates that there is no plasma in the waveguide. In fact, for $\Delta_p = 0$, opposite surface charges on the plasma boundaries merge and neutralize one another by virtue of the plasma quasineutrality. Consequently, the limiting transition in relationship (3.10) should be understood as a decrease in the plasma thickness to a value below which the infinitely thin plasma approximation fails to hold:

$$\lim_{\Delta_p \to 0}\left(\Delta_p \frac{dE_z^{(0)}}{dr}\right) = \Delta_p \frac{dE_z^{(0)}}{dr}(r_p). \tag{3.11}$$

Further, we substitute relationship (3.10) into expression (1.7) and take into account relationship (3.11) and boundary condition (3.8) to obtain the following final boundary conditions for describing an infinitely thin tube of an unmagnetized plasma in the case of excitation of a high-frequency surface plasma wave with an anomalous dispersion:

$$\left\{\frac{dE_z^{(0)}}{dr}(r_p)\right\} = 0,$$
$$\{E_z^{(0)}(r_p)\} = \Delta_p \frac{\chi^2}{\chi_0^2\varepsilon_\perp}\frac{dE_z^{(0)}}{dr}(r_p). \tag{3.12}$$

As an example, let us consider the dispersion properties of a high-frequency surface wave with an anomalous dispersion in the infinitely thin plasma approximation with no external magnetic field present. Inserting solutions (2.15) into the boundary conditions (3.12) and eliminating the constants A and B, we arrive at the following dispersion relation for a high-frequency surface wave with an anomalous dispersion:

$$1 - \frac{\omega_p^2}{\omega^2}$$
$$= -r_p\Delta_p\chi^2 I_1^2(\chi_0 r_p)\left[\frac{K_1(\chi_0 r_p)}{I_1(\chi_0 r_p)} + \frac{K_0(\chi_0 R)}{I_0(\chi_0 R)}\right]. \tag{3.13}$$

As before, a low-frequency surface wave with a normal dispersion obeys dispersion relation (2.16). The dispersion curves obtained by solving Eqs. (2.16) and (3.13) are represented by heavier curves *1a* and *2a* in Fig. 3. Recall that curves *1* and *2* in this figure were obtained by solving the exact dispersion relation (3.4),
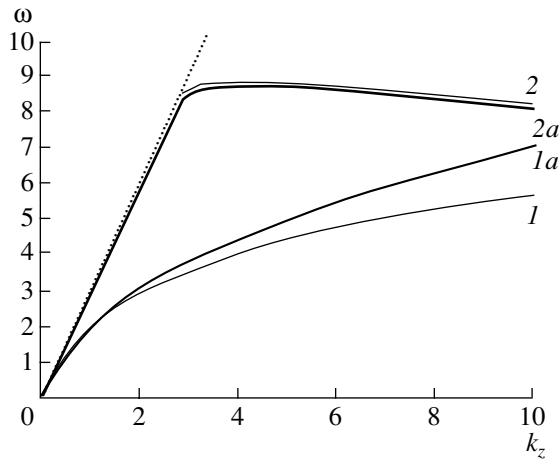
Fig. 6. Spectra of the surface waves of a thin-walled annular plasma with a free surface: curves *1* and *2* were calculated by solving the exact dispersion relation and curves *1a* and *2a* were obtained in the infinitely thin plasma approximation.
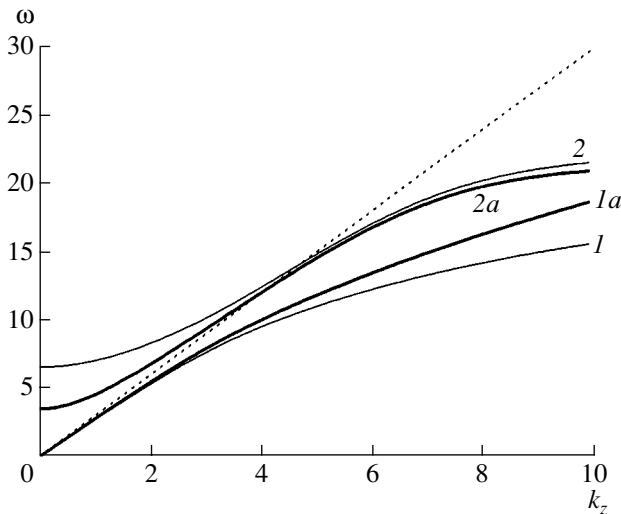
Fig. 7. Spectra of the surface waves of a thin-walled annular plasma of high density: curves *1* and *2* were calculated by solving the exact dispersion relation and curves *1a* and *2a* were obtained in the infinitely thin plasma approximation.

i.e., without assuming that the wall of the plasma tube is infinitely thin. We again find good agreement between the results obtained in different ways. An especially impressive agreement is observed between the results obtained for a high-frequency surface wave in the frequency range $\omega < k_z c$. In this frequency range, which is the most important for the purposes of plasma relativistic microwave electronics, curves *2* and *2a* coincide almost exactly. Moreover, they are qualitatively similar in shape even in the range $\omega > k_z c$, which was not supposed to be included in our analysis. As for the low-frequency surface wave, the correlation

between curves *1* and *1a* is even worse than that in the case of an infinitely strong external magnetic field. This stems from the fact that, when the finite plasma thickness is taken into account, the frequency in the short-wavelength limit approaches ω_p in an infinitely strong external magnetic field and $\omega_p/\sqrt{2}$ in the absence of the external field. However, in the long-wavelength range, the spectra of the low-frequency surface wave coincide almost exactly.

Another piece of evidence that the infinitely thin plasma approximation may be judged adequate is provided by Fig. 6, which displays the spectra of surface waves in the case of a thin-walled annular plasma with a free surface. This case corresponds to an infinitely large radius *R* in Eqs. (2.16) and (3.13). The remaining parameters of the waveguide and the plasma are the same as in Figs. 1 and 3, and the notation in Fig. 6 is the same as in Fig. 3. We see good coincidence between the exact and approximate dispersion curves. It should be emphasized that the infinitely thin plasma approximation correctly describes the following important property of waves on the free surface of the plasma: in the long-wavelength spectrum range, the velocity of these waves is equal to the speed of light. As is clear from Fig. 6, the high-frequency surface wave exhibits this property in a wide range of k_z values. This circumstance also demonstrates the correctness of the approximation at hand.

Up to this point, in speaking of high-frequency waves excited on the surface of a thin-walled annular plasma in the absence of an external magnetic field, we have used the term anomalous dispersion. However, this term is used not quite properly. Anomalous dispersion is significant only under the inequality

$$\frac{\Delta_p}{c/\omega_p} < 1. \qquad (3.14)$$

The calculations that have been discussed in deriving boundary conditions (3.12) and whose results are illustrated in Figs. 3–5 were carried out for a waveguide such that the parameter in inequality (3.14) was equal to 1/3. As the plasma density increases, inequality (3.14) becomes violated and anomalous dispersion changes to a normal dispersion, or, more precisely, the dispersion remains anomalous in the range of increasingly short wavelengths, where the infinitely thin plasma approximation fails to hold. That is why it is expedient to consider the accuracy of this approximation in the long-wavelength range [see inequality (1.5)], in which condition (3.14) is violated.

Figure 7 shows the dispersion curves calculated for a plasma whose density is one order of magnitude higher than in the previous figures, specifically, $\omega_p = 3 \times 10^{11}$ rad s^{-1}, the remaining parameters being the same as in Fig. 3. One can see that, in the range of relativistic wave phase velocities, which is important for the purposes of plasma relativistic microwave electronics, the

infinitely thin plasma approximation is quite accurate. The dispersion of the waves described by curves *2* and *2a* in Fig. 7 is anomalous at k_z values larger than those presented in the figure.

To conclude the discussion of the case of a thin-walled annular plasma in the absence of an external magnetic field, note that, unlike boundary conditions (2.13), conditions (3.12) cannot be derived by integrating the field equations with a δ-shaped radial plasma profile (2.14) over the radial coordinate *r*. In fact, integration of the third of Eqs. (3.1) leads to the relationship

$$\{B_\varphi^{(0)}\} = i\frac{\omega}{c}\Delta_p\frac{\omega_p^2}{\omega^2}E_z^{(p)}(r_p). \qquad (3.15)$$

However, taking into account the fact that the plasma in a high-frequency surface wave has the structure of a double layer and relying on Fig. 5a, we can conclude that $E_z^{(p)}(r_p) = 0$, in which case relationship (3.15) and the second of expressions (3.2) yield the first of the boundary conditions (3.12). Then, we integrate the second of Eqs. (3.1) and take into account the finiteness of B_φ to obtain $\Delta_p\omega_p^2E_r^{(p)}(r_p) = 0$. Consequently, since the line plasma density is constant ($\Delta_p\omega_p^2 = \text{const}$), we deal with one of the two possible cases: either the wave is absent (which is certainly not the case) or the equality $E_r^{(p)}(r_p) = 0$ holds (which contradicts Fig. 5b). The fact that the boundary conditions (3.12) cannot be derived by integrating the field equations with a δ-shaped radial plasma profile has a simple physical meaning: the existence of a high-frequency surface wave is governed by the processes on the boundaries of the plasma tube rather than by the processes occurring in the plasma volume.

4. EXTERNAL MAGNETIC FIELD OF FINITE STRENGTH

Here, we consider the general case of an external magnetic field of arbitrary strength. The dielectric tensor of a cold electron plasma in an external field has the form [9, 12]

$$\varepsilon_{ij} = \begin{pmatrix} \varepsilon_\perp & ig & 0 \\ -ig & \varepsilon_\perp & 0 \\ 0 & 0 & \varepsilon_\parallel \end{pmatrix}. \qquad (4.1)$$

Here, $i, j = r, \varphi, z$;

$$\varepsilon_\perp = 1 - \frac{\omega_p^2}{\omega^2 - \Omega_e^2}, \quad g = -\frac{\omega_p^2\Omega_e}{\omega(\omega^2 - \Omega_e^2)},$$
$$\varepsilon_\parallel = 1 - \frac{\omega_p^2}{\omega^2}, \qquad (4.2)$$

and Ω_e is the electron cyclotron frequency. It is well known that, at a finite frequency Ω_e, the electromagnetic field in a plasma waveguide does not split into independent E- and H-type fields [9]. Consequently, we must start with a complete set of equations for the six components of the electromagnetic field:

$$ik_zE_r - \frac{dE_z}{dr} = i\frac{\omega}{c}B_\varphi,$$

$$k_zB_\varphi = \frac{\omega}{c}\varepsilon_\perp E_r + \left[i\frac{\omega}{c}gE_\varphi\right],$$

$$\frac{1}{r}\frac{d}{dr}(rB_\varphi) = -i\frac{\omega}{c}\varepsilon_\parallel E_z,$$

$$k_zE_\varphi = -\frac{\omega}{c}B_r, \qquad (4.3)$$

$$ik_zB_r - \frac{dB_z}{dr} = -i\frac{\omega}{c}\varepsilon_\perp E_\varphi - \left[\frac{\omega}{c}gE_r\right],$$

$$\frac{1}{r}\frac{d}{dr}(rE_\varphi) = i\frac{\omega}{c}B_z.$$

Of these six equations, the first three are the equations for components E_z, E_r, and B_φ of the E-type field and the remaining three are the equations for components B_z, B_r, and E_φ of the H-type field. In Eqs. (4.3), these two triples of the components are coupled by the terms in square brackets.

From Eqs. (4.3), transverse components E_r, E_φ, B_r, and B_φ of the electromagnetic field in a waveguide are expressed in terms of longitudinal components E_z and B_z and their derivatives with respect to *r* as follows:

$$E_r = \xi^{-1}\left\{-ik_z\chi^2\frac{dE_z}{dr} - g\frac{\omega^3}{c^3}\frac{dB_z}{dr}\right\},$$

$$E_\varphi = \xi^{-1}\left\{i\frac{\omega}{c}\chi^2\frac{dB_z}{dr} - gk_z\frac{\omega^2}{c^2}\frac{dE_z}{dr}\right\},$$

$$B_r = \xi^{-1}\left\{-ik_z\chi^2\frac{dB_z}{dr} + gk_z^2\frac{\omega}{c}\frac{dE_z}{dr}\right\}, \qquad (4.4)$$

$$B_\varphi = \xi^{-1}\left\{-i\varepsilon_\perp\frac{\omega}{c}\left(\chi^2 + \frac{g^2}{\varepsilon_\perp}\frac{\omega^2}{c^2}\right)\frac{dE_z}{dr} - gk_z\frac{\omega^2}{c^2}\frac{dB_z}{dr}\right\},$$

where $\chi^2 = k_z^2 - \varepsilon_\perp\omega^2/c^2$ and $\xi = \chi^4 - g^2\omega^4/c^4$. With expressions (4.4), Eqs. (4.3) yield the following set of
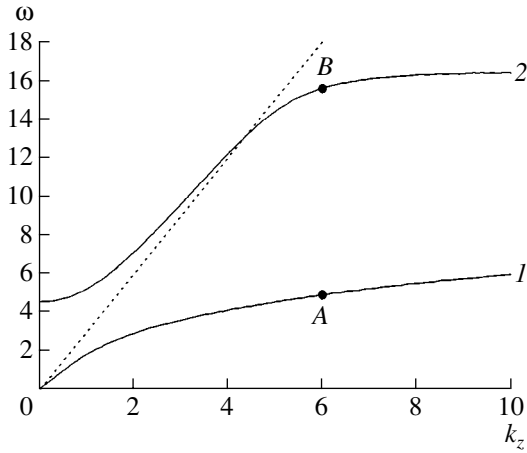
Fig. 8. Dispersion curves of (*1*) the low-frequency and (*2*) high-frequency surface waves of a thin-walled annular plasma in a waveguide in an external magnetic field of finite strength (the case $\Omega_e > \omega_p$ corresponds to a strong magnetic field). The curves were calculated by solving the exact dispersion relation.
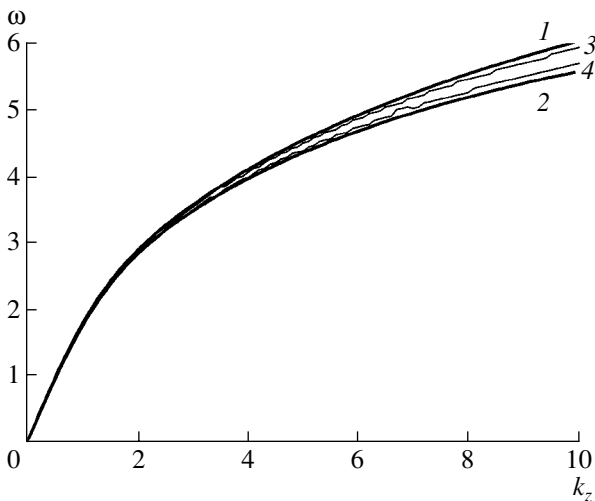
Fig. 9. Exact dispersion curves of the low-frequency surface waves of a thin-walled annular plasma in a waveguide in magnetic fields of different strengths: (*1*) $\Omega_e = \infty$, (*2*) $\Omega_e = 0$, (*3*) $\Omega_e = 1.5 \times 10^{11}$ rad s^{-1}, and (*4*) $\Omega_e = 0.5 \times 10^{11}$ rad s^{-1}.[1]

equations for longitudinal components E_z and B_z of the electric and magnetic fields:

$$\left(\chi^2 + \frac{g^2}{\varepsilon_\perp}\frac{\omega^2}{c^2}\right)\Delta_\perp E_z - \xi\frac{\varepsilon_\|}{\varepsilon_\perp}E_z \;=\; ik_z\frac{\omega}{c}\frac{g}{\varepsilon_\perp}\Delta_\perp B_z,$$

$$\chi^2\Delta_\perp B_z - \xi B_z = -ik_z\frac{\omega}{c}g\Delta_\perp E_z, \tag{4.5}$$

---

[1]In Fig. 9, curves *3* and *4* should be smoothed out, because the small-scale fluctuations in them are associated exclusively with the computational process.

where $\Delta_\perp = \dfrac{1}{r}\dfrac{d}{dr}r\dfrac{d}{dr}$ is the transverse Laplace operator in cylindrical coordinates. Supplementing Eqs. (4.5) with boundary conditions $E_z(R) = E_\varphi(R) = 0$, we arrive at the boundary-value problem, which is, however, very complicated to solve analytically, especially in the case of an annular plasma. Since the solution in the form of a dispersion relation and expressions for the eigenfunctions [3, 5] is extremely involved, we do not write out it here, but the corresponding numerical results needed for our analysis will be discussed below.

When studying the plasma waveguide in a magnetic field of finite strength, we must distinguish between the cases of a strong ($\Omega_e > \omega_p$) and a weak ($\Omega_e < \omega_p$) external magnetic field. We start by considering the waveguide in a strong magnetic field, because, in this case, it is clearly possible to describe the limiting transition $\Omega_e \longrightarrow \infty$ to an infinitely strong external magnetic field. The characteristic dispersion curves for the relevant surface plasma waves are shown in Fig. 8. The curves were calculated by solving the exact dispersion relation for a plasma waveguide with the parameters $R = 2$ cm, $r_p = 1$ cm, $\Delta_p = 0.1$ cm, $\omega_p = 10^{11}$ rad s^{-1}, and $\Omega_e = 1.5 \times 10^{11}$ rad s^{-1}. The waveguide at hand differs from the waveguide with $\Omega_e = \infty$, whose dispersion curves are given in Fig. 1, only in that the electron cyclotron frequency is finite, the remaining parameters being the same. In Fig. 8, curve *1* illustrates the dispersion of a low-frequency plasma wave and curve *2* refers to a high-frequency plasma wave. Figure 1 differs from Fig. 8 chiefly in that it contains no dispersion curve of the high-frequency plasma wave. The explanation of this circumstance is really quite clear: for $\Omega_e \longrightarrow \infty$, the dispersion curve of the low-frequency plasma wave lies at infinitely high frequencies. In Fig. 8, the dispersion curve of the low-frequency plasma wave is of conventional shape. For $\Omega_e > \omega_p$, this curve asymptotically approaches ω_p in the short-wavelength limit $k_z \longrightarrow \infty$. Of course, this asymptotic behavior cannot be described by means of the infinitely thin plasma approximation. Recall that this approximation and the effective boundary conditions, which are the subject of our analysis, are aimed at describing the plasma waves in the opposite (long-wavelength) limit (1.5). Again, it should be stressed that, among the variety of slow ($\omega < k_z c$) surface plasma waves, we are interested here exclusively in transverse fundamental modes, namely, the low-frequency mode (curve *1*) and the high-frequency mode (curve *2*). Let us first derive the effective boundary conditions for the fields of the low-frequency plasma wave in the infinitely thin plasma approximation.

The above exact dispersion curves of the low-frequency wave (Figs. 1, 3, 8) are seen to depend weakly on the strength of the external magnetic field in the long-wavelength range. For illustrations, Fig. 9 shows exact dispersion curves calculated for different Ω_e val-
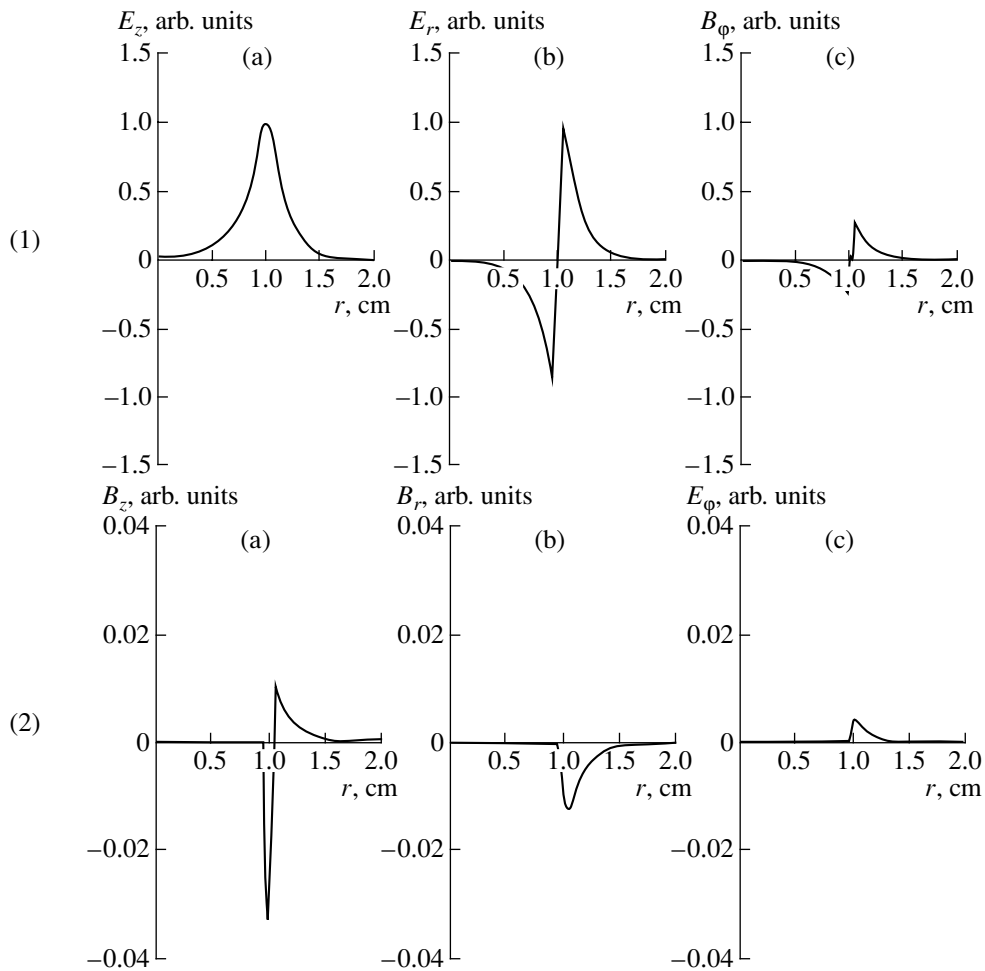
Fig. 10. Components (1) E_z, E_r, and B_φ and (2) B_z, B_r, and E_φ of the electromagnetic field of a low-frequency surface wave calculated at point *A* on dispersion curve *1* from Fig. 8 (the case $\Omega_e > \omega_p$ corresponds to a strong magnetic field).

ues (the remaining parameter values being the same): curve *1* is for $\Omega_e = \infty$, curve *2* is for $\Omega_e = 0$, and curve *3* is for $\Omega_e = 1.5 \times 10^{11}$ rad s^{-1} (curve *4* will be explained below). At sufficiently small k_z (in the example at hand, for $k_z < 2$–3 cm^{-1}), the dispersion curves are seen to coincide, while, at larger wavenumbers, they gradually deviate from each other. This circumstance stems from the small plasma thickness; moreover, the smaller the thickness Δ_p, the larger the interval of k_z values where the dispersion curves coincide. In a waveguide with a thin-walled annular plasma, not only the dispersion of the low-frequency waves depends weakly on the strength of the external magnetic field but also the fields of these waves are close in structure. Figure 10(1) displays field components E_z, E_r, and B_φ calculated for point *A* on dispersion curve *1* from Fig. 8 ($k_z = 6$ cm^{-1}). There are essentially no visible differences between this figure and Fig. 2, which refers to the case of an infinitely strong external magnetic field. The finiteness of the external magnetic field manifests itself primarily in

the fact that the electromagnetic field of the low-frequency plasma wave acquires the components of the H-type field. Figure 10(2) depicts components B_z, B_r, and E_φ calculated for the same point *A* on dispersion curve *1* from Fig. 8. A comparison of Fig. 10(2) with Fig. 10(1) shows that components B_z, B_r, and E_φ of the H-type field are small, because they are about two orders of magnitude smaller than components E_z, E_r, and B_φ (the units of measure in these figures are the same). Hence, in the case of a thin-walled annular plasma, the dispersion and the field structure of the low-frequency surface plasma wave in the long-wavelength spectral range both depend weakly on the strength of the external magnetic field: with a high degree of accuracy, they are the same as those for $\Omega_e = \infty$. It should be emphasized that this conclusion is valid only for a thin-walled annular plasma.

It is easy to understand why a low-frequency wave on the surface of a thin-walled annular plasma is so insensitive to the strength of the external magnetic

field. From Fig. 10(1), we can see that, inside the plasma, the component E_r, which is perpendicular to the external magnetic field, passes through zero and changes sign; consequently, the efficiency with which the component E_r affects the charges in the plasma volume is, on the average, close to zero. But it is the E_r component that induces the azimuthal current in the plasma and, as a consequence, gives rise to H-type fields. Mathematically, this effect is described by the term in square brackets in the next to last equation in set (4.3). Because of the relationship $E_r \approx 0$, which is, on the average, satisfied in the plasma volume, this term is small, thereby explaining the smallness of components B_z, B_r, and E_φ of the H-type field. From Fig. 10(1), we can also see that, inside the plasma, component E_z, which is aligned with the external magnetic field, is large. Therefore, the motion of the charges in the plasma is governed precisely by this component and is clearly insensitive to the external magnetic field (because the charges move just along its direction). Consequently, in the long-wavelength limit, the dispersion properties of the low-frequency plasma wave are approximately the same for any value of the electron cyclotron frequency Ω_e. The thinner the plasma, the higher the degree of confidence in the validity of the above analysis.

Hence, when describing a low-frequency plasma wave in the infinitely thin plasma approximation, we can neglect the coupling between the field components of different types. In this way, we can keep only the following three equations for the components of the E wave in the general set (4.3):

$$ik_z E_r - \frac{dE_z}{dr} = i\frac{\omega}{c}B_\varphi, \quad k_z B_\varphi = \frac{\omega}{c}\varepsilon_\perp E_r,$$
$$\frac{1}{r}\frac{d}{dr}(rB_\varphi) = -i\frac{\omega}{c}\varepsilon_\parallel E_z. \tag{4.6}$$

As for the remaining three equations, they can be used to estimate the effect of H-type fields. Using Eqs. (4.6), we express components E_r and B_φ in terms of E_z and obtain a separate equation for E_z:

$$E_r = -ik_z\frac{1}{\chi^2}\frac{dE_z}{dr}, \quad B_\varphi = -i\varepsilon_\perp\frac{\omega}{c}\frac{1}{\chi^2}\frac{dE_z}{dr}, \tag{4.7}$$

$$\Delta_\perp E_z - \chi^2\frac{\varepsilon_\parallel}{\varepsilon_\perp}E_z = 0. \tag{4.8}$$

Expressions (4.7) and Eq. (4.8) generalize formulas (2.2), (2.3), (3.2), and (3.3) to the case of infinitely strong external magnetic fields (only in relation to a low-frequency plasma wave!).

As follows from Figs. 10(1)a and 10(1)b, components E_z and B_φ satisfy relationships (2.6) and (2.7), in which case relationships (1.7) and (2.6) give the first of boundary conditions (2.8). Then, using relationships

(1.7) and (2.7), the second of formulas (2.2), and the second of formulas (4.7), we obtain

$$\left\{\frac{dE_z^{(0)}}{dr}(r_p)\right\} = \lim_{\Delta_p \to 0}\left(\Delta_p\varepsilon_\perp\frac{\chi_0^2}{\chi^2}\frac{d^2 E_z^{(p)}}{dr^2}\right). \tag{4.9}$$

Further, we find the second derivative of $E_z^{(p)}$ from Eq. (4.8) and substitute it into expression (4.9). As a result, we arrive at equality (2.11). The limiting transition is independent of whether the external magnetic field is finite or not. As a result, we can see that effective boundary conditions (2.13) are again satisfied for the fields of the low-frequency wave on the surface of an infinitely thin plasma tube. Consequently, dispersion relation (2.16) is also valid for finite external fields, so that its solutions correctly describe the dispersion of low-frequency waves on the surface of an infinitely thin plasma tube in external magnetic fields of different strengths. This conclusion is fully confirmed by Fig. 9, which shows the dispersion curves calculated from the exact mathematical model, and by Figs. 1 and 3, which compare the exact solutions to the dispersion relation with the solutions obtained in the infinitely thin plasma approximation.

Now, we proceed to the derivation of the effective boundary conditions for the fields of the high-frequency plasma wave. We begin by assuming that the external magnetic field is strong, $\Omega_e > \omega_p$. For this case, the exact dispersion curve for a high-frequency wave is shown by curve 2 in Fig. 8. In the short-wavelength range, the dispersion of the wave is anomalous and, as $k_z \longrightarrow \infty$, the dispersion curve approaches the electron cyclotron frequency Ω_e from above (the range of large k_z values is not shown in the figure). The highest frequency of this wave does not exceed the upper hybrid frequency $\Omega_h = \sqrt{\omega_p^2 + \Omega_e^2}$ (for the parameter values of Fig. 8, we have $\Omega_h \approx 1.8 \times 10^{11}$ rad s^{-1}), and the cutoff frequency $\omega(k_z = 0)$ is independent not only of Ω_e but also of ω_p. Figure 11 presents the field components of the high-frequency plasma wave, which were calculated at point B on dispersion curve 2 in Fig. 8. Components E_z, E_r, and B_φ are seen to be similar in shape to those of the high-frequency plasma wave in the absence of an external magnetic field (Fig. 5). Additionally, from Fig. 11(2), one can see that, in an external magnetic field of finite strength, components B_z, B_r, and E_φ are significant. Consequently, in the case at hand, it is not quite correct to speak of a small addition of the H-type field to the E wave: in an external magnetic field of finite strength, a high-frequency plasma wave is a mixed EH wave. Large values of components B_z, B_r, and E_φ stem from the fact that, inside the plasma, the transverse component E_r of the electric field of the high-frequency wave is significant, see Fig. 11(1)b.
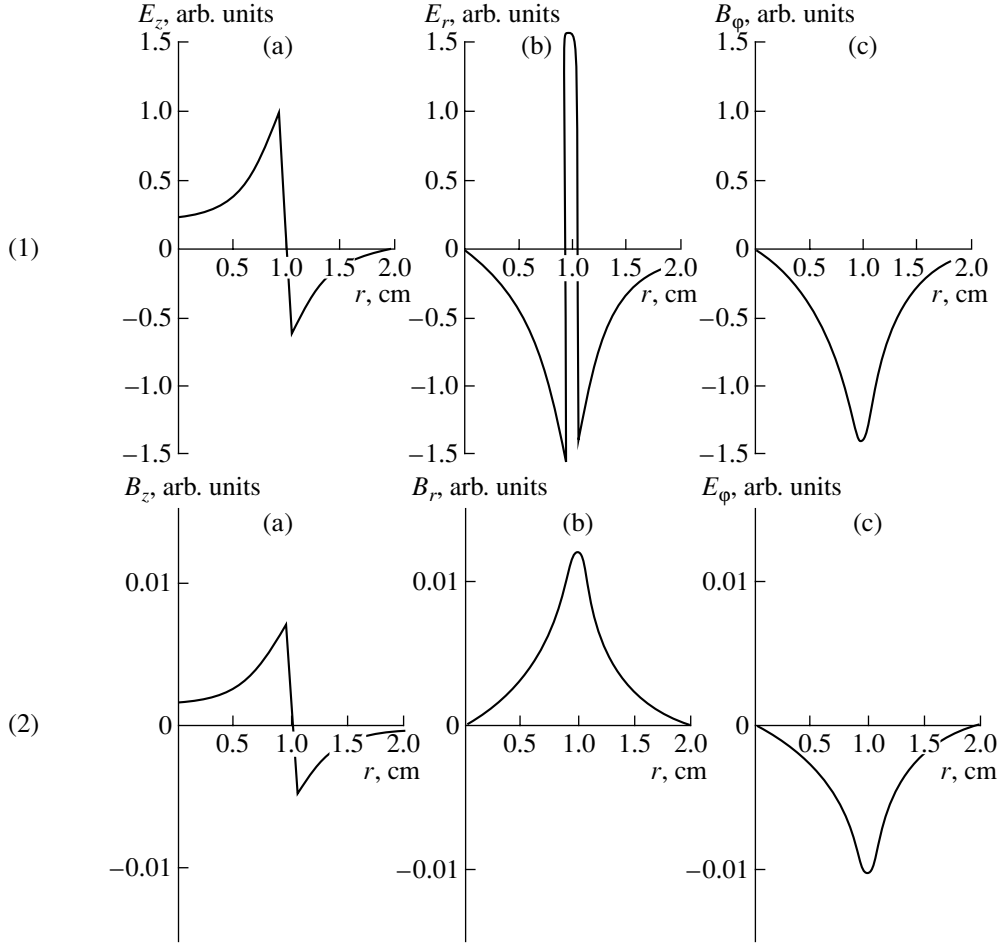
Fig. 11. Components (1) E_z, E_r, and B_φ and (2) B_z, B_r, and E_φ of the electromagnetic field of a high-frequency surface wave calculated at point B on dispersion curve *2* from Fig. 8 (the case $\Omega_e > \omega_p$ corresponds to a strong magnetic field).

Let us write out relationships (1.7) for electromagnetic field components that are tangent to the plasma boundaries:

$$\{E_z^{(0)}(r_p)\} = \lim_{\Delta_p \to 0}\left(\Delta_p \frac{dE_z^{(p)}}{dr}\right),$$

$$\{B_z^{(0)}(r_p)\} = \lim_{\Delta_p \to 0}\left(\Delta_p \frac{dB_z^{(p)}}{dr}\right), \quad (4.10)$$

$$\{E_\varphi^{(0)}(r_p)\} = \lim_{\Delta_p \to 0}\left(\Delta_p \frac{dE_\varphi^{(p)}}{dr}\right),$$

$$\{B_\varphi^{(0)}(r_p)\} = \lim_{\Delta_p \to 0}\left(\Delta_p \frac{dB_\varphi^{(p)}}{dr}\right). \quad (4.11)$$

First, we analyze relationships (4.11). Taking into account the shape of components $B_\varphi^{(p)}(r)$ and $E_\varphi^{(p)}(r)$, which are shown in Figs. 11(1)c and 11(2)c, and using almost the same analytical procedure as was used to

obtain boundary conditions (3.12), we can conclude that the limits on the right-hand sides of relationships (4.11) equal zero. As a result, we have

$$\{E_\varphi^{(0)}(r_p)\} = 0, \quad \{B_\varphi^{(0)}(r_p)\} = 0. \quad (4.12)$$

Taking account of the formulas

$$B_\varphi^{(0)} = -i\frac{\omega}{c\chi_0^2}\frac{dE_z^{(0)}}{dr}, \quad E_\varphi^{(0)} = i\frac{\omega}{c\chi_0^2}\frac{dB_z^{(0)}}{dr}, \quad (4.13)$$

which are valid in the vacuum regions of the waveguide [see expressions (4.4)], we obtain from relationships (4.12) the first two of the desired boundary conditions:

$$\left\{\frac{dE_z^{(0)}}{dr}(r_p)\right\} = 0, \quad \left\{\frac{dB_z^{(0)}}{dr}(r_p)\right\} = 0. \quad (4.14)$$

Second, we analyze relationships (4.10). Taking into account the shape of components $E_z^{(p)}(r)$ and $B_z^{(p)}(r)$, which are shown in Figs. 11(1)a and 11(2)a, and repeat-
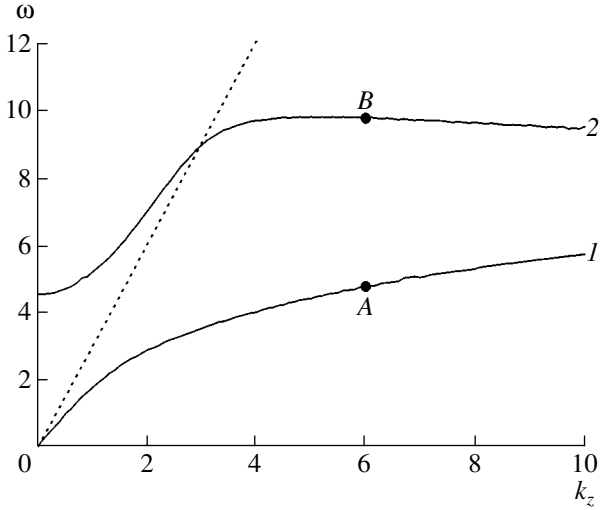
Fig. 12. Dispersion curves of (*1*) low-frequency and (*2*) high-frequency surface waves of a thin-walled annular plasma in a waveguide in an external magnetic field of finite strength (the case $\Omega_e < \omega_p$ corresponds to a strong magnetic field). The curves were calculated by solving the exact dispersion relation.

ing the procedure used to deduce boundary conditions (3.12), we can conclude that the limits on the right-hand sides of relationships (4.10) are nonzero. These limits can be calculated in essentially the same way as limit (3.11). Using the second and fourth of formulas (4.4), we express derivatives $E_z^{(p)}$ and $B_z^{(p)}$ in terms of $E_\varphi^{(p)}$ and $B_\varphi^{(p)}$:

$$\frac{dE_z^{(p)}}{dr} = i\frac{c}{\omega\varepsilon_\perp}\chi^2 B_\varphi^{(p)} + k_z\frac{g}{\varepsilon_\perp}E_\varphi^{(p)},$$

$$\frac{dB_z^{(p)}}{dr} = -i\frac{c}{\omega}\left(\chi^2 + \frac{g^2}{\varepsilon_\perp}\frac{\omega^2}{c^2}\right)E_\varphi^{(p)} + k_z\frac{g}{\varepsilon_\perp}B_\varphi^{(p)}. \tag{4.15}$$

Then, taking into account conditions (4.12) and the continuity of physical components B_φ and E_φ, we insert vacuum values $B_\varphi^{(0)}(r_p)$ and $E_\varphi^{(0)}(r_p)$ into relationships (4.15) in order to express them in terms of derivatives of E_z and B_z with respect to r. As a result, we obtain

$$\frac{dE_z^{(p)}}{dr}(r_p) = \frac{\chi^2}{\chi_0^2\varepsilon_\perp}\frac{dE_z^{(0)}}{dr} + ik_z\frac{\omega}{c}\frac{g}{\chi_0^2\varepsilon_\perp}\frac{dB_z^{(0)}}{dr},$$

$$\frac{dB_z^{(p)}}{dr}(r_p) = \frac{1}{\chi_0^2}\left(\chi^2 + \frac{g^2}{\varepsilon_\perp}\frac{\omega^2}{c^2}\right)\frac{dB_z^{(0)}}{dr} - ik_z\frac{\omega}{c}\frac{g}{\chi_0^2\varepsilon_\perp}\frac{dE_z^{(0)}}{dr}. \tag{4.16}$$

Further, we substitute expressions (4.16) into formulas (4.10) and combine the resulting expressions with conditions (4.14) to arrive at the following final boundary conditions for the fields of the high-frequency plasma

wave in an external magnetic field of finite strength in the infinitely thin plasma approximation:

$$\left\{\frac{dE_z^{(0)}}{dr}(r_p)\right\} = 0, \quad \left\{\frac{dB_z^{(0)}}{dr}(r_p)\right\} = 0,$$

$$\{E_z^{(0)}(r_p)\} = \Delta_p\frac{\chi^2}{\chi_0^2\varepsilon_\perp}\frac{dE_z^{(0)}}{dr}(r_p)$$

$$+ ik_z\frac{\omega}{c}\Delta_p\frac{g}{\chi_0^2\varepsilon_\perp}\frac{dB_z^{(0)}}{dr}(r_p), \tag{4.17}$$

$$\{B_z^{(0)}(r_p)\} = \Delta_p\frac{1}{\chi_0^2}\left(\chi^2 + \frac{g^2}{\varepsilon_\perp}\frac{\omega^2}{c^2}\right)\frac{dB_z^{(0)}}{dr}(r_p)$$

$$- ik_z\frac{\omega}{c}\Delta_p\frac{g}{\chi_0^2\varepsilon_\perp}\frac{dE_z^{(0)}}{dr}(r_p).$$

Now, we consider a waveguide in a weak magnetic field such that $\Omega_e < \omega_p$. Clearly, this case involves the limiting transition $\Omega_e = 0$. The representative dispersion curves of the surface plasma waves are shown in Fig. 12. The curves were calculated by solving the exact dispersion relation for a plasma waveguide with the parameters $R = 2$ cm, $r_p = 1$ cm, $\Delta_p = 0.1$ cm, $\omega_p = 10^{11}$ rad s^{-1}, and $\Omega_e = 0.5 \times 10^{11}$ rad s^{-1}. Curve *1* in Fig. 12 illustrates the dispersion of a low-frequency plasma wave, and curve *2* refers to a high-frequency plasma wave. The dispersion curve of the low-frequency plasma wave in Fig. 12 has the same shape as the corresponding curves in Figs. 1, 3, and 8. For $\Omega_e < \omega_p$, this curve asymptotically approaches the frequency $\omega_h/\sqrt{2}$ from below in the short-wavelength limit ($k_z \longrightarrow \infty$). In the same limit, the dispersion curve of the high-frequency plasma wave also approaches this frequency but from above, indicating that the dispersion of the high-frequency wave is anomalous. These short-wavelength asymptotics cannot be described in the infinitely thin plasma approximation.

Figure 13 presents the electromagnetic field components of the low-frequency plasma wave, which were calculated at point *A* on dispersion curve *1* in Fig. 12. The components are seen to be completely analogous in shape to those displayed in Fig. 10. The dispersion curve of the low-frequency plasma wave in Fig. 12 is reproduced by curve *4* in Fig. 9. In the long-wavelength limit, this curve coincides with the dispersion curves obtained for other strengths of the magnetic field. Hence, over the entire range of magnetic fields ($0 \le \Omega_e \le \infty$), a low-frequency wave on the surface of a thin-walled annular plasma has the same dispersion properties in the long-wavelength limit and its fields are close in structure. We can thus conclude that, in the infinitely thin plasma approximation, a low-frequency surface plasma wave can be described by boundary condi-
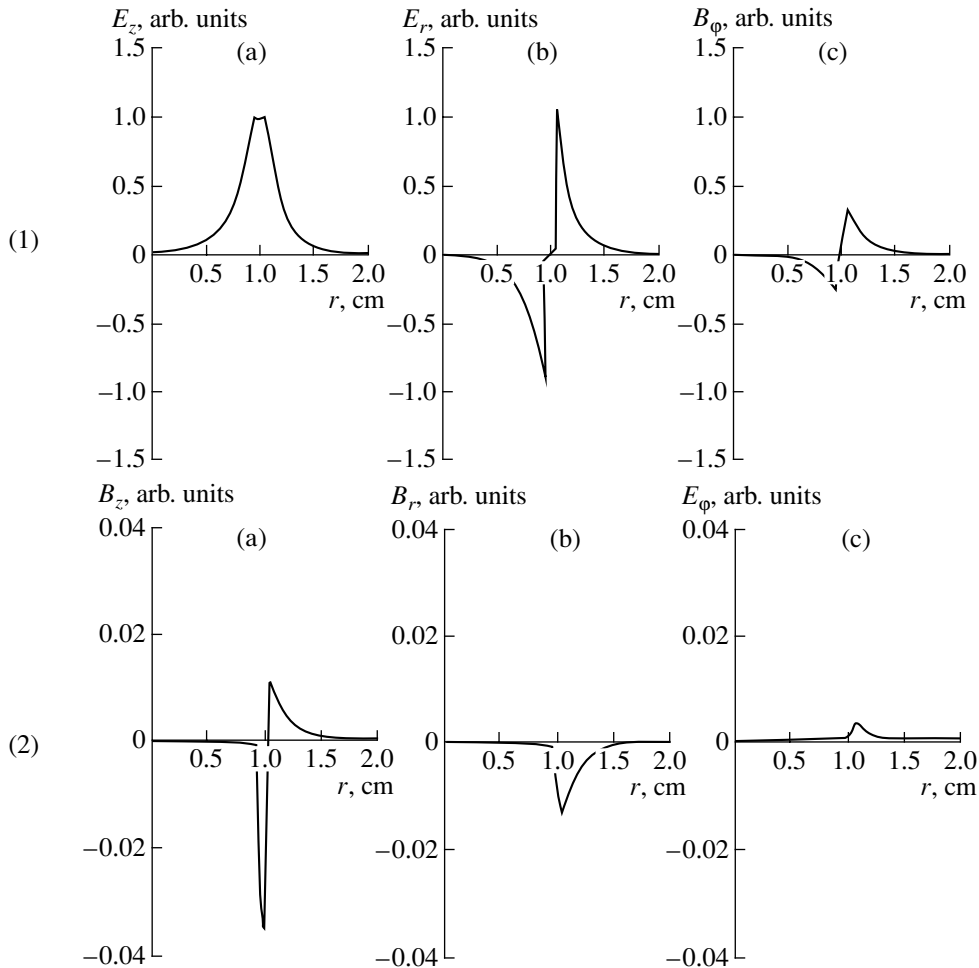
Fig. 13. Components (1) E_z, E_r, and B_φ and (2) B_z, B_r, and E_φ of the electromagnetic field of a low-frequency surface wave calculated at point A on dispersion curve 1 from Fig. 12 (the case $\Omega_e < \omega_p$ corresponds to a weak magnetic field).

tions (2.13) regardless of the strength of the external magnetic field.

Now, we consider a high-frequency plasma wave in a weak ($\Omega_e < \omega_p$) external magnetic field. Recall that the relevant characteristic dispersion curve is represented by curve 2 in Fig. 12. The electromagnetic field components of this wave that were calculated at point B on the dispersion curve 2 from Fig. 12 are shown in Fig. 14. We can see that the components have the same shapes as those obtained for $\Omega_e > \omega_p$, see Fig. 11. Consequently, when analyzing low-frequency and high-frequency surface waves in the long-wavelength limit in the infinitely thin plasma approximation, there is no reason to distinguish between the cases of a strong and a weak external magnetic field. In these cases, the low-frequency and high-frequency surface waves should be analyzed in different ways only in the short-wavelength range, which, however, is beyond the scope our study because it cannot be described in the infinitely thin plasma approximation. Hence, we can conclude that, in the infinitely thin plasma approximation, a high-fre-

quency surface plasma wave can be described by effective boundary conditions (4.17) regardless of the strength of the external magnetic field. In the particular case $\Omega_e = 0$, these conditions pass over to boundary conditions (3.12).

5. WAVES OF AN INFINITELY THIN PLASMA CYLINDER IN AN EXTERNAL MAGNETIC FIELD OF FINITE STRENGTH

Let us apply the above effective boundary conditions to investigate the spectra of the surface waves of a thin-walled annular plasma in a waveguide under the action of an external magnetic field of finite strength. We restrict ourselves to considering high-frequency waves, because it has already been established that the dispersion and the fields of the low-frequency waves of such a plasma are both independent of the strength of the external magnetic field. We supplement boundary conditions (4.17) with the requirement that the tangen-
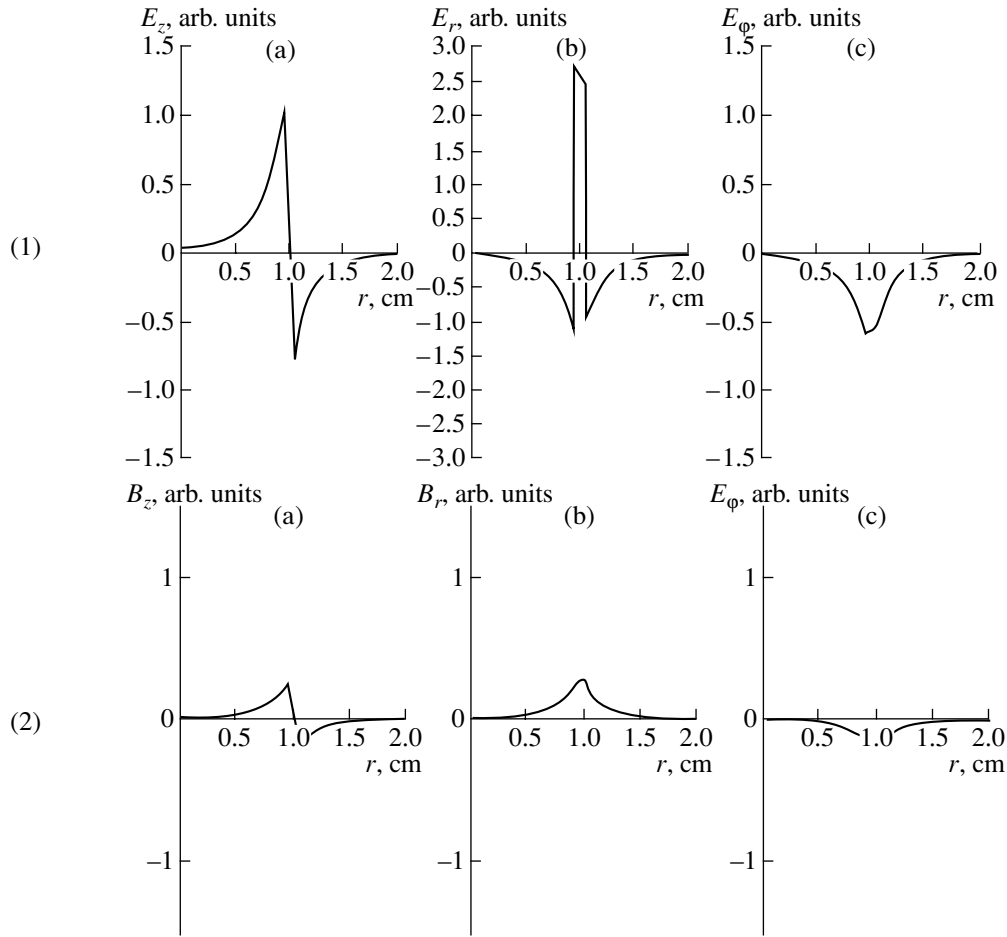
Fig. 14. Components (1) E_z, E_r, and B_φ and (2) B_z, B_r, and E_φ of the electromagnetic field of a high-frequency surface wave calculated at point B on dispersion curve 2 from Fig. 12 (the case $\Omega_e < \omega_p$ corresponds to a weak magnetic field).

tial component of the wave electric field be zero at the metal waveguide wall:

$$E_z(R) = E_\varphi(R) = 0. \tag{5.1}$$

Taking into account the second of formulas (4.13), we obtain from requirement (5.1) the following boundary conditions at the metal wall:

$$E_z^{(0)}(R) = 0, \quad \frac{dB_z^{(0)}}{dr}(R) = 0. \tag{5.2}$$

Conditions (4.17), together with conditions (5.2), constitute the full set of boundary conditions for the electromagnetic field of the high-frequency surface wave of a thin-walled annular plasma in an external magnetic field of finite strength.

The second of Eqs. (4.5) implies that, in the vacuum regions of the waveguide, the component $B_z^{(0)}$ satisfies the equation

$$\frac{1}{r}\frac{d}{dr}\left(r\frac{dB_z}{dr}\right) - \chi_0^2 B_z = 0. \tag{5.3}$$

The solution to Eq. (5.3) that satisfies the second of conditions (5.2) has the form

$$B_z^{(0)} = \begin{cases} CI_0(\chi_0 r), & r < r_p \\ D\left[I_0(\chi_0 r) + K_0(\chi_0 r)\dfrac{I_1(\chi_0 R)}{K_1(\chi_0 R)}\right], & r_p < r < R, \end{cases} \tag{5.4}$$

where C and D are constants and the component E_z, which satisfies the first of Eqs. (5.2), is, as before, given by formula (2.15). Substituting solutions (5.4) and (2.15) into boundary conditions (4.17) and eliminating constants A, B, C, and D, we obtain a dispersion relation for the spectra of a high-frequency plasma wave in a magnetic field of finite strength in the infinitely thin plasma approximation:

$$\left(1 + \Delta_p r_p \frac{\chi^2}{\varepsilon_\perp} G_E\right)\left[1 + \Delta_p r_p \left(\chi^2 + \frac{g^2}{\varepsilon_\perp}\frac{\omega^2}{c^2}\right)G_B\right]$$
$$= \Delta_p^2 r_p^2 k_z^2 \frac{\omega^2}{c^2}\frac{g^2}{\varepsilon_\perp^2} G_E G_B. \tag{5.5}$$
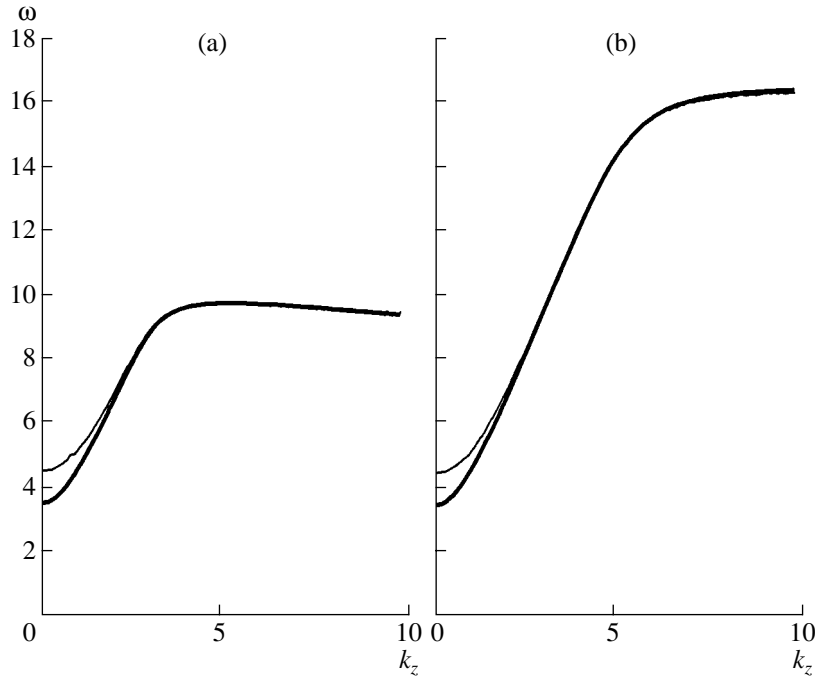
Fig. 15. Comparison between the dispersion curves calculated by solving the dispersion relation in the infinitely thin plasma approximation (heavier lines) and the exact dispersion relation (lighter lines).

Here, we have introduced the following notation for the geometric factors:

$$G_E = I_1^2(\chi_0 r_p)\left[\frac{K_1(\chi_0 r_p)}{I_1(\chi_0 r_p)} + \frac{K_0(\chi_0 R)}{I_0(\chi_0 R)}\right],$$

$$G_B = I_1^2(\chi_0 r_p)\left[\frac{K_1(\chi_0 r_p)}{I_1(\chi_0 r_p)} - \frac{K_1(\chi_0 R)}{I_1(\chi_0 R)}\right]. \qquad (5.6)$$

In a nonzero external magnetic field, the right-hand side of dispersion relation (5.5) vanishes ($g = 0$). As a result, dispersion relation (5.5) splits into the following two independent equations for the E and H waves, respectively:

$$1 + \Delta_p r_p \frac{\chi^2}{\varepsilon_\perp} G_E = 0, \qquad (5.7a)$$

$$1 + \Delta_p r_p \chi^2 G_B = 0. \qquad (5.7b)$$

One can readily see that Eq. (5.7a) coincides exactly with dispersion relation (3.13) and that Eq. (5.7b) has no roots for $\omega < k_z c$, as was to be expected, because, in this frequency range, there are no dispersion curves of the H waves. Consequently, Eq. (5.5) correctly describes the limiting transition to a zero external magnetic field. Note that dispersion relation (2.16) cannot be derived from Eq. (5.5) by taking the limit of an infinitely strong external magnetic field: these equations

describe qualitatively different types of surface plasma waves.

Figure 15 compares the dispersion curves calculated by solving approximate dispersion relation (5.5) and the exact dispersion relation. The dispersion curves obtained in the infinitely thin plasma approximation are shown by the heavier lines, and the exact dispersion curves are represented by the lighter lines. All of the dispersion curves were calculated for a plasma waveguide with the parameters $R = 2$ cm, $r_p = 1$ cm, $\Delta_p = 0.1$ cm, and $\omega_p = 10^{11}$ rad s^{-1} and for two values of the electron cyclotron frequency: $\Omega_e = 0.5 \times 10^{11}$ rad s^{-1} (Fig. 15a) and $\Omega_e = 1.5 \times 10^{11}$ rad s^{-1} (Fig. 15b). These parameter values are the same as those for the exact dispersion curves shown in Figs. 8 and 12, which are also reproduced in Fig. 15 in order to make the comparison with the approximate dispersion curves more illustrative. Figure 15 shows that the infinitely thin plasma approximation provides a high degree of accuracy: the approximate and exact dispersion curves differ only near the cutoff frequency, i.e., in the range where we did not intend to use this approximation. Note that the right-hand side of dispersion relation (5.5) is quadratic in the small parameter $k_z \Delta_p$. Consequently, to second order in this parameter, the spectra in the infinitely thin plasma approximation are determined from the very simple dispersion relation (5.7a), in which $\varepsilon_\perp$ is given by the first of expressions (4.2). The spectra calculated from Eq. (5.7a) also agree reasonably well with those obtained from more exact models.

6. APPLICATION TO PLASMA MICROWAVE ELECTRONICS

Here, we apply the infinitely thin plasma approximation to solve one of the main problems of plasma microwave electronics, namely, the problem of the Cherenkov excitation of surface plasma waves by an electron beam in a waveguide. We consider a waveguide with a thin-walled annular plasma and a thin-walled annular electron beam with the mean radius r_b and thickness $\Delta_b \ll r_b$. To be specific, we set $r_b < r_p$. The beam is assumed to be infinitely thin; i.e., it is incorporated only through certain effective boundary conditions. Let us derive these boundary conditions for the beam.

It is well known that the dielectric tensor of a straight electron beam in an external magnetic field of finite strength is more complex in structure than tensor (4.1) [9, 13]. Accordingly, the theory of the beam waves becomes much more elaborate, even when the beam is assumed to be infinitely thin. However, it is also a well-known fact that the Cherenkov interaction of a straight electron beam with a plasma is completely described by the contribution of the beam to the longitudinal dielectric function alone [9]:

$$\varepsilon_\parallel^{(b)} = 1 - \frac{\omega_b^2 \gamma^{-3}}{(\omega - k_z u)^2}, \qquad (6.1)$$

where ω_b is the Langmuir frequency of the beam electrons, u is their velocity, and $\gamma = (1 - u^2/c^2)^{-1/2}$ is the relativistic factor. In describing the Cherenkov interaction of a beam with a plasma, the contribution of the beam to the remaining elements of the dielectric tensor can be neglected. On the other hand, the longitudinal dielectric function of any medium (in particular, the beam and the plasma) enters only the effective boundary conditions (2.13). Taking into account the fact that the ratio ω_p^2/ω^2 in these conditions is equal to $1 - \varepsilon_\parallel$ and that the longitudinal dielectric function of the beam is given by formula (6.1), we arrive at the following effective boundary conditions for describing the Cherenkov interaction of an infinitely thin annular electron beam with a plasma:

$$\{ E_z^{(0)}(r_b) \} = 0,$$

$$\left\{ \frac{dE_z^{(0)}}{dr}(r_b) \right\} = -\Delta_b \chi_0^2 \frac{\omega_b^2 \gamma^{-3}}{(\omega - k_z u)^2} E_z^{(0)}(r_b). \qquad (6.2)$$

Of course, these conditions can be obtained not only in the same way as conditions (2.13) but also by repeating an analytical procedure very similar to that used to describe a low-frequency surface wave of an infinitely thin annular plasma.

Let us consider the Cherenkov interaction of an infinitely thin annular electron beam with an infinitely thin annular plasma in a waveguide. For simplicity, we

restrict ourselves to analyzing a beam and a plasma with free surfaces, i.e., we consider the limit $R \longrightarrow \infty$. A more general and complete analysis will be done in a separate paper. We start by deriving a dispersion relation describing the interaction of a beam with a high-frequency plasma wave. To do this, we substitute the solutions to the field equations in the vacuum regions of the waveguide ($0 < r < r_b$, $r_b < r < r_p$, $r_p < r < \infty$) into the boundary conditions (6.2) at $r = r_b$ and into the boundary conditions (4.17) at $r = r_p$. Taking account of the finiteness of the fields at infinity and eliminating the arbitrary constants in the solutions at hand, we obtain the following dispersion relation, describing the Cherenkov interaction of a beam with a high-frequency surface plasma wave:

$$(1 - \xi_b I_0(\chi_0 r_b) K_0(\chi_0 r_b))(1 + \xi_p^\uparrow I_1(\chi_0 r_p) K_1(\chi_0 r_p))$$
$$= \xi_b \xi_p^\uparrow I_0^2(\chi_0 r_b) K_1^2(\chi_0 r_p), \qquad (6.3)$$

where

$$\xi_b = \Delta_b r_b \chi_0^2 \frac{\omega_b^2 \gamma^{-3}}{(\omega - k_z u)^2},$$

$$\xi_p^\uparrow = \Delta_p r_p \frac{\chi^2}{\varepsilon_\perp}. \qquad (6.4)$$

For simplicity, the dispersion relation (6.3) was obtained to first order in the small parameter $k_z \Delta_p$.

The left-hand side of Eq. (6.3) contains the product of the two functions

$$D_b(\omega, k_z) \equiv 1 - \xi_b I_0(\chi_0 r_b) K_0(\chi_0 r_b),$$
$$D_p^\uparrow(\omega, k_z) \equiv 1 + \xi_p^\uparrow I_1(\chi_0 r_p) K_1(\chi_0 r_p). \qquad (6.5)$$

The dispersion relation $D_b(\omega, k_z) = 0$ determines the spectra of the surface waves of an infinitely thin annular beam with a free surface. In fact, if, in dispersion relation (2.16), we replace ω_p^2/ω^2 by $\omega_b^2 \gamma^{-3}(\omega - k_z u)^{-2}$ [see expression (6.1)] and take the limit $R \longrightarrow \infty$, then we can see that the resulting relation coincides with dispersion relation (6.5). In the same limit $R \longrightarrow \infty$, the dispersion relation $D_p^\uparrow(\omega, k_z) = 0$ coincides with Eq. (5.7a); i.e., to first order in $k_z \Delta_p$, it can be used to determine the spectrum of a high-frequency surface wave of an infinitely thin annular plasma with a free surface. Hence, as expected, general dispersion relation (6.3) refers to a system of two coupled oscillators—a beam–plasma oscillator. The coupling between the oscillators is accounted for by the right-hand side of this relation.

Now, we derive a dispersion relation describing the interaction of an electron beam with a low-frequency surface plasma wave. To do this, we substitute the solutions to the field equations in the vacuum regions of the waveguide ($0 < r < r_b$, $r_b < r < r_p$, $r_p < r < \infty$) into boundary conditions (6.2) at $r = r_b$ and into boundary condi-

tions (2.13) at $r = r_p$. Taking into account the finiteness of the fields at infinity and eliminating the arbitrary constants in the solutions at hand, we obtain the following dispersion relation, which describes the Cherenkov interaction of a beam with a low-frequency surface plasma wave:

$$(1 - \xi_b I_0(\chi_0 r_b) K_0(\chi_0 r_b))(1 - \xi_p^\downarrow I_0(\chi_0 r_p) K_0(\chi_0 r_p))$$
$$= \xi_b \xi_p^\downarrow I_0^2(\chi_0 r_b) K_0^2(\chi_0 r_p), \qquad (6.6)$$

where ξ_b is defined by expression (6.4) and

$$\xi_p^\downarrow = \Delta_p r_p \chi_0^2 \frac{\omega_p^2}{\omega^2}. \qquad (6.7)$$

The left-hand side of dispersion relation (6.6) is again the product of two functions—the first of functions (6.5) and the function

$$D_p^\downarrow(\omega, k_z) = 1 - \xi_p^\downarrow I_0(\chi_0 r_p) K_0(\chi_0 r_p). \qquad (6.8)$$

The dispersion relation $D_p^\downarrow(\omega, k_z) = 0$ describes the spectrum of a low-frequency surface wave of an infinitely thin annular plasma with a free surface. In fact, it coincides with Eq. (2.16) in the limit $R \longrightarrow \infty$. Hence, dispersion relation (6.6) also describes a system of two coupled oscillators.

At this point, it is important to make a comment regarding dispersion relation (6.8) and more general dispersion relation (2.16). These dispersion relations are well known, and, beginning with paper [11], they are routinely used to theoretically explain experiments in plasma microwave electronics and to perform particular calculations of plasma-filled electrodynamic systems. However, in many papers devoted to plasma relativistic microwave electronics (see, e.g., [6, 14, 15]), it was pointed out that dispersion relation (2.16) and all conclusions drawn from it are valid only in the limit of an infinitely strong external magnetic field. In the present work, it has been rigorously verified that dispersion relation (2.16) is valid for an external magnetic field of finite strength. Thereby, the results and conclusions of the above-cited theoretical and experimental investigations of the Cherenkov excitation of low-frequency surface waves of an infinitely thin plasma by an electron beam in a waveguide are actually applicable over a range far wider than previously thought. In the author's opinion, this is one of the most important results of the present paper. As for dispersion relation (6.3), it arises in the study of such new problem in plasma microwave electronics as the problem of the interaction of an electron beam with high-frequency surface waves of an infinitely thin plasma.

Figure 16 shows the dispersion curves calculated from dispersion relations (6.3) and (6.6) for a beam–plasma waveguide with the parameters $\omega_p = 25 \times 10^{10}$ rad s^{-1}, $\Omega_e = 50 \times 10^{10}$ rad s^{-1}, $r_p = 1$ cm, $r_b = 0.9$ cm, and $\Delta_p = \Delta_b = 0.1$ cm, the beam velocity and beam current being

$u = 2.6 \times 10^{10}$ cm/s and $I_b = 2$ kA, respectively. Since dispersion relations (6.3) and (6.6), which describe the interaction of an electron beam with different types of waves, are entirely independent of one another, the curves in Fig. 16 were obtained by matching the corresponding dispersion curves of the two groups. Specifically, for frequencies above 20×10^{10} rad s^{-1}, the dispersion curves were calculated from relation (6.3) and, for frequencies below 35×10^{10} rad s^{-1}, the dispersion curves were calculated from relation (6.6). Being plotted in the same figure (Fig. 16), the corresponding curves are seen to coincide surprisingly well in the common frequency range from 20×10^{10} to 35×10^{10} rad s^{-1}. Also shown in Fig. 16 (and in the next figure) are the Cherenkov resonance line $\omega = k_z u$ (short dashes) and the "light" straight line $\omega = k_z c$ (long dashes).

In Fig. 16, we can see that, in the beam–plasma waveguide under consideration, there are two instability regions, whose boundaries are indicated by the vertical straight lines: the frequency axis ($k_z = 0$), line α ($k_z \approx 4.9$ cm^{-1}), line β ($k_z \approx 18.5$ cm^{-1}), and line γ ($k_z \approx 19.9$ cm^{-1}). In the region of wavenumbers k_z from zero to line α, the instability is governed by the interaction of an electron beam with a low-frequency surface plasma wave under the Cherenkov resonance conditions. The structure of the dispersion curves allows us to conclude that this low-frequency instability is associated with the stimulated single-particle Cherenkov effect. In recent years, this instability has been thoroughly investigated both theoretically and experimentally for essentially the same parameters of the beam–plasma waveguide [6]. The second, far narrower, instability region lies between lines β and γ. In this range of wavenumbers, the instability is governed by the Cher-
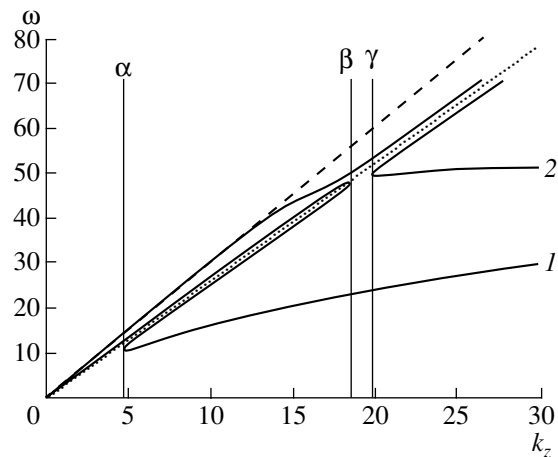
Fig. 16. Dispersion curves characterizing the Cherenkov instability in a waveguide with an infinitely thin annular plasma and an infinitely thin annular electron beam in the case of the minimum possible gap between the beam and the plasma.
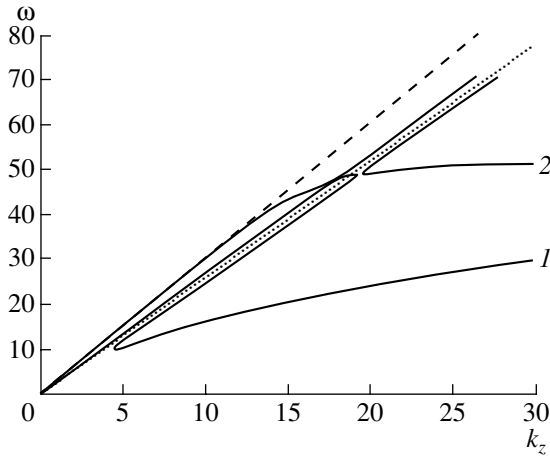
Fig. 17. Dispersion curves characterizing the Cherenkov instability in a waveguide with an infinitely thin annular plasma and an infinitely thin annular electron beam in the case of a large gap between the beam and the plasma.

enkov resonance interaction of an electron beam with a high-frequency surface plasma wave. Judging from the structure of the dispersion curves, this high-frequency instability is associated with the stimulated collective Cherenkov effect. To the best of my knowledge, this instability remains virtually uninvestigated. In the cited experiments on the interaction between thin-walled annular electron beams and thin-walled annular plasmas, no radiation was recorded in the frequency range of high-frequency instability [15, 16].

From the theory of plasma microwave electronics, it is well known that the character of the Cherenkov interaction of a thin-walled annular electron beam with a thin-walled annular plasma is governed by the gap $|r_p - r_b|$ between them [6, 14]. If the gap is sufficiently small, the beam interacts with the plasma under the single-particle Cherenkov resonance conditions. As the gap increases, the regime of the single-particle Cherenkov effect goes over to the collective Cherenkov regime. The high-frequency instability is much more sensitive to an increase in the gap $|r_p - r_b|$ than is the low-frequency instability. In a waveguide characterized by the dispersion curves shown in Fig. 16, we deal with the minimum possible gap (for $|r_p - r_b| = 0.1$ cm, the outer beam boundary $r_b + \Delta_b/2$ coincides with the inner plasma boundary $r_p - \Delta_p/2$). Nevertheless, high-frequency instability in this waveguide is associated with the collective Cherenkov effect. With increasing gap, the collective character of the high-frequency instability becomes even more pronounced, which manifests itself as a narrowing of the instability region. Figure 17 shows the dispersion curves calculated for a waveguide with the same parameters as in Fig. 16 but with a smaller beam radius ($r_b = 0.7$ cm). We can see that, as the gap is increased from 0.1 to 0.3 cm, the region of high-frequency instability becomes so narrow that it is hardly distinguished visually (in Fig. 17, this region is

determined by the inequalities $19.28 < k_z < 19.50$ cm^{-1}). As for the low-frequency instability, a comparison of Fig. 17 with Fig. 16 shows that it does not change its character. It is only at $r_b < 0.59$ cm (the remaining parameters being the same) that the single-particle Cherenkov regime of the low-frequency instability goes over to the collective regime, in which case the region of high-frequency instability turns out to be negligibly narrow.

Above, we have spoken of the instability region, i.e., the wavenumber interval in which the dispersion relation has not only real solutions but also complex solutions (in the plane of the complex frequency ω). As regards experimental investigations, it is also meaningful to speak of the region of wave amplification, i.e., the frequency range in which the dispersion relation has complex solutions in the plane of the complex wavenumber k_z. In the interaction of an electron beam with a high-frequency surface wave, the amplification region is extremely narrow. Thus, for the minimum possible gap, the boundaries of the amplification region can be inferred from Fig. 16: $47.2 \times 10^{10} < \omega < 49.4 \times 10^{10}$ rad s^{-1}. In this case, the relative width $\Delta\omega/\omega$ of the emission spectrum of the beam at the highest frequency is about 0.046 (which is smaller than 5%). Presumably, it is because of this feature of the high-frequency radiation that it was not recorded in the cited experimental investigations. Note that, in a weak external magnetic field ($\Omega_e < \omega_p$), the radiation spectrum at high frequencies is not much narrower than the low-frequency radiation spectrum. However, this effect was not investigated in the cited experiments.

The above characteristic features of the interaction of an electron beam with low- and high-frequency surface waves of an infinitely thin annular plasma (see the discussion of Figs. 16 and 17) are governed by the value of the resonance frequency. The higher the resonance frequency, the weaker is the coupling between the beam and the plasma wave, the narrower is the radiation spectrum, the lower is the instability growth rate, etc. All these effects are captured by dispersion relations (6.3) and (6.6). In order to see this, let us consider some particular solutions to the dispersion relations. Following [6, 14], we convert dispersion relation (6.6) to a generalized form:

$$((\omega - k_z u)^2 - \Omega_b^2)(\omega^2 - \Omega_{p\downarrow}^2) = \Theta_\downarrow \Omega_b^2 \Omega_{p\downarrow}^2, \quad (6.9)$$

where

$$\Omega_b^2 = \Delta_b r_b \chi_0^2 \omega_b^2 \gamma^{-3} I_0(\chi_0 r_b) K_0(\chi_0 r_b),$$
$$\Omega_{p\downarrow}^2 = \Delta_p r_p \chi_0^2 \omega_p^2 I_0(\chi_0 r_p) K_0(\chi_0 r_p) \quad (6.10)$$

are the squared frequencies of the beam wave and of the low-frequency plasma wave, respectively, and

$$\Theta_\downarrow = \frac{I_0(\chi_0 r_b) K_0(\chi_0 r_p)}{K_0(\chi_0 r_b) I_0(\chi_0 r_p)} \quad (6.11)$$

is the coupling coefficient for beam and plasma waves. Dispersion relation (6.3) can be written in a similar form:

$$((\omega - k_z u)^2 - \Omega_b^2)(\omega^2 - \Omega_h^2 + \Omega_{p\uparrow}^2) = \Theta_\uparrow \Omega_b^2 \Omega_{p\uparrow}^2, \quad (6.12)$$

where $\Omega_h = \sqrt{\omega_p^2 + \Omega_e^2}$ is the upper hybrid frequency and

$$\begin{aligned} \Omega_b^2 &= \Delta_b r_b \chi_0^2 \omega_b^2 \gamma^{-3} I_0(\chi_0 r_b) K_0(\chi_0 r_b), \\ \Omega_{p\uparrow}^2 &= \Delta_p r_p \chi^2 (\omega^2 - \Omega_e^2) I_1(\chi_0 r_p) K_1(\chi_0 r_p). \end{aligned} \quad (6.13)$$

As in the first of expressions (6.10), the quantity Ω_b^2 is the squared frequency of the beam wave (without allowance for the Doppler shift). The quantity $\Omega_{p\uparrow}^2$ enters the definition of the spectrum of a high-frequency plasma wave. Also, in the dispersion relation (6.12), the coupling coefficient for beam and plasma waves is denoted by

$$\Theta_\uparrow = \frac{I_0(\chi_0 r_b) K_1(\chi_0 r_p)}{K_0(\chi_0 r_b) I_1(\chi_0 r_p)}. \quad (6.14)$$

In the notation used for dispersion relations (6.9) and (6.12), the frequency spectra of the beam waves and of the low- and high-frequency plasma waves can be written, respectively, as

$$\begin{aligned} (\omega - k_z u)^2 &= \Omega_b^2, \\ \omega^2 &= \Omega_{p\downarrow}^2, \\ \omega^2 &= \Omega_h^2 - \Omega_{p\uparrow}^2. \end{aligned} \quad (6.15)$$

Of course, formulas (6.15) can be regarded as the expressions for spectra only tentatively. Since the quantities Ω_b^2, $\Omega_{p\downarrow}^2$, and $\Omega_{p\uparrow}^2$ are functions of ω, formulas (6.15) serve as equations for determining the eigenfrequencies. Examples of solutions to the second and third of Eqs. (6.15) are presented in Figs. 8 and 12, as well as in some other figures. Under the inequality

$$2\gamma^2 \left(\frac{\Omega_b}{k_z u}\right) \approx \left(4\Delta_b r_b \frac{\omega_b^2 \gamma^{-1}}{u^2}\right)^{\frac{1}{2}} \ll 1, \quad (6.16)$$

the first of Eqs. (6.15) yields the following expression for the spectrum of the slow wave of an electron beam:

$$\begin{aligned} \omega &= k_z u(1 - \sqrt{\alpha_b}), \\ \alpha_b &= \Delta_b r_b \frac{\omega_b^2 \gamma^{-5}}{u^2} I_0(k_z \gamma^{-1} r_b) K_0(k_z \gamma^{-1} r_b). \end{aligned} \quad (6.17)$$

First, we consider the instability of an electron beam in the interaction with a low-frequency surface plasma wave. We denote by $\omega_\downarrow$ and $k_{z\downarrow}$ the solution to the set of equations

$$\omega = \Omega_{p\downarrow}, \quad \omega = k_z u(1 - \sqrt{\alpha_b}). \quad (6.18)$$

It is obvious that, in the plane $(\omega_\downarrow, k_{z\downarrow})$, the values of ω and k_z are the coordinates of the point of the resonant interaction between a slow beam wave and a low-frequency surface wave. At $k_z = k_{z\downarrow}$, the solution to the dispersion relation (6.9) can be represented in the form

$$\omega = \omega_\downarrow + \delta\omega_\downarrow, \quad |\delta\omega_\downarrow| \ll 1. \quad (6.19)$$

Here, the inequality implies that the electron beam density is low, which agrees with inequality (6.16). We substitute solution (6.19) into dispersion relation (6.9) to obtain the following equation for the instability growth rate $\delta\omega_\downarrow$ in the interaction with a low-frequency wave:

$$\begin{aligned} &\delta\omega_\downarrow^2(- 2k_z u \sqrt{\alpha_b} + \delta\omega_\downarrow) \\ &= \frac{1}{2}\Theta_\downarrow \alpha_b \Omega_{p\downarrow} k_z^2 u^2 \left(1 - \frac{\partial\Omega_{p\downarrow}}{\partial\omega}\right)^{-1}. \end{aligned} \quad (6.20)$$

The right-hand side of this equation should be calculated at the resonant point $(\omega_\downarrow, k_{z\downarrow})$. From Eq. (6.20), we find the growth rates of the Cherenkov instability of an electron beam in the interaction with a low-frequency surface plasma wave:

$$\delta\omega_\downarrow = \begin{cases} \dfrac{-1 + i\sqrt{3}}{2}\omega_\downarrow\left[\dfrac{1}{2}\Theta_\downarrow \alpha_b\left(1 - \dfrac{\partial\Omega_{p\downarrow}}{\partial\omega}\right)^{-1}\right]^{1/3}, \\ \quad \sqrt{\alpha_b} \ll \Theta_\downarrow \\ i\dfrac{1}{2}\omega_\downarrow\left[\dfrac{1}{2}\Theta_\downarrow \sqrt{\alpha_b}\left(1 - \dfrac{\partial\Omega_{p\downarrow}}{\partial\omega}\right)^{-1}\right]^{1/2}, \\ \quad \Theta_\downarrow \ll \sqrt{\alpha_b}. \end{cases} \quad (6.21)$$

When deriving growth rates (6.21), we used the inequality $\alpha_b \ll 1$, which follows from inequality (6.16). The instability with the first of growth rates (6.21) is called a single-particle Cherenkov effect, and the instability with the second of the growth rates is called a collective Cherenkov effect. For the waveguide parameters of Figs. 16 and 17, the coupling coefficient $\Theta_\downarrow$ is larger than 0.37, which indicates that, when discussing these figures, we dealt with a single-particle Cherenkov effect.

We now consider the instability of an electron beam in the interaction with a high-frequency surface plasma wave. We denote by $\omega_\uparrow$ and $k_{z\uparrow}$ the solution to the set of equations

$$\omega = \sqrt{\Omega_h^2 - \Omega_{p\uparrow}^2}, \quad \omega = k_z u(1 - \sqrt{\alpha_b}). \quad (6.22)$$

It is obvious that, in the plane (ω, k_z), the values of $\omega_\uparrow$ and $k_{z\uparrow}$ are the coordinates of the point of the resonant interaction between a slow beam wave and a high-fre-

quency surface wave. At $k_z = k_{z\uparrow}$, the solution to dispersion relation (6.12) can be represented in a form analogous to solution (6.19):

$$\omega = \omega_\uparrow + \delta\omega_\uparrow, \quad |\delta\omega_\uparrow| \ll 1. \qquad (6.23)$$

Substituting solution (6.23) into dispersion relation (6.12), we obtain the following equation for the instability growth rate $\delta\omega_\uparrow$ in the interaction with the high-frequency wave:

$$\delta\omega_\uparrow^2(-2k_z u\sqrt{\alpha_b} + \delta\omega_\uparrow)$$

$$= \frac{1}{2}\Theta_\uparrow\alpha_b\Omega_{p\uparrow}k_z^2 u^2\frac{\Omega_{p\uparrow}}{\omega}\left(1 + \frac{\Omega_{p\uparrow}}{\omega}\frac{\partial\Omega_{p\uparrow}}{\partial\omega}\right)^{-1}. \qquad (6.24)$$

The right-hand side of this equation should be calculated at the resonant point $(\omega_\uparrow, k_{z\uparrow})$. From Eq. (6.24), we find the growth rates of the Cherenkov instability of an electron beam in the interaction with a high-frequency surface plasma wave:

$$\delta\omega_\uparrow$$

$$= \begin{cases} \dfrac{-1 + i\sqrt{3}}{2}\omega_\uparrow\left[\dfrac{1}{2}\Theta_\uparrow\alpha_b\left(\dfrac{\Omega_{p\uparrow}}{\omega_\uparrow}\right)^2\left(1 + \dfrac{\Omega_{p\uparrow}}{\omega_\uparrow}\dfrac{\partial\Omega_{p\downarrow}}{\partial\omega}\right)^{-1}\right]^{1/3}, \\[2mm] \sqrt{\alpha_b} \ll \Theta_\uparrow\left(\dfrac{\Omega_{p\uparrow}}{\omega_\uparrow}\right)^2 \\[2mm] i\dfrac{1}{2}\omega_\uparrow\left[\dfrac{1}{2}\Theta_\uparrow\sqrt{\alpha_b}\left(\dfrac{\Omega_{p\uparrow}}{\omega_\uparrow}\right)^2\left(1 + \dfrac{\Omega_{p\uparrow}}{\omega_\uparrow}\dfrac{\partial\Omega_{p\uparrow}}{\partial\omega}\right)^{-1}\right]^{1/2}, \\[2mm] \Theta_\uparrow\left(\dfrac{\Omega_{p\uparrow}}{\omega_\uparrow}\right)^2 \ll \sqrt{\alpha_b}. \end{cases} \qquad (6.25)$$

The instability with the first of growth rates (6.25) is called a single-particle Cherenkov effect, and the instability with the second of the growth rates is called a collective Cherenkov effect. For the waveguide parameters of Figs. 16 and 17, the coupling coefficient $\Theta_\uparrow$ is smaller than 0.13 because of the high value of the resonance frequency $\omega_\uparrow$. Also, the inequalities that determine the type of Cherenkov effect in dispersion relations (6.25) contain the coefficient $\Theta_\uparrow$ with the small factor $(\Omega_{p\uparrow}/\omega_\uparrow)^2$. Consequently, in discussing the examples illustrated in Figs. 16 and 17, we dealt with the collective Cherenkov regime of the beam instability in the interaction with a high-frequency surface plasma wave.

CONCLUSION

In conclusion, note that the physical meaning of the surface waves under consideration here and the mathematical structure of the formulas describing them are both governed by the character of plasma polarization. In the case of a low-frequency wave, the plasma is polarized predominantly in the longitudinal direction and the perturbations of the electric charge are impor-

tant over the entire volume of the annular plasma, so that the plasma behaves as if it were a conventional layer of thickness Δ. In terms of an analogy with mathematical potential theory [17], in describing a low-frequency surface wave, the role of the potential of the conventional layer is played by the electric field component E_z. It is well known that the potential of the conventional layer is continuous and its normal derivative in the layer is discontinuous; both of these circumstances are reflected in boundary conditions (2.13). In the case of a high-frequency surface wave, the plasma is polarized predominantly in the transverse direction and the perturbations of the electric charges of opposite sign are mostly localized near the surfaces of the annular plasma, so that the plasma behaves as if it were a double layer of thickness Δ. In describing a high-frequency surface wave, the role of the potential of the double layer is played by the electric field component E_z. This potential is known to be discontinuous within the layer, as reflected by the second of boundary conditions (3.12). The first of these conditions implies that, if the total electric charge of the double layer is equal to zero, then the electric field component normal to the layer (i.e., the directional derivative of the potential along the normal to the layer) is continuous. It is precisely specific polarization motions of the annular plasma in the surface waves under consideration that made possible the development of the method of the effective boundary conditions. Note that the above-described high-frequency surface wave is associated exclusively with the plasma layer: in a nonannular plasma ($r_1 = r_p - \Delta_p/2 = 0$), this wave does not exist.

The method of the effective boundary conditions makes it possible to analytically describe the main surface waves of a thin-walled annular plasma in a waveguide and the Cherenkov excitation of these waves by a thin-walled annular electron beam in an arbitrary external magnetic field. The method provides a wider range of applicability of the theoretical results obtained in plasma relativistic microwave electronics and outlines future directions for theoretical investigations in this field of plasma physics.

REFERENCES

1. Ya. B. Faĭnberg and M. F. Gorbatenko, Zh. Tekh. Fiz. **29**, 549 (1959) [Sov. Phys. Tech. Phys. **4**, 487 (1959)].

2. B. A. Aronov, L. S. Bogdankevich, and A. A. Rukhadze, Zh. Tekh. Fiz. **43**, 2493 (1973) [Sov. Phys. Tech. Phys. **18**, 1569 (1973)].

3. A. N. Kondratenko, *Plasma Waveguides* (Atomizdat, Moscow, 1976).

4. M. V. Kuzelev, E. V. Liperovkaya, and A. A. Rukhadze, Fiz. Plazmy **4**, 433 (1978) [Sov. J. Plasma Phys. **4**, 242 (1978)].

5. M. V. Kuzelev, R. V. Romanov, I. A. Selivanov, *et al.*, in *Eigenmodes of a Coaxial Plasma Waveguide in a Finite Magnetic Field* (Nauka, Moscow, 1994), Tr. Inst. Obshch. Fiz. Ross. Akad. Nauk **45**, 3 (1994).

6. M. V. Kuzelev, O. T. Loza, A. A. Rukhadze, *et al.*, Fiz. Plazmy **27**, 710 (2001) [Plasma Phys. Rep. **27**, 669 (2001)].

7. *Encyclopedia of Low-Temperature Plasma*, Vol. IV: *Plasma Electronics*, Ed. by V. E. Fortov (Nauka, Moscow, 2000), p. 87.

8. *Plasma and Electronic Microwave Amplifiers and Oscillators*, Ed. by Z. S. Chernov (Sov. Radio, Moscow, 1965).

9. A. F. Alexandrov, L. S. Bogdankevich, and A. A. Rukhadze, *Principles of Plasma Electrodynamics* (Vysshaya Shkola, Moscow, 1988; Springer-Verlag, Berlin, 1984).

10. M. V. Kuzelev and A. A. Rukhadze, *Electrodynamics of Dense Electron Beams in a Plasma* (Nauka, Moscow, 1990).

11. M. V. Kuzelev, F. Kh. Mukhametzyanov, and A. G. Shkvarunets, Fiz. Plazmy **9**, 1137 (1983) [Sov. J. Plasma Phys. **9**, 655 (1983)].

12. N. A. Krall and A. W. Trivelpiece, *Principles of Plasma Physics* (Academic, New York, 1973; Mir, Moscow, 1975).

13. *Plasma Electrodynamics*, Ed. by A. I. Akhiezer (Nauka, Moscow, 1974; Pergamon, Oxford, 1975).

14. M. Birau, M. A. Krasil'nikov, M. V. Kuzelev, and A. A. Rukhadze, Usp. Fiz. Nauk **167**, 1025 (1997) [Phys. Usp. **40**, 975 (1997)].

15. A. G. Shkvarunets, A. A. Rukhadze, and P. S. Strelkov, Fiz. Plazmy **20**, 682 (1994) [Plasma Phys. Rep. **20**, 613 (1994)].

16. M. V. Kuzelev, O. T. Loza, A. V. Ponomarev, *et al.*, Zh. Éksp. Teor. Fiz. **108**, 2048 (1996) [JETP **82**, 1102 (1996)].

17. A. N. Tikhonov and A. A. Samarskii, *Equations of Mathematical Physics* (Nauka, Moscow, 1972, 4th ed.; Pergamon, Oxford, 1964).

Translated by I. A. Kalabalyk

DUSTY
PLASMA

Dust Grain Charges in a Nuclear-Track Plasma and the Formation of Dynamic Vortex Dust Structures

V. A. Rykov*, A. V. Khudyakov*, V. S. Filinov**, V. I. Vladimirov**, L. V. Deputatova**,
D. V. Krutov**, A. P. Nefedov**[†], and V. E. Fortov**

* Leĭpunskiĭ Research Institute for Physics and Power Engineering, Russian State Scientific Center,
Obninsk, Kaluga oblast, 249020 Russia
e-mail: rykov@ippe.obninsk.ru
** Institute for High Energy Densities, Russian Academy of Sciences, Moscow, 127412 Russia
e-mail: dlv@ihed.ras.ru
Received December 3, 2001

Abstract—Results are presented from Monte Carlo calculations of the electric charge of dust grains in a plasma produced during the slowing down of the radioactive decay products of californium nuclei in neon. The dust grain charging is explained for the first time as being due to the drift of electrons and ions in an external electric field. It is shown that the charges of the grains depend on their coordinates and strongly fluctuate with time. The time-averaged grain charges agree with the experimental data obtained on ordered liquidlike dust structures in a nuclear-track plasma. The time-averaged dust grain charges are used to carry out computer modeling of the formation of dynamic vortex structures observed in experiments. Evidence is obtained of the fact that the electrostatic forces experienced by the dust grains are potential in character. © 2002 MAIK "Nauka/Interperiodica".

1. INTRODUCTION

Dust particles are widely encountered in nature. They are present in industrial and engineering processes, the environment, and cosmic space. The dust may often be technologically and environmentally harmful, so that removing it from the chambers of engineering devices and from the environment is an important practical task. Especially disastrous is the effect on humans, animals, and the environment of radioactive dust particles that can be released into the atmosphere during nuclear emergencies. Dust particles in the atmosphere, as well as in the chambers of technological devices, often form dust clouds. From a practical standpoint, it is important to investigate the physical properties of such clouds in order to learn to control their behavior and to overcome their possible dangerous effects. This challenging problem has been partially solved with developing and implementing electrical collecting filters in the ventilating systems of nuclear reactors. The mechanism by which such filters collect radioactive aerosol particles is based on the acquisition of electric charge by the dust in the plasma of corona discharges.

The behavior of dust particles in a plasma is the subject of a newly developed branch of plasma physics. The addition of even a small amount of dust to the plasma may considerably change the plasma properties. The discovery of the self-organization of dust

grains into liquidlike and crystalline ordered structures has attracted special attention. By now, static dust structures having long- and short-range orders were observed in the plasmas of stratified gas discharges [1, 2], thermal plasmas [3], and RF discharge plasmas [4]. The results of experiments on the formation of dust structures in air affected by a radioactive source were reported in [5]. It is well known that ordered dust structures can form when $\Gamma > 10$, where Γ is the coupling parameter, which characterizes the degree to which the plasma is nonideal and is defined as the ratio of the energy of the electrostatic interaction between dust grains to the energy of thermal motion. In the absence of screening, we have

$$\Gamma = \frac{Z^2 e^2}{aT};\qquad(1)$$

where Z is the dust grain charge in units of the electron charge e, a is the distance between the grains, and T is the energy of thermal motion. The parameter Γ is fairly large in a dusty plasma in which the distances between the grains are small and their charges are large.

The objective of this paper is to produce dynamic ordered dust structures in a nuclear-track plasma created by nuclear-reaction products in inert gases and to carry out computer modeling of the processes that lead to their formation.

We apply the Monte Carlo (MC) method to calculate the time dependence of the charge of dust grains in a nuclear-track plasma that decays under the action of an external electric field into the flows of electrons and

[†] Deceased.

ions drifting toward the oppositely charged electrodes. We show that, since the grain charge is alternately affected by electron and ion flows, it fluctuates strongly about a value smaller than that typical of a quasineutral plasma. The mean values of the grain charge agree with those measured experimentally.

We theoretically explain the formation of the experimentally observed dynamic vortex dust structures in a nuclear-track plasma in neon in the presence of an external electric field and experimentally test our theoretical model for describing such a plasma. Numerical investigations carried out using the method of molecular dynamics make it possible to explain the characteristic features of the formation of vortex dust structures. The numerical results presented here agree qualitatively with the experimental data. Evidence is obtained of the potential character of the electrostatic forces experienced by the dust grains.

2. CALCULATION OF THE DUST GRAIN CHARGE

Investigations of the behavior of dust grains in a plasma created by nuclear-reaction products provide new information on the self-organizing abilities of the dust in the plasma. The dusty plasma differs considerably in properties from other plasmas, the primary difference being that it is strongly inhomogeneous in space and highly unsteady in time. In a nuclear-track plasma, a dust grain is affected by the flows of drifting electrons and ions that are cylindrically symmetric in structure (the symmetry axis being parallel to the propagation direction of an ionizing particle). Because of diffusion, the electron and ion flows spread out in the radial direction; simultaneously, because of a difference in the electron and ion diffusion coefficients, the radii of the electron and ion cylindrical flows increase to a far greater extent. As a rule, the dust grains acquire a negative electric charge, because the electrons are much more mobile than the ions. The ion flows efficiently discharge the grains. The external electric fields of both the dielectric walls of an experimental device and its electrodes can substantially redirect the drift flows of plasma particles.

The experimental device in which we observed the formation of levitated dust structures consists of an ionization chamber with horizontally oriented parallel electrodes. The chamber was filled with neon at a certain pressure. Dust grains were injected through a hole in the upper electrode into the interelectrode space, in
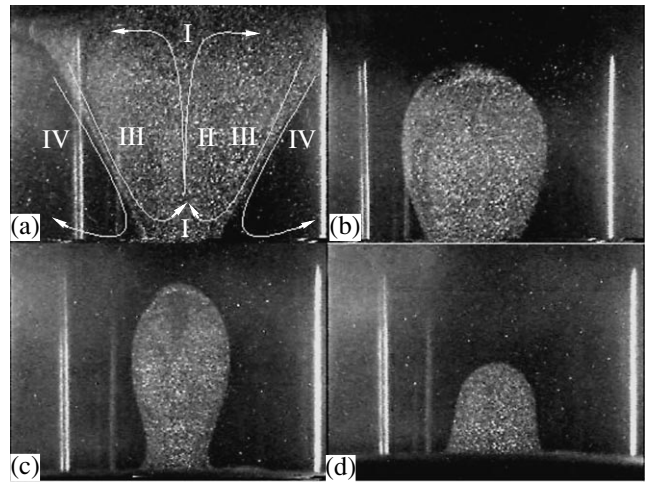

Fig. 1. Evolution of a cloud of Zn dust grains. The photographs were taken (a) 2 min, (b) 4 min, (c) 4 min 30 s, and (d) 4 min 45 s after the injection of the dust. The upper electrode was held at a potential of 152 V, the distance between the upper and lower electrodes was 3.5 cm, and the neon gas pressure was 76000 Pa. Each photograph corresponds to an observational area of 4.2×3.1 cm^2.

which the external electric field was created. The role of the radioactive source was played by a 7-mm-diameter plane layer of ^{252}Cf at the lower electrode. The numerical results presented below were obtained for the experiments condition under which we observed liquidlike dust structures (see table and Fig. 1).

The physical model of dust grain charging consists in the following. The ionizing particles emitted from the source are stopped in the gas over a time of several nanoseconds. The energy of the primary electrons is, on the average, 90 eV [6]. In turn, the primary electrons ionize neon atoms and thus produce a plasma cloud, which is called the track of an ionizing particle. The degree of plasma ionization inside the track is about 10^{-8}. The length of the track is much larger than the diameter of its cross section. As time elapses, the diameter of the track increases and, correspondingly, the electron and ion densities within the track decrease. The electric field generated in the track hinders charge separation [7] and delays this process in the presence of an external electric field. However, since the electron density gradient is large, the electron diffusion eventually reduces the electric field inside the track, so that the charges begin to be separated by the external field.

Conditions of our experiments on the formation of dynamic dust structures

Grain diameter, μm	Interelectrode distance, mm	Chamber radius, mm	Neon pressure, torr	High-voltage electrode potential, V	^{252}Cf source intensity, fission/s
1.87	17	15	380	162	10^5
2.1	35	25	557	152	4×10^6
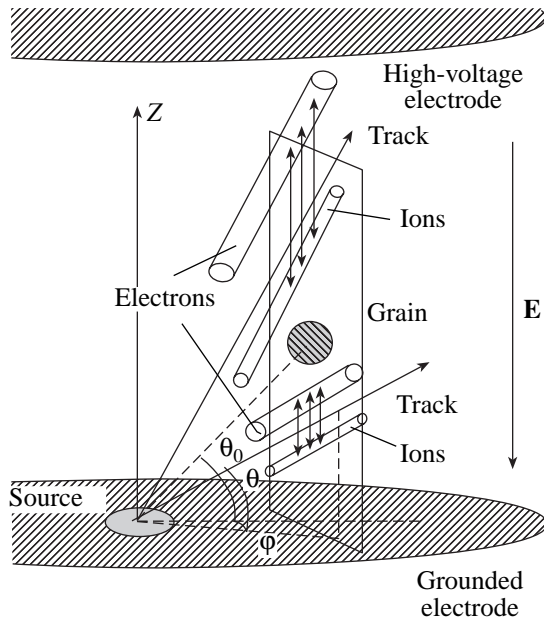
Fig. 2. Schematic of electron and ion motions in the vicinity of a dust grain in an electric field and geometry for MC simulations.

Hence, the process of the formation of a track plasma and the charging of dust grains proceeds in the following two stages. The first, extremely short (~100 ns [8]), stage of the track evolution is far from being studied completely. In the second, much longer (several microseconds), stage (electron drift in the interelectrode space), the dust grain charge changes after the track plasma decays into two flows, namely, the flows of electrons and ions drifting toward the oppositely charged electrodes and toward the charged dielectric walls of the device.

Let us discuss the main physical assumptions underlying the mathematical description of the dynamic processes in a nuclear-track plasma. We start by considering the second stage of the formation of dust structures and charging of the dust grains, because the processes occurring in this stage have been studied in great detail. Since the electric field strength in our experiments was such that the measured current reached the saturation stage, we neglect the recombination of charged particles. When a dust grain is affected by an electron flow from the track toward the positively charged electrode (anode), it collects some of the electrons and thus acquires a negative charge. When an ion flux meets this grain, it decreases the grain's negative charge and may even charge the grain positively (Fig. 2). A statistical treatment of these charging processes in time constitutes the essence of the mathematical model for calculating the grain charge. The main constants for these processes were chosen from the published data so as to satisfy the conditions of our particular experiments on the formation of ordered dust structures in neon.

Under the action of the electric field, the mean energy of the electron thermal motion becomes several orders of magnitude higher than the kinetic energy of the ions and neutral atoms. The mean electron energy was calculated from the formula [9]

$$\varepsilon = 9.7\frac{E}{p} \quad \text{for} \quad E/p = 0.1–1.2 \text{ V/(cm torr)}, \quad (2)$$

where E is the electric field strength and p is the gas pressure. In our experiments, the ratio E/p was equal to 0.25 V/(cm torr). The electron drift velocity w_e corresponding to this value was taken from [10, 11]. The electron mobility μ_e was calculated from the relationship

$$w_e = \mu_e E. \quad (3)$$

The electron diffusion coefficient D_e was calculated from the Nernst–Townsend–Einstein formula, which is valid for both electrons and ions. That is why we write this formula as the general relationship

$$\frac{\mu}{D} = \frac{e}{kT}, \quad (4)$$

where e is the electron charge, k is Boltzmann's constant, and T is the temperature. The electron mean free path was determined from the data on the cross section for the elastic scattering of electrons by neon atoms at the known density of a neon gas [10].

The temperature (mean energy) of the ions was set equal to that of the neon atoms. This assumption is justified in view of the effective energy exchange between ions and atoms. The ion diffusion coefficient was taken from [12]. The ion mobility was calculated from formula (4), and the ion drift velocity was calculated from a formula analogous to relationship (3). The ion mean free path was determined from the data presented in [11].

In order to simplify the analysis, the energy losses of the ionizing particles were calculated from the following analytic formulas:

$$E(x) = E_0\left(1 - \frac{x}{R}\right)^\alpha \quad \text{for fission fragments}, \quad (5)$$

$$E(x) = E_0\left(1 - \frac{x}{2R} - \frac{x^2}{2R^2}\right)^\alpha \quad \text{for alpha particles}, \quad (6)$$

where E_0 and E_1 are the initial energies of the ionizing particles, x is the distance between from the radioactive source, R is the total path length traversed by an ionizing particle before it is stopped in a neon gas, and α is the approximating parameter lying between 1 and 2. Formulas (5) and (6) were obtained by approximating the expressions that describe the energy losses of heavy ions in matter and follow from the Bethe and Lindhardt theories.

The energy losses were normalized to the energy cost of the production of one electron–ion pair (for

neon, this cost is 35 eV) [13]. As usual, we assumed that the energy cost does not change as the energy of the ionizing particles decreases. In a nuclear-track plasma, the dynamics of the electric charge q of a dust grain in electron and ion flows is described by the equation

$$\frac{dq}{dt} = I, \tag{7}$$

where I is the total electron and ion current to the grain surface. The mathematical expression for this current is governed to a large extent by the ratio of the grain diameter to the mean free paths of the plasma particles. Thus, a grain diameter of 1 μm is four times smaller than the electron mean free path, but six times larger than the ion mean free path. That is why we used two different approaches to calculating the electron and ion currents to the grain surface. The electron current, which is determined by the absorption cross section for plasma electrons, was calculated from the formula [14, 15]

$$I = 2\sqrt{2\pi}\, n_e v_T a^2 \exp\left(-\frac{e\varphi}{T_e}\right), \tag{8}$$

where a is the grain radius, n_e is the electron density, v_T is the electron thermal velocity, and φ is the potential acquired by the grain during the charging process.

The charge acquired by a negatively charged grain in ion flows is determined by the currents of positive and negative ions to its surface. These currents are described by the following analytic formulas, which were obtained in the diffusion approximation:

$$I_- = \frac{4\pi D_- N_- q e^2}{T[\exp(q e^2/r_0 T_-) - 1]},$$

$$I_+ = \frac{4\pi D_+ N_+ q e^2}{T[1 - \exp(-q e^2/r_0 T_+)]}. \tag{9}$$

The charge of the grain affected simultaneously by the electron and ion flows is determined by the total current of the electrons and ions. If the electron mean free path is much larger than the grain diameter, the electron current is calculated from formula (8); otherwise, it is calculated from the first of formulas (9). For electron mean free paths comparable with the grain diameter, the electron current is calculated by matching formula (8) with the first of formulas (9). The ion current to the grain surface is calculated from the second of formulas (9). As a result, the dynamics of the grain charge is described by the equation

$$\frac{dq}{dt} = I_- - I_+. \tag{10}$$

In a nuclear-track plasma with a low degree of ionization and a low electron temperature, the dust grains acquire small charges.

## 3. STATISTICAL MODELING OF THE TRACKS OF IONIZING PARTICLES

As was already noted, the plasma created by high-energy ionizing particles is strongly inhomogeneous in space and highly unsteady in time, and the degree of ionization is the highest near the radioactive source of the experimental device. At relatively low intensities of radioactive sources approved for use in laboratories, the tracks of different ionizing particles do not intersect and the plasma exists for a short time in the form of long narrow tracks, whose distribution in space and time exhibits statistical regularities. Hence, the first step in calculating the charge of dust grains in a nuclear-track plasma is to model the track distribution statistically by the MC technique.

Let a dust grain be located at some distance r from a point radioactive source, and let the angle that the straight line passing through the grain and source makes with the horizontal plane be θ_0 (Fig. 2). The angle θ is measured from the horizontal plane, and the azimuthal angle φ is measured from the vertical plane containing the grain and the source. A uniform electrostatic field is assumed to be created by two electrodes, the upper of which is held at a positive potential.

In order to economize on the computer time, among the ionizing particles emitted from the source in all possible azimuthal directions, we chose only those that generate such flows of drifting electrons for which the probability of meeting the grain is nonzero. It is electrons that, due to their large diffusivity, determine the region where the statistical track distribution should be modeled. We also took into account the fact that, for very small angles θ_0, this region can be determined by the downward drifting ions. For the emission events modeled by this statistical sampling, our code calculates the mean time between the events, which, in turn, are distributed in time according to the Poisson law [16]. Then, the code statistically samples the type of ionizing particle (an alpha particle or a fission fragment). It is assumed that the source emits 16 alpha particles per one fission fragment (the second fission fragment is lost in the substrate); in other words, it is assumed that one-half of each 32 alpha particles are lost in the substrate. In each statistical sample of the angle θ, the code determines what type of newly produced particles can meet the grain: electrons or ions. Then, the code calculates the drift time required for a newly produced electron (or ion) to reach the grain. If this time is too short for the flow of the drifting electrons (or ions) to meet the grain, then the code stops calculating this event. Otherwise, if the flow meets the grain, the code calculates the electron (ion) density in the flow, the instant when the flow reaches the grain surface, and the residence time of the grain within the flow. Because of the statistical nature of the processes in question, the grain charge may be recycled, i.e., the grain can be charged by the electrons (or ions) of the next but nearer track before it will be charged by the electrons (or ions)
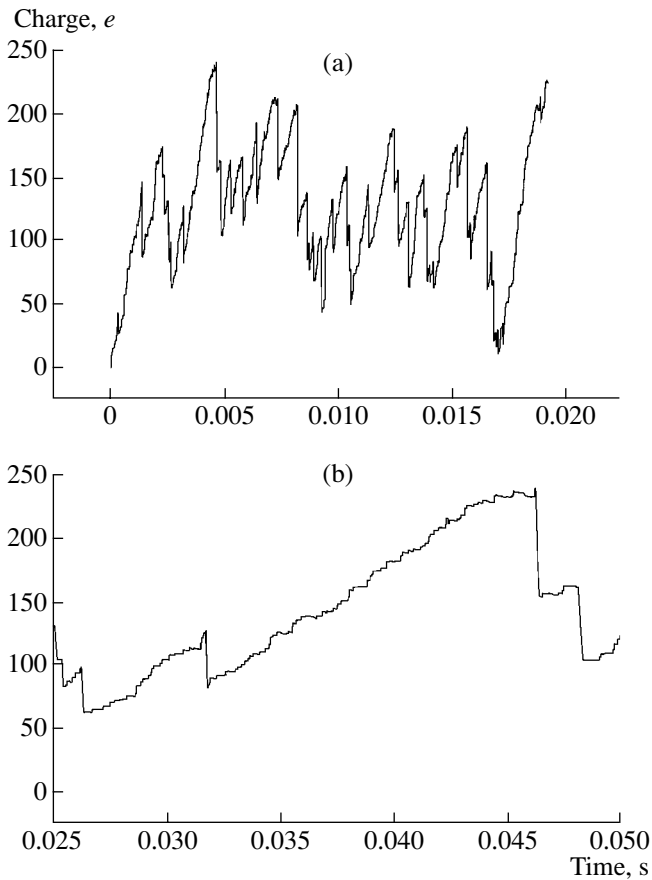
Charge, *e*

Charge, *e*

Fig. 3. (a) Time evolution of the dust grain charge in a neon gas ionized by alpha particles and fission fragments (the time-averaged grain charge is equal to 105 electron charges) and (b) magnified fragment of the image. Here and below, the grain charge is expressed in units of the absolute value of the electron charge *e*.
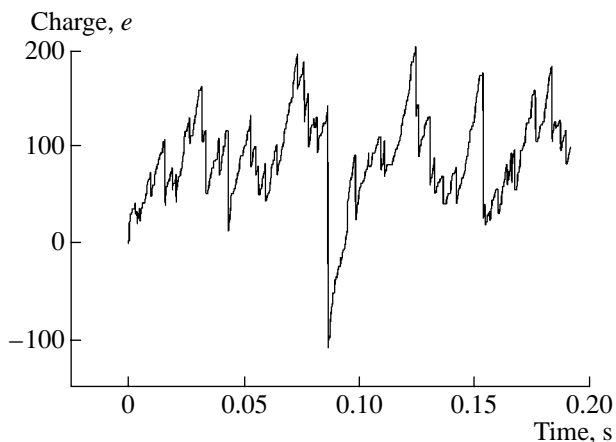
Fig. 4. Calculated time evolution of the dust grain charge in a neon gas ionized only by 90-MeV fission fragments. The time 0.075 s corresponds to the direct impact of a fission fragment on a dust grain (as a result, the grain loses 250 electrons).

of the preceding but farther track. That is why the times at which each of the flows meets the grain and departs from it, as well as the density of the drifting plasma particles, are stored in computer memory. Then, the code regulates (sorts) all of these processes in time. If the flows from different tracks overlap, the code sums the corresponding particle densities in the overlap regions. Then, the code integrates Eq. (10) by the Runge–Kutta method. In this equation, the currents are calculated as functions of the grain radius: the electron current is calculated from formula (8) or by matching formula (8) with the first of formulas (9), and the ion current is calculated from the second of formulas (9). In our simulations, the longitudinal and transverse diffusion coefficients for the electrons were different but, for the ions, these coefficients were assumed to be the same, which is valid for the ratios E/N (where N is the density of neon atoms) typical of our experiments ($\sim 10^{-17}$ V cm^2) [9]. At this point, we should emphasize the following characteristic difference between the charging process in a nuclear-track plasma and in a quasineutral plasma: in the case at hand, the currents on the left-hand side of Eq. (10) are strongly fluctuating, which leads to strong fluctuations of the dust grain charge with time.

The numerical results obtained for a grain located at a distance of 1 cm from the source and for $\theta_0 = 45°$ are illustrated in Figs. 3–5. Since the grain charge is negative, the ordinate shows the absolute value of the charge, for convenience in representing the results. First of all, note that the grain charge fluctuates strongly with time. On the one hand, the grain acquires a charge in electron attachment processes; on the other hand, its charge decreases substantially in less frequent events of interaction with the ions. This stems from the fact that the grain interactions with the electrons and ions are different in nature: a negatively charged grain repulses electrons but attracts positively charged ions. Since the ionizing ability of alpha particles is far lower than that of fission fragments, they have an insignificant impact on the process under consideration and are responsible exclusively for small-amplitude variations in the time evolutions of the grain charge (Fig. 3b).

As an example, Fig. 4 illustrates the results obtained for the direct impact of a fission fragment on a dust grain. As a result of secondary electron emission, the grain loses 250 electrons simultaneously [6]; however, the lost charge is soon restored.

The dependence of the mean charge of the grain on its radius is almost linear (Fig. 5), as is the case for a quasineutral plasma. The experimental points in Fig. 5 were obtained for levitated spherical monodisperse melamineformaldehyde grains, whose charge was determined from the balance between the gravity and electrostatic forces with allowance for the nonuniformity of the electric field under the hole in the upper electrode.
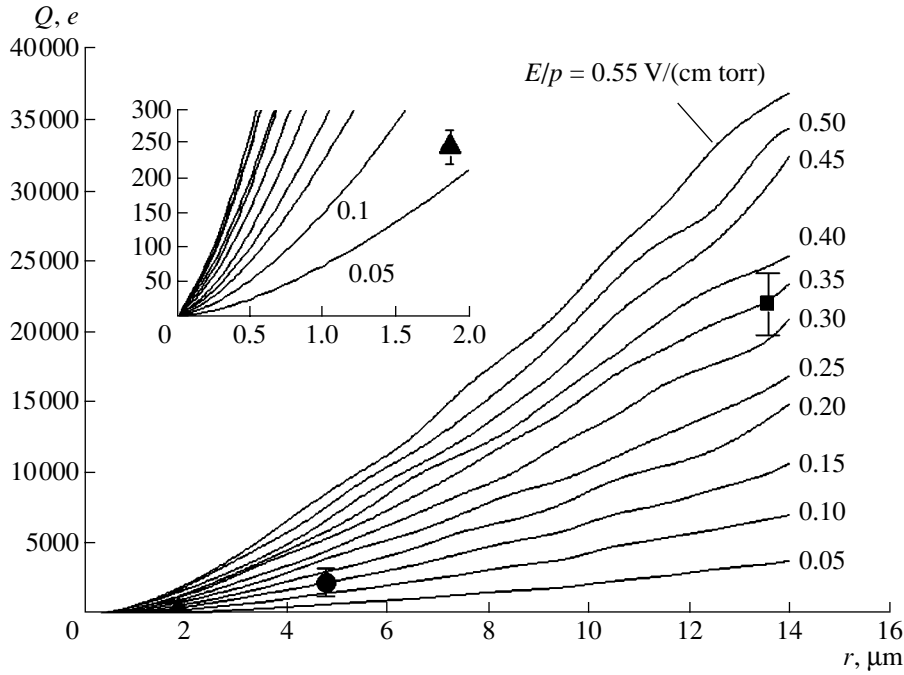
Fig. 5. Calculated dependence of the grain charge on the ratio E/p and the grain diameter in Ne at a pressure of 380 torr. The grain is at a distance of 3 cm from the radioactive source, the angle that the straight line passing through the grain and source makes with the horizontal plane of the source being 75°. The distance between the electrodes is 3.5 cm. The symbols stand for the experimental results: the closed square corresponds to $E/p = 0.3$ V/(cm torr) and $r_d = 13.57$ µm, the closed circle refers to $E/p = 0.155$ V/(cm torr) and $r_d = 4.82$ µm, and the closed triangle is for $E/p = 0.09$ V/(cm torr) and $r_d = 13.57$ µm. The inset shows a magnified fragment of the figure for grains with small diameters and low charges.

4. DUST GRAIN CHARGING IN NUCLEAR TRACKS

The description of plasma processes in the above slow stage, in which the drift flows of plasma electrons and ions form and charge the dust grains, is valid at sufficiently large distances from the radioactive source, i.e., in regions where the tracks occur close to the dust grain only in sufficiently rare cases. Near the source, i.e., in the region where the frequency of occurrence of the tracks close to the grain increases in proportion to $1/r^2$, the dust grain charge is determined primarily by the asymptotic behavior of the nonequilibrium electron distribution function in the high-energy range. In this region, the grain charging process is dominated by the electrons produced by ionization in the track and also by the frequency of occurrence of the tracks close to the grain and the discharging of the grain in the flows of drifting ions. Recall that the evolution of the tracks is extremely fast (~100 ns [8]) and is far from being studied completely. However, assuming that this evolution is described by the approximate expressions (5) and (6) and applying the model of grain charging that was proposed in [17, 18] yields the following estimate for the mean charge of a dust grain:

$$\langle Q(\mathbf{r}) \rangle = C\phi_t(\mathbf{r}). \qquad (11)$$

Here, the coefficient $C \simeq 4\pi\varepsilon_0 R_p$ is approximately equal to the capacitance of the grain and the coordinate-dependent function $\phi_t(\mathbf{r})$ has the form

$$\phi_t(\mathbf{r}) \approx \frac{R_p \gamma \varepsilon \Phi_s}{2\pi NeC} \left\{ 2\frac{dE_0(\zeta_0)}{\zeta_0^2 d\zeta_0} + 32\frac{dE_1(\zeta_1)}{\zeta_1^2 d\zeta_1} \right\}, \qquad (12)$$

where $N = (2E_0 + 32E_1)$, ε is the energy cost of the production of an electron–ion pair, $\zeta_i = |\mathbf{r}/R_i|$, r is the distance from the ionization source, R_p is the grain radius, R_0 is the total path length traversed by a fission fragment before it is stopped, R_1 means the same for the alpha particles, E_0 is the initial energy of a fission fragment, and E_1 means the same for the alpha particles. Hence, the mean charge $\langle Q \rangle$ of the grain is a prescribed function of its spatial coordinates.

Clearly, in experiments with dust grains of different diameters, the values of the ratio E/p are different. On the average, the condition for spherical grains of radius r_0 to be in equilibrium yields the relationship

$$\langle Q \rangle E = mg = \frac{4}{3}\pi\rho r_0^3, \qquad (13)$$

where m is the mass of a grain and ρ is the density of the matter. For the mean strength of the electrostatic field, the characteristic mean grain charges calculated

z, cm

(a)

(b)

x, cm
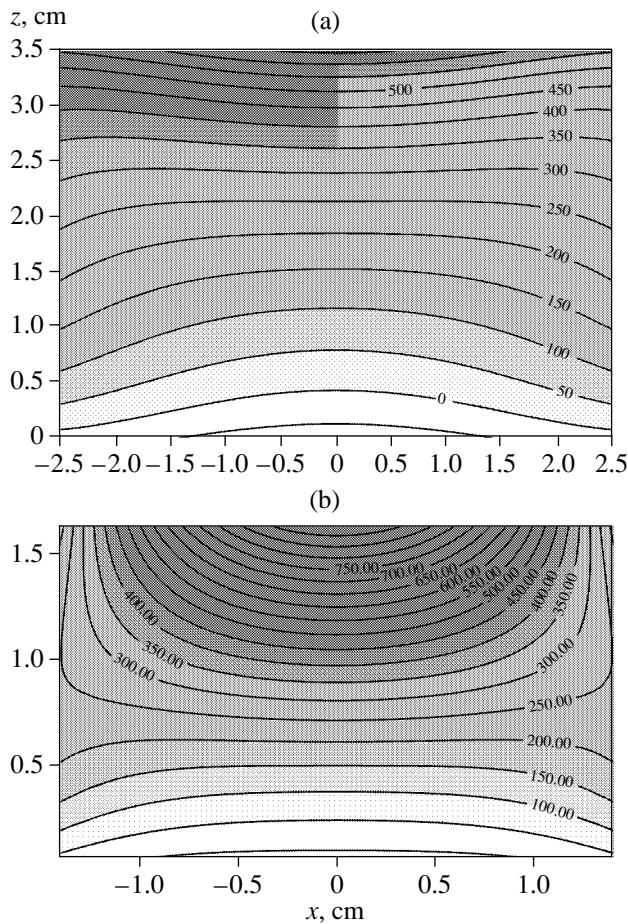
Fig. 6. Dependence of the dust grain charge (in units of *e*) on the spatial coordinates under the conditions given in the table for a grain diameter of (a) 2.1 and (b) 1.87 μm. The *x*-axis lies in the plane of the source, which is located at the point (0, 0).

in units of the electron charge from this relationship range from 100 to 1000.

In numerical modeling of the dynamic vortex structures, the dependence of the dust grain charge on the spatial coordinates was obtained by matching the dependences obtained for small and large distances (Fig. 6) between the grain and the radioactive source. As a result, we can see that the grain charge increases sharply as the source is approached.

5. COMPUTER MODELING OF THE DYNAMICS OF THE FORMATION OF LIQUIDLIKE DUST STRUCTURES

Since this is the first paper in which an attempt is made to model the formation of vortex structures from dust grains in a nuclear-track plasma, our theoretical approach does not pretend to completely describe the dust behavior under the experimental conditions in question. Our main objective here is to develop a reasonable model for describing the most characteristic

features of the grain behavior in a plasma and to reveal the main physical mechanisms for the formation of a potential trap that ensures the levitation of the dust grains. That is why it is expedient to carry out numerical modeling for the experimental conditions under which vortex structures were stable. In this context, it is most reasonable to model the structures like that shown in Fig. 1, which were observed to form in a nuclear-track neon plasma at pressures from 2.5×10^4 to 7.5×10^4 Pa.

In order to investigate the levitation of dust grains and their mutual interactions, it is necessary not only to establish the mechanism for their charging but also to reveal the nature of the forces acting upon them. At present, several different mechanisms are being discussed in the literature that affect both the balance between the gravity and electrostatic forces experienced by the levitated dust grains and the interactions between them (see [6, 17, 18] for details). Here, we investigate the complex dynamic problem under consideration by a simplified approach that makes it possible to trace the formation of dynamic vortex structures and their evolution using a reasonable amount of computer time. First, because of the comparatively small charges of dust grains and comparatively large mean distances between them, we neglect their mutual interactions. Second, because of the low intensity of the radioactive source and low degree of ionization of the nuclear-track plasma created by it, we ignore the drag forces exerted on dust grains by drift ion flows, which are directed primarily downward, i.e., toward the grounded electrode (with the radioactive source) and the dielectric wall of the device. In future studies, we are going to consider how the drag forces influence the formation of dynamic vortex structures. In the model developed here, we take into account the interaction of grains with the electrostatic fields of both the electrodes of the device and its walls, the weight of the grains, and the effect of their friction with the buffer gas. The levitation of dust grains results from the balance between the gravity force associated with the mass of the grain and the electrostatic forces of the device, in which case the electrostatic fields are governed equally by the internal plasma processes and by the processes of recombination and adsorption of the charges on the walls. In our experiments, the electrostatic trap was created by the electrostatic fields of both a negative surface charge on the walls of the device and a positive charge of the electrode with a hole. The effect of the steady-state positive space charge induced in the plasma near the radioactive source is insignificant because the electron mobility is much higher than the ion mobility. This effect will be taken into account in ongoing studies. Numerical modeling of the vortex structures of charged dust grains in the electrostatic trap of the device requires the use of convenient analytic expressions for the electrostatic potential that should correctly reflect its physical nature. The numerical results presented in

this paper were obtained from the expressions derived in [17].

Dynamic vortex dust structures in a nuclear-track plasma were simulated using the standard method of molecular dynamics. This method usually assumes calculations for a finite number N of particles in a cell of size L. In order for the computations to take a reasonable amount of time on available computers, we restricted our simulations to $N = 200$–1000. Accordingly, in order for an MC cell to capture the characteristic dust structure, the linear cell size was chosen to be equal to $L = 100r_D \approx 3$ cm, which approximately corresponds to our experimental conditions. Note that such a small cell size, as well as a smaller number of dust grains in comparison with that in the experiments, substantially relaxed the requirements on computational resources and made it possible to reduce the run time of the code to about ten hours. We modeled levitated dust grains in an electrostatic trap with the potential derived in [17]. The characteristic potential at the chamber wall was varied in the range from 0.5 to 3 V. The z-axis was directed downward, i.e., along the direction of the gravity force. The initial spatial distribution of dust grains and their initial velocities were specified with the help of computer-generated random numbers, distributed uniformly within the interval from zero to unity.

6. DISCUSSION OF THE CALCULATED RESULTS

Here, we present the results of numerical simulations carried out by the standard method of molecular dynamics for a cylindrical volume in space. Figure 7 shows parts of the grain trajectories inside a planar vertical axial layer of small radial thickness. The trajectories were calculated at three successive times. The arrows indicate the direction of the grain motion. The physical cause of the onset of dynamic vortex structures is the dependence of the charges of both dust grains and the device walls on the distance from the source. In fact, let us consider a grain located near the upper electrode, in which case the grain's negative charge is small because its distance from the source is large. Under the action of the gravity force, which exceeds the electrostatic force of attraction toward the upper electrode, the grain starts falling downward, i.e., toward the lower electrode. In such motion, the grain charge, first, decreases and, then, begins to increase. A downward moving grain experiences increasingly strong radial fields of the dielectric walls, whose charge, in turn, increases near the radioactive source. The radial forces bend the grain trajectory and cause the grain to move toward the device axis and toward the radioactive source at the axis. On the other hand, as the charge of the grain increases, it is affected by the increasingly strong upward-directed electrostatic force of the positively charged upper electrode. Because of inertia, the grain passes the equilibrium position and its charge continues to increase until the electrostatic force
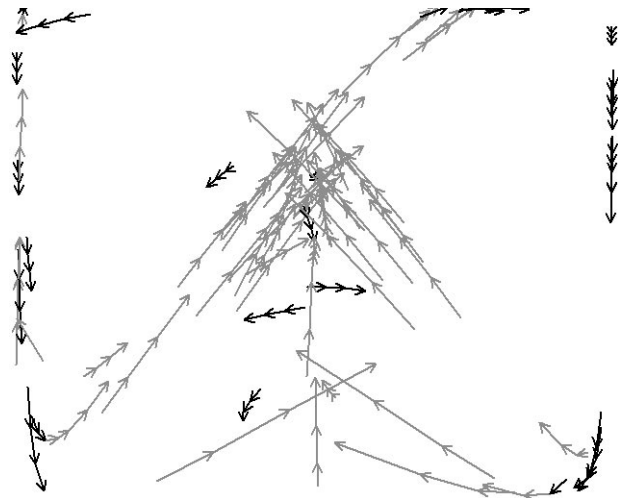
Fig. 7. Schematic representation of a thin layer of the vortex dynamic structure obtained using the method of molecular dynamics under the assumption that the forces acting upon the grains are potential. Each part of the grain trajectories calculated at three successive times is shown by three successive arrows. The black and gray arrows refer to the grains moving downward and upward, respectively. The radioactive source is at the center of the bottom of the frame.

becomes larger than the gravity force. The grain begins to move upward, keeping its radial velocity component unchanged, until the gravity force becomes larger than the electrostatic force. Then, this cycle of the grain's motion repeats itself. As a consequence, most of the grain trajectories are very similar in shape to the infinity symbol. In the axial region of the device, the grains move predominantly upward, while, in the peripheral region near the walls, the grains fall downward. As a result, a dynamic vortex structure forms that consists of dust grains rotating in the same direction as the vortex structures observed in our experiments.

We stress the following important feature of the results obtained here. In our study, the main attention is focused on energy transfer from the radioactive source, which creates the plasma, to the disperse grains. The energy-transfer mechanism is associated with the variation in the charge of a moving dust grain. The charge of the grain is a function of its spatial coordinates and also depends on the energy parameters of the inhomogeneous plasma closely around it. Hence, the above system of levitated dust grains is an open system, which exchanges energy with its surrounding. Following [2, 18], we assume that the electrostatic forces acting upon the grains are potential in character. As a result, these forces (which are defined as minus the spatial gradient of the potential energy) are described by two types of terms. The terms of the first type are formally similar in structure to those describing the Coulomb forces of particles with coordinate-dependent charges. The terms of the second type (non-Coulomb correction) account for the dependence of the charges on the
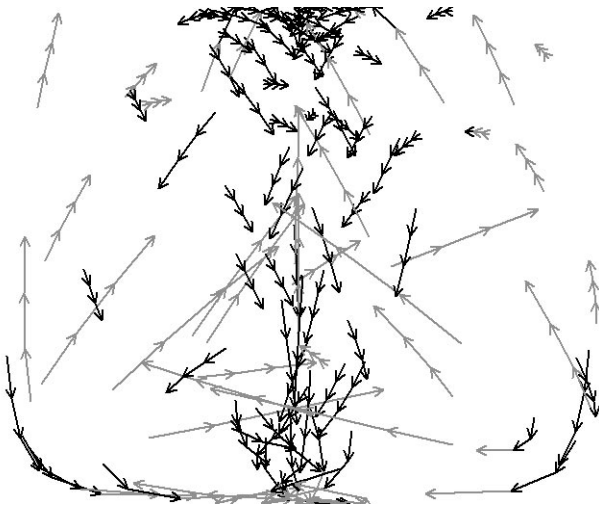
Fig. 8. Thin layer of a dynamic structure analogous to that in Fig. 7. The parts of the grain trajectories were calculated under the assumption that the forces acting upon the grains are nonpotential.

Fig. 9. Late stage of the time evolution of the dynamic structure shown in Fig. 7 under the long-term action of the frictional forces exerted by the buffer gas on the dust grains.

Fig. 10. Late stage of the time evolution of the dynamic structure shown in Fig. 8 under the long-term action of the frictional forces exerted by the buffer gas on the dust grains.

spatial coordinates and are represented in terms of the gradients of the grain charges and the gradient of the surface charge on the dielectric walls of the device. Note that the effect of the surface charge is equivalent

to that of an effective macroparticle. Non-Coulomb forces are directed opposite to the gradient of the absolute value of the grain charge and displace a dust cloud toward the region where the grain charges and, accordingly, the Coulomb repulsion energy in the device are both minimum.

In the alternative approach [19], the electrostatic forces acting upon the dust grains in a plasma are assumed to be Coulomb forces $|F| \sim q(r_1)q(r_2)/|r_1 - r_2|$ with coordinate-dependent grain charges. However, as was noted in [19], these forces cannot be represented in terms of the gradient of a certain effective potential. Consequently, the terms describing these forces do not contain the charge gradient, as is the case with the terms of the second type.

The results obtained from the alternative approach [19] for the same parameters and the same model device as in Fig. 7 are illustrated in Fig. 8, which again shows parts of the grain trajectories inside a thin planar vertical axial layer, calculated at three successive times. We can see the formation of a vortex structure in which the grains rotate in two opposite directions, which, however, contradicts our experimental observations. Hence, a comparison of the results of numerical modeling with experimental data clearly indicates the potential character of the forces acting upon the grains in a nuclear-track dusty plasma.

The effect of the frictional forces exerted by the buffer gas on the dust grains is illustrated in Figs. 9 and 10, which show parts of the grain trajectories inside a vertical axial layer of small radial thickness in the model device, calculated at three successive times. The frictional forces were calculated from Stokes' law. The computations were carried out using the above two approaches. We can see that, under the action of the frictional forces, the linear dimensions of the dynamic vortex structures of dust grains become several times smaller than in the initial stage and the structures themselves evolve to a nearly steady stable state analogous to that simulated by the MC method in [18]. The calculated time evolution of the vortex structures agrees qualitatively with the experimental observations illustrated in Fig. 1.

7. CONCLUSION

The main results of our investigations can be summarized as follows. The spatial dependence of the dust grain charges has been calculated. The experimentally observed formation of the dynamic vortex structures of dust grains under the action of an external electric field in a nuclear-track plasma in neon has been explained theoretically. The theoretical model of such a plasma has been tested experimentally. The physical mechanisms for levitating dust grains and forming dynamic vortex structures in a nuclear-track plasma in neon have been investigated both theoretically and experimentally.

The MC method has been applied to trace the time evolution of the dust grain charge in a nuclear-track plasma, which disintegrates under the action of an external electric field into the flows of electrons and ions drifting toward the electrodes.

The dynamic vortex dust structures that form under the action of an external electric field in a nuclear-track plasma in neon has been explained theoretically, and the theoretical model of such a plasma has been tested experimentally. Numerical simulations carried out using the method of molecular dynamics made it possible to explain the characteristic features of the formation of vortex dust structures. It has been shown that the non-Coulomb forces, which are described by the terms proportional to the gradients of the charges and, along with the Coulomb forces, act on the dust grains, reverse the rotation of vortex dust structures. The resulting direction of rotation agrees with our experimental observations, thereby qualitatively indicating the potential character of the electrostatic forces of interaction between the grains. We have also analyzed the effects of friction between the buffer gas and the dust grains on both the evolution of dynamic vortex dust structures and the formation of the steady-state structures that were investigated previously by the MC method [18]. The results of calculating these effects numerically agree qualitatively with our experimental data.

ACKNOWLEDGMENTS

REFERENCES

1. V. E. Fortov, A. P. Nefedov, V. M. Torchinskiĭ, *et al.*, Pis'ma Zh. Éksp. Teor. Fiz. **64**, 86 (1996) [JETP Lett. **64**, 92 (1996)].

2. O. M. Belotserkovskiĭ, I. E. Zakharov, A. P. Nefedov, *et al.*, Zh. Éksp. Teor. Fiz. **115**, 819 (1999) [JETP **88**, 449 (1999)].

3. V. E. Fortov, V. S. Filinov, A. P. Nefedov, *et al.*, Zh. Éksp. Teor. Fiz. **111**, 889 (1997) [JETP **84**, 489 (1997)].

4. Yu. V. Gerasimov, A. P. Nefedov, V. A. Sinel'shchikov, and V. E. Fortov, Pis'ma Zh. Tekh. Fiz. **24** (19), 62 (1998) [Tech. Phys. Lett. **24**, 774 (1998)].

5. V. E. Fortov, V. I. Vladimirov, L. V. Deputatova, *et al.*, Dokl. Akad. Nauk **366** (2), 22 (1999) [Dokl. Phys. **44**, 279 (1999)].

6. P. P. D'yachenko and V. A. Rykov, At. Énerg. **82**, 365 (1997).

7. A. P. Budnik and I. V. Dobrovol'skaya, Preprint No. 2498 (Institute of Physics and Power Engineering, Obninsk, 1996).

8. A. P. Budnik, Yu. V. Sokolov, and A. S. Vakulovskiy, Hyperfine Interact. **88**, 185 (1994).

9. Yu. P. Raizer, *Gas Discharge Physics* (Nauka, Moscow, 1987; Springer-Verlag, Berlin, 1991).

10. L. G. H. Huxley and R. W. Crompton, *The Diffusion and Drift of Electrons in Gases* (Wiley, New York, 1974; Mir, Moscow, 1976).

11. V. E. Golant, A. P. Zhilinskii, and I. E. Sakharov, *Fundamentals of Plasma Physics* (Atomizdat, Moscow, 1977; Wiley, New York, 1980).

12. E. W. McDaniel and E. A. Mason, *The Mobility and Diffusion of Ions in Gases* (Wiley, New York, 1973; Mir, Moscow, 1976).

13. B. B. Rossi and H. H. Staub, *Ionization Chambers and Counters: Experimental Techniques* (McGraw-Hill, New York, 1949; Inostrannaya Literatura, Moscow, 1950).

14. V. N. Tsytovich, Usp. Fiz. Nauk **167**, 57 (1997) [Phys. Usp. **40**, 53 (1997)]; A. P. Nefedov, O. F. Petrov, and V. E. Fortov, Usp. Fiz. Nauk **167**, 1215 (1997) [Phys. Usp. **40**, 1163 (1997)].

15. B. M. Smirnov, *Aerosols in Gas and Plasma* (Inst. Vys. Temp. Akad. Nauk SSSR, Moscow, 1990).

16. A. I. Abramov, Yu. A. Kazanskiĭ, and E. S. Matusevich, *Foundations of Experimental Methods in Nuclear Physics* (Atomizdat, Moscow, 1970).

17. V. I. Vladimirov, L. V. Deputatova, V. I. Molotkov, *et al.*, Fiz. Plazmy **27**, 37 (2001) [Plasma Phys. Rep. **27**, 36 (2001)].

18. A. V. Zobnin, A. P. Nefedov, V. A. Sinel'shchikov, *et al.*, Fiz. Plazmy **26**, 445 (2000) [Plasma Phys. Rep. **26**, 415 (2000)].

19. V. V. Zhakovskiĭ, V. I. Molotkov, A. P. Nefedov, *et al.*, Pis'ma Zh. Éksp. Teor. Fiz. **66**, 392 (1997) [JETP Lett. **66**, 419 (1997)].

Translated by G. V. Shepekina